

HETEROGENEOUS NUCLEATION AND INFLUENCE OF
SURFACE STRUCTURE AND WETTABILITY

By

YUSEN QI

A DISSERTATION PRESENTED TO THE GRADUATE SCHOOL
OF THE UNIVERSITY OF FLORIDA IN PARTIAL FULFILLMENT
OF THE REQUIREMENTS FOR THE DEGREE OF
DOCTOR OF PHILOSOPHY

UNIVERSITY OF FLORIDA

2005

Copyright 2005

by

Yusen Qi

To My Family, Lian Lu and Andrew Qi.

ACKNOWLEDGMENTS

I acknowledge Professor James F. Klausner, my Ph.D. advisor, who has freely given me his time and guidance during the course of this fundamental research. Providing critical thinking and penetrating discussions, Dr. Klausner contributed much to the understanding of this research. Not only does he value classical principles, but he also conceives new possibilities when experimental observations do not support classical theory. Professors Renwei Mei, David Worthington Hann, Wallace Gregory Sawyer and Samim Anghaie were extremely helpful in several aspects of this research while serving on my supervisory committee. My indebtedness to them cannot be overstated.

My fellow graduate students, Chris Velat, Jason Bower, Jun Liao, and Yi Li, have graciously given their time and experience. Undergraduate student Kris Dean contributed significantly to the final stage of experimental research.

Finally, I would like to thank my parents for the most needed encouragement to finish my studies.

Special thanks are given to my wife, Lian Lu, for years of support. Without her sacrifice, it would have been impossible for me to complete this work. The love she provides makes this work more satisfying.

TABLE OF CONTENTS

	<u>page</u>
ACKNOWLEDGMENTS.....	iv
LIST OF TABLES	viii
LIST OF FIGURES.....	ix
NOMENCLATURE.....	xiii
ABSTRACT	xvi
CHAPTER	
1 INTRODUCTION	1
1.1 Heterogeneous Nucleate Boiling	1
1.2 Current Understanding of Heterogeneous Nucleation.....	2
1.3 Outline of the Current Investigation	5
2 GAS NUCLEATION TECHNIQUE.....	8
2.1 Introduction and Literature Survey	8
2.1.1 Bubble Counting Method.....	8
2.1.2 Gas Nucleation Study	9
2.2 Gas Nucleation Facility Overview.....	10
2.3 Test Section Design	11
2.3.1 Low Pressure Test Section.....	12
2.3.2 High Pressure Test Section	13
2.4 Surface Preparation	15
2.5 Instrumentation and Calibration.....	15
2.6 Experimental Results	17
2.6.1 Static Contact Angle Measurements.....	17
2.6.2 Advancing and Receding Contact Angle Measurements	21
2.6.3 Nucleation Site Density Measurements Using Water.....	23
2.6.4 Nucleation Site Density Measurements Using Ethanol.....	26
3 POOL BOILING TECHNIQUE.....	27
3.1 Pool Boiling Facility Overview	27

3.2	Fabrication of Heater Assembly	28
3.3	Surface Preparation	30
3.4	Instrumentation and Calibration.....	31
3.5	Experimental Results	32
3.5.1	Temperature Measurements.....	32
3.5.2	Boiling Curve.....	33
3.5.3	Experimental Observation	38
3.5.4	Nucleation Site Density Comparison for Pool Boiling and Gas Nucleation	40
3.5.5	Discussion.....	46
4	STATISTICAL MODEL FOR HETEROGENEOUS NUCLEATION	51
4.1	History and Review.....	51
4.1.1	Gas Trapping Criteria.....	51
4.1.2	Bubble Inception.....	53
4.1.3	Surface Characterization.....	54
4.1.4	Statistical Model	55
4.2	Surface Characterization	56
4.2.1	Instrumentation	56
4.2.2	Identifying Gas Trapping Cavities.....	58
4.2.3	Distribution of Cavity Diameters.....	63
4.2.3.1	Introduction of Weibull distribution.....	63
4.2.3.2	Distribution of cavity diameters	64
4.2.4	Distribution of Cavity Half-cone Angles.....	66
4.3	Prediction of Nucleation Site Density.....	69
4.3.1	Prediction with Gas Nucleation Results	69
4.3.2	Prediction with Pool Boiling Results.....	73
4.3.3	Discussion.....	73
5	HETEROGENEOUS NUCLEATION WITH ARTIFICIAL CAVITIES.....	75
5.1	History and Review.....	76
5.2	Cavity Fabrication Methods.....	80
5.2.1	Lithography.....	80
5.2.1.1	Photomask design.....	82
5.2.1.2	Spin coating	83
5.2.1.3	Pattern transfer.....	85
5.2.2	DRIE Etching.....	85
5.2.3	Wafer Cleaving Procedure.....	87
5.2.4	Wafer Cleaning	87
5.3	Cavity Measurements.....	88
5.4	Experimental Facilities	90
5.5	Gas Nucleation Experimental Results for Water	92
5.5.1	Effect of Backpressure on Gas Nucleation Bubble Activation.....	92
5.5.2	Activation of an Array of Cylindrical Cavities Using Gas Nucleation	93
5.5.3	Activation of an Array of Cylindrical Cavities in Pool Boiling	95

5.5.4 Gas Nucleation Experiments with a Cavity Matrix	99
5.5.5 Activation of Different Shape Cavities Using Gas Nucleation	100
5.6 Discussion	101
5.7 Summary	106
6 CONCLUSIONS AND RECOMMENDATIONS	107
6.1 Accomplishments and Findings	107
6.2 Recommendations for Future Research	110
APPENDIX	
A BRASS/WATER STATIC CONTACT ANGLE MEASUREMENTS.....	111
B STAINLESS STEEL/WATER STATIC CONTACT ANGLE MEASUREMENTS	112
C CAVITY MEASUREMENTS.....	113
D LIQUID PROPERTIES AND POOL BOILING DATA.....	118
LIST OF REFERENCES	121
BIOGRAPHICAL SKETCH	127

LIST OF TABLES

<u>Table</u>	<u>page</u>
2.1 Contact angle measurements.....	21
5.1 Cavity design dimensions in area 2 of the photomask.....	83
5.2 Cavity design dimensions in area 3 of the photomask.....	83
5.3 Silicon wafer specification.....	88
5.4 Cylindrical cavities measurements.....	89

LIST OF FIGURES

<u>Figure</u>	<u>page</u>
1.1. Formation of heterogeneous nucleation sites.....	2
2.1. Gas nucleation apparatus used by Brown.....	9
2.2. Schematic diagram of the gas nucleation facility.....	12
2.3. Overview of the low-pressure test section.....	13
2.4. Exploded view of the test section.....	14
2.5. Overview of the high-pressure test section.....	15
2.6. Viatran pressure transducer calibration curve.....	17
2.7. Thermocouple calibration curve.....	18
2.8. Liquid droplet configuration.....	19
2.9. Typical water drops in static contact with the stainless steel surface.....	20
2.10. A typical water drop in static contact with the brass surface.....	20
2.11. Ethanol drop spreading on a stainless steel surface.....	22
2.12. A typical image of gas nucleation sites on the brass surface.....	24
2.13. A typical image of gas nucleation sites on the stainless steel surface.....	24
2.14. Variation of nucleation site density with $\frac{\Delta P}{2\sigma}$ for brass surface using water.....	25
2.15. Variation of nucleation site density with $\frac{\Delta P}{2\sigma}$ for stainless steel surface using water.	25
2.16. Variation of nucleation site density with $\frac{\Delta P}{2\sigma}$ for brass surface using ethanol.....	26

3.1. Assembled view of pool boiling chamber.....	28
3.2. Cylindrical heater and heat transfer surface used in pool boiling experiments.	29
3.3. Schematic drawing of brass cylinder installation.....	30
3.4. Validyne P2 pressure transducer calibration curve.....	31
3.5. Measured temperature distribution with water on brass surface.....	32
3.6. Measured temperature distribution with ethanol on brass surface.....	34
3.7. Measured temperature distribution with water on stainless steel surface.....	34
3.8. Measured temperature distribution with ethanol on stainless steel surface.	35
3.9. Measured temperature distribution with ethanol on the mirror-finish brass surface.	35
3.10. Heat flux as a function of wall superheat with water on brass surface.....	36
3.11. Heat flux as a function of wall superheat with ethanol on brass surface.	36
3.12. Heat flux as a function of wall superheat with water on stainless steel surface.	37
3.13. Heat flux as a function of wall superheat with ethanol on stainless steel surface....	37
3.14. Heat flux as a function of wall superheat with ethanol on polished brass surface... 38	
3.15. A typical image of pool boiling nucleation sites.....	39
3.16. Deposits on the brass surface.....	39
3.17. Deposits on the stainless steel surface.....	39
3.18. Variation of nucleation site density for water on brass surface using gas nucleation and pool boiling.....	41
3.19. Variation of nucleation site density for water on stainless steel surface using gas nucleation and pool boiling.....	42
3.20. Variation of nucleation site density for ethanol on brass surface using gas nucleation and pool boiling.....	43
3.21. Variation of pool boiling nucleation site density for ethanol on brass surface.....	45
3.22. Variation of pool boiling nucleation site density for ethanol on stainless steel surface.....	46

3.23. Variation of pool boiling nucleation site density for ethanol on coarse and polished brass surfaces.....	47
3.24. Dehydrogenation conversion rate with the temperature.....	50
4.1. Condition for the gas entrapment (Wang).....	52
4.2. Condition for gas entrapment (Bankoff).....	53
4.3. A typical x-z surface profile using VSI.....	58
4.4. Cavity identification diagram.....	59
4.5. Different gas/liquid interface configurations for cavities residing inside a cavity. ...	62
4.6. Cavity dimension with gas/liquid interface at cavity mouth.....	63
4.7. Cavity mouth diameter distributions for brass surface.....	65
4.8. Cavity mouth diameter distributions for stainless steel surface.....	65
4.9. Cavity half-cone angle distribution for brass surface using the linear scale.....	67
4.10. Cavity half-cone angle distribution for brass surface using the log-log scale.	67
4.11. Cavity half-cone angle distribution for stainless steel surface using the linear scale.	68
4.12. Cavity half-cone angle distribution for stainless steel surface using the log-log scale.....	68
4.13. Comparison between measured and predicted nucleation site density on brass surface.....	71
4.14. Comparison between measured and predicted nucleation site density on stainless steel surface.....	72
4.15. Comparison between measured and predicted nucleation site density on stainless steel surface within low pressure change range.....	72
4.16. Comparison between measured and predicted nucleation site density on brass surface using water.....	74
4.17. Comparison between measured and predicted nucleation site density on stainless steel surface using water.....	74
5.1. Convex vapor meniscus protruding from a cylindrical cavity.....	79

5.2. Schematic drawing of liquid/vapor interface.	80
5.3. Lithography process.	81
5.4. Photomask overview.	82
5.5. Schematic drawing of the photomask.	84
5.6. Deep reactive ion etching process.	86
5.7. Three-dimensional profile of cylindrical cavity with 60 μm mouth diameter and 45 μm depth.	89
5.8. 2-D measurement of cylindrical cavity with 60 μm mouth diameter and 45 μm depth.	90
5.9. Validyne differential pressure transducer calibration curve.	92
5.10. Layout of cylindrical cavities on silicon surface.	93
5.11. The influence of backpressure on gas bubble activation.	94
5.12. Typical images of bubble activation on cavities with different diameters.	96
5.13. Comparison between measured and predicted gas bubble incipience.	97
5.14. Comparison between measured and predicted boiling incipience.	98
5.15. Gas bubble activation on a 10 \times 10 matrix of 10 μm cylindrical cavities.	100
5.16. Gas bubble activation on cavities with different shapes.	101
5.17. The influence of cavity shape on gas bubble activation.	102
5.18. Vapor trapping mechanism in cylindrical cavities.	105

NOMENCLATURE

a	baseline length of the liquid drop, mm
A	surface area, cm^2
b	protrusion height of the liquid drop, mm
d	cavity diameter, μm
D	cylindrical cavity mouth diameter, μm
$f(d)$	probability density function for finding cavities with diameter d , μm^{-1}
$g(\beta)$	probability density function for finding cavities with half cone angle β , rad^{-1}
h	height of the gas/liquid interface above the cavity, μm
h_{fg}	latent heat of vaporization, J/kg
H	distance between peaks, μm
H_{cav}	cavity depth, μm
n/A	nucleation site density, cm^{-2}
N/A	number of cavities per unit area, cm^{-2}
P	pressure, kPa
q''	heat flux, w/m^2
r	radius of curvature, μm
r_c	critical cavity radius, μm

R cylindrical cavity radius, μm

T_{sat} saturation temperature, $^{\circ}C$

Greek symbols

β half cone angle, rad

Δp change in pressurization, MPa

μ_d mean of the cavity diameter distribution, μm

θ liquid solid contact angle, rad

σ liquid/gas interfacial surface tension, N/m

σ_d standard deviation of the cavity diameter distribution, μm

ΔT_{sat} wall superheat, $^{\circ}C$

$(\Delta T_{sat})_{inc}$ wall superheat at the incipient point, $^{\circ}C$

μ_{β} mean of the cavity half cone angle distribution, rad

σ_{β} standard deviation of the cavity half cone angle distribution, rad

ρ_v density of vapor, kg/m^3

ψ_{min} minimum cavity side angle, rad

Subscripts

b boiling

cav cavity

inc incipience

min minimum

max maximum

meas measured

nc	natural convection
sat	saturation
l	liquid
v	vapor
w	surface

Abstract of Dissertation Presented to the Graduate School
of the University of Florida in Partial Fulfillment of the
Requirements for the Degree of Doctor of Philosophy

HETEROGENEOUS NUCLEATION AND INFLUENCE OF SURFACE STRUCTURE
AND WETTABILITY

By

Yusen Qi

May 2005

Chair: James F. Klausner

Major Department: Mechanical and Aerospace Engineering

This work explores the physical mechanisms governing heterogeneous nucleation and leads to a new area of bubble nucleation study.

Gas nucleation and pool boiling experimental facilities have been fabricated. The fluids used for this study, water and ethanol, are moderately wetting and highly wetting, respectively. Extensive gas nucleation experiments have been carried through on copper and stainless steel surfaces. In order to compare with the gas nucleation data, nucleation site density has also been measured for saturated pool boiling on brass and stainless steel surfaces with the same surface finishes. Detailed measurements of the surface microstructure have been made using a vertical scanning interferometer. A criterion for identifying potential cavities from surface topography data on surfaces has been provided. Distributions for cavity sizes and half-cone angles have been identified and a statistical model has been used to predict the resulting nucleation site density.

It has been observed that nucleation sites are substantially more populated on the brass surface compared with the stainless steel surface. The variations in the surface structure play an important role in the observed difference. However, due to the large uncertainty in the probability of finding cavities that satisfy the gas trapping criteria, the statistical method does not appear to be useful for predicting nucleation site density on surfaces with randomly distributed cavities.

Using ethanol it has been observed that few sites are active on the brass and the stainless steel surface during gas nucleation experiments. However, nucleation sites readily form in large concentration on both the brass and stainless steel surfaces during pool boiling. The comparison of nucleation site density for pool boiling and gas nucleation casts doubt on the general assumption that heterogeneous nucleation in boiling systems is exclusively seeded by vapor trapping cavities.

Artificial cavities with various sizes and shapes have been manufactured from silicon to study the bubble incipience. The incipience conditions observed for water using both gas nucleation and pool boiling support Cornwell's contact angle hysteresis theory for vapor trapping cavities. The results suggest that the theoretical considerations required for a deterministic model for incipience from vapor trapping cavities during boiling is more complex than previously hypothesized.

CHAPTER 1 INTRODUCTION

1.1 Heterogeneous Nucleate Boiling

Boiling heat transfer has attracted the interest of many researchers over the past 70 years because large heat transfer rates and convection coefficients may be achieved in the nucleate boiling with a small temperature difference. This regime starts from the onset of nucleate boiling to fully developed nucleate boiling. It is applied extensively in various heat exchanger and energy conversion systems. Also nucleate boiling can be found in the cooling of high-energy dissipation electrical components. The high heat flux energy transfer associated with the nucleate boiling depends on the nucleation, growth, and departure of vapor bubbles from the heating surface.

There are two types of nucleation, homogeneous nucleation and heterogeneous nucleation. Homogeneous nucleation boiling occurs in the liquid in which there is no contact with any other foreign substance or surface. In homogeneous nucleation, the nucleation begins when a very small volume of liquid molecules (embryo) reaches a vapor state. This embryo becomes the basis for further growth. In order for homogeneous nucleation to occur, a substantial amount of energy must be available, and thus a very large superheat is required for homogeneous nucleation. Boiling on surfaces is typical associated with low superheat, and thus another mechanism is responsible for the spontaneous growth of vapor bubbles.

Heterogeneous nucleation occurs on surfaces when pre-existing vapor spontaneously grows and generates vapor bubbles. It is supposed that the presence of

trapped gas or vapor in small cavities on heating surfaces seeds heterogeneous nucleation, as illustrated in Fig. 1.1. Nucleate boiling is usually initiated with heterogeneous nucleation.

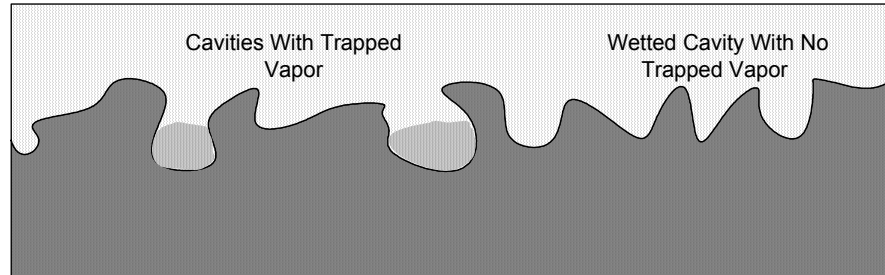


Figure 1.1. Formation of heterogeneous nucleation sites.

1.2 Current Understanding of Heterogeneous Nucleation

To design an effective boiling system, it is necessary to predict the average heat flux, which is closely related to the active nucleation site density, the average frequency for bubble departure and the bubble diameter at departure. Such heat flux modeling can be achieved by assuming that the total heat flux on the heating surface is controlled by two mechanisms, bubble detachment and free convection. Mikic and Rohsenow (1969) used the following relation to model the nucleate pool boiling heat flux:

$$q'' = (1 - A)q''_{nc} + Aq''_b \quad (1.1)$$

Here, q''_{nc} and q''_b are the natural convection and boiling components of the total heat flux, respectively, and A is the area influenced by the nucleation sites. Constant wall superheat was assumed over the heated surface. Lorenz et al. (1974) also proposed a physical model relating surface characteristics to nucleate pool boiling heat flux. Recently, Bergez (1995) suggested a boiling heat transfer model by accounting for the heating surface temperature variations. However, none of the existing theoretical and mechanistic models are capable of satisfactorily predicting the rate of the heat transfer

during nucleate boiling over a wide parameter space. The main reason is that one of the most important modeling parameters, nucleation site density, is very difficult to predict although many experimental and theoretical investigations conducted in recent years allow the determination and analysis of most of the fundamental boiling parameters.

It has been the goal of researchers for the past 70 years to understand heterogeneous nucleation in boiling systems and develop correlations and models to predict its dependence on surface structure, wettability and wall superheat. Corty and Foust (1955) recognized that boiling takes place on surfaces with irregularities and suggested that vapor trapped in these surface irregularities served as nucleation sites. This hypothesis was confirmed by Clark et al. (1959) using micrographs of the heating surface. In their experiments, they found that pits and scratches in the zinc and aluminum surfaces were active sites using ether and pentane as the boiling liquids. And they concluded that neither the grain boundary nor atomic density would have an effect on boiling nucleation. Gaertner and Westwater (1960) measured the nucleation site density for a water and nickel-salt solution boiling on a copper surface. During the boiling process nickel was deposited on the heater surface. The number of active nucleation sites was determined by counting the number of areas with no nickel deposition. It was found that $\frac{n}{A}$ is proportional to q_w^2 , where $\frac{n}{A}$ is the nucleation site density and q_w is the wall heat flux. Kurihara and Meyers (1960) demonstrated that $\frac{n}{A}$ is highly dependent on the roughness of the boiling surface. By conducting boiling experiments on a flat plate with different pure liquids, they proposed that the boiling coefficient is proportional to $\left(\frac{n}{A}\right)^m$, where m is a constant.

An important breakthrough in quantitatively relating the heating surface microstructure to nucleation phenomena was made by Griffith and Wallis (1960). Using a conical geometry as an idealized surface cavity, they identified a minimum cavity mouth radius (critical radius r_c) required to generate vapor bubbles. They also demonstrated that for a specific surface-fluid combination the nucleation site density was correlated with the inverse of r_c at low heat flux, expressed as $\frac{n}{A} = c\left(\frac{1}{r_c}\right)^m$, where $\frac{n}{A}$ is the nucleation site density, r_c is the critical radius, and c and m are empirically determined constants. At higher heat flux the correlation appeared to break down. Hsu (1962) accounted for the liquid thermal boundary layer surrounding a static vapor embryo using a conduction analysis in pool boiling and suggested there exists both a minimum and maximum cavity radius which will permit the incipience of vapor bubbles. Zeng and Klausner (1993) measured nucleation site density in flow boiling. Their data were re-analyzed by Thorncroft et al. (1997), and it was demonstrated that both the maximum and minimum cavity radii are important in flow boiling nucleation. Studying pool boiling heat transfer using different surface finishes under different pressures, Bier et al. (1978) found that the heat transfer coefficient cannot be correlated with a single surface parameter such as average roughness. Others who have studied nucleation site density include Barthau (1992), and Luke and Runowski (1997).

Tong et al. (1990) demonstrated that the presence of non-condensable gas as well as contact angle hysteresis can exert a large influence on the incipience point of vapor bubbles in pool boiling systems. The contact angle hysteresis has a large impact on highly wetting fluids. Cornwell (1982) also reported on the effects of contact angle hysteresis on incipience.

There is also a serious limitation in the study of bubble incipience. Since the pioneering work of Griffith and Wallis (1960) to identify the bubble incipience condition, this model has been widely used to predict the heat flux in boiling systems. However, it is impossible to manufacture a precise cavity using a steel gramophone needle, and thus it may undermine the usefulness of this incipience model. Cornwell (1977) conducted a very detailed study of the geometry of naturally formed nucleation site cavities in pool boiling. In general, the cavity sizes of actual sites tend to be slightly smaller than r_c . Brauer and Mayinger (1992) have given an overview of the models that have been proposed for the prediction of boiling incipience. They suggested that experiments should be conducted on simple geometries and involved as few variables as possible.

The difficulty level in understanding heterogeneous nucleation in boiling is substantial due to the uncertainty in micro surface structure and contact angle hysteresis, on which the nucleation site density is highly dependent. Yang and Kim (1988) successfully predict the nucleation site density based on the understanding of statistic information of cavity size and cavity half-cone angle distributions on a mirror surface. The maximum superheat tested is only $2.6\text{ }^\circ\text{C}$.

1.3 Outline of the Current Investigation

The objectives of the current work are the following:

- (1) Investigate the usefulness of the gas nucleation technique to assist in the prediction of pool nucleate boiling site density.
- (2) Develop a methodology for nucleation site prediction on commercial surfaces using statistical models.
- (3) Study the effect of wettability on nucleation.
- (4) Explore bubble incipience on the precisely manufactured cavities.

A gas nucleation experimental facility, described in Chapter 2, has been designed, constructed, and tested which allows the measurement of nucleation site density using different surface samples under appropriate pressurization change. Extensive gas nucleation experiments have been carried through on brass and stainless steel surfaces using water and ethanol. Nucleation site density measurements have been made for a change in pressurization up to 8.5 atmospheres. To demonstrate the validity of the gas nucleation technique to predict the bubble population data, a comparison with boiling nucleation is also performed. The boiling facility and experimental results are described in Chapter 3. A high speed CMOS digital camera is used to capture the nucleation site images. The brass and stainless steel surfaces used in the saturated pool boiling experiments are prepared in the same way as in the gas nucleation experiments. Two fluids used in this study, distilled water and ethanol, are moderately wetting and highly wetting, respectively. By applying the different combination of liquids and surface structure, the effect of wettability is also explored.

Chapter 4 presents an investigation of a statistical model to predict the nucleation site density. Detailed measurements of the surface microstructure have been made using a vertical scanning interferometer. Distributions for cavity sizes and half-cone angles have been identified; a method to identify the vapor trapping cavity has been developed; and a statistical model has been used to predict the resulting nucleation site density.

Artificial cavities are fabricated on a silicon wafer by micro-fabrication techniques. The manufacturing process is described in Chapter 5. Bubble incipience in artificial cavities has been studied using gas nucleation and pool boiling. Water and ethanol have both been used as the bulk fluid with cylindrical cavities, as well as those with a triangle,

square, and rectangle shape cross section. Nominal cavity sizes range from 8 to 60 μm . The data supply the experimental basis for further understanding of bubble incipience. Using the gas nucleation, the effect of backpressure on bubble incipience is also discussed.

A summary of important conclusions from this work is offered in Chapter 6. Finally recommendations are proposed for further study.

CHAPTER 2 GAS NUCLEATION TECHNIQUE

2.1 Introduction and Literature Survey

2.1.1 Bubble Counting Method

Many researchers including Clark et al. (1959), Kurihara and Myers (1960), Griffith and Wallis (1960), Mikic and Rohsenow (1969), and Lorenz et al. (1974) have attempted to visually count the number of active nucleation sites on a given surface area, either by direct observation, still pictures, or high speed photography. The counting was limited to low densities, typically n/A less than 100 cm^{-2} , because the large number of vapor bubbles suspended in the boiling bulk liquid or the vapor column formed on the heater surface will obstruct the view of the heater surface at a higher heat flux.

Gaertner and Westwater (1960) used an electroplating process to identify nucleation sites during nucleate boiling. The problem here is that the deposition of the nickel layer on the copper surface may affect the surface characteristics although they were able to identify up to 175 sites/cm^2 . Using a high-speed infrared camera, Sgheiza and Myers (1985) identified active nucleation sites by recording the temperature pattern of a thin metal sheet. Despite all these merits that make it possible to count the higher nucleation site density, these methods either undermine the bubbling behavior or need a special type of heater. Barthau (1992) developed an optical method to count the dark spots on a horizontal tube and claimed that it succeeded in measuring up to $5000 \text{ sites per cm}^{-2}$.

In this study, a simple visual counting method is used. The method is not intrusive to the boiling process, although the upper density limit is low.

2.1.2 Gas Nucleation Study

Brown (1967) used the apparatus shown in Fig. 2.1 to extensively investigate supersaturated gas bubble formation from naturally formed cavities and compared the results to bubble formation in boiling systems.

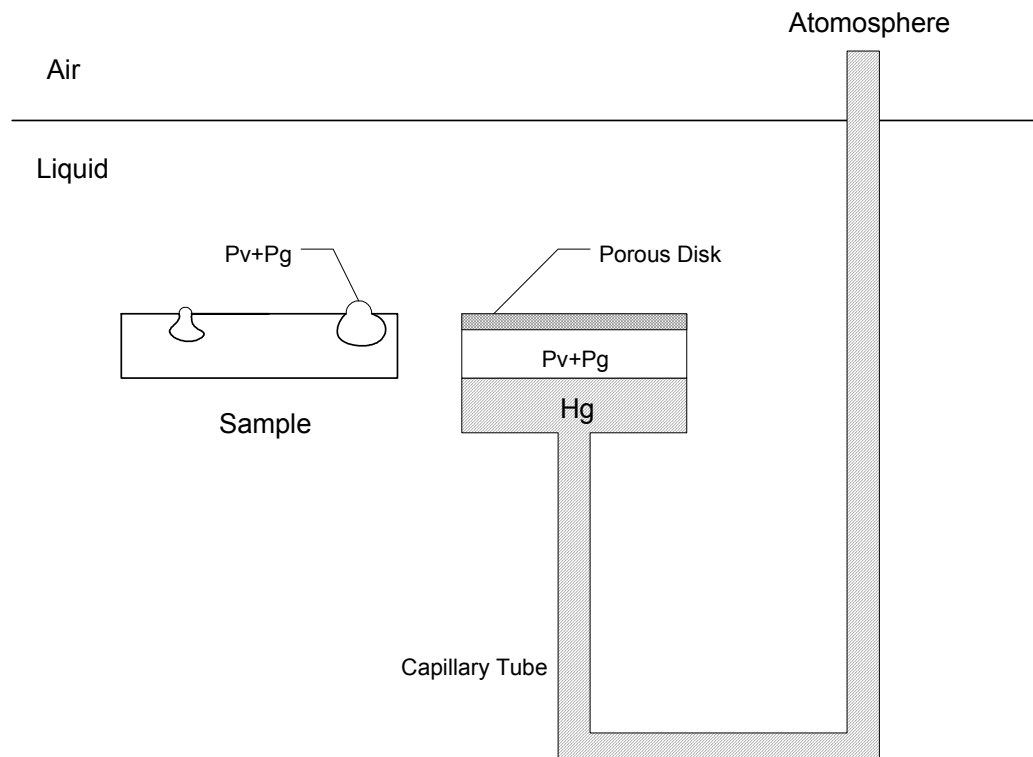


Figure 2.1. Gas nucleation apparatus used by Brown.

Eddington et al. (1978) and Eddington and Kenning (1979) have extensively compared nucleation via gas bubbling with that in nucleate boiling. All of the experiments used distilled water as the heat transfer fluid. They suggested that the nucleation site density model might be complicated by the thermal interference and sites interference. When comparing nucleation site density measured as a function of the critical cavity radius by gas nucleation with those measured during nucleate boiling, the

comparison was not satisfactory. However, Kenning (2000) re-analyzed the data of Eddington et al. by accounting for the nonlinear variation of the saturation pressure with temperature and found improved agreement. Yet the nucleation site density measured during gas nucleation experiments tends to be greater than that measured for nucleate boiling experiments with the same critical cavity mouth radius.

The advantage of using gas nucleation over boiling experiments is that it is easier to count the nucleation sites and the experiments are potentially easier to operate. Supersaturated gas bubble growth rates in an inorganic fluid are very slow, while they are more rapid in organic fluids due to the low surface tension. When addressing the surface characteristics and wettability effects on heterogeneous nucleation the gas nucleation technique has inherent advantages. Gas nucleation eliminates the possibility of thermal interference between adjacent sites, which has been suggested as a mechanism for suppressing boiling nucleation. Also, due to the slow growth rate of gas bubbles, dynamic influences related to vapor bubble growth, departure, and turbulence are absent. These advantages of the gas nucleation technique provide a sufficient incentive to explore its usefulness for predicting nucleation site density in boiling systems.

2.2 Gas Nucleation Facility Overview

A gas nucleation facility, shown in Fig. 2.2, was designed and fabricated for the present experiments. The operation of the facility is similar to that used by Eddington et al. (1978). The 20-liter liquid storage epoxy-lined steel tank is half filled with liquid. Valves 5, 6, 8, and 9 are opened and a portion of the facility is pressurized with a charged air cylinder, and the degree of pressurization is controlled with a pressure regulator, located between valves 8 and 9. Valve 9 is closed, and a variable speed magnetically driven micro-pump, excellent in preventing leakage, is used to circulate pressurized

liquid through the liquid storage tank. Either water or ethanol, used in the current study, is sprayed into the liquid storage tank. It gradually becomes saturated with air. The liquid is allowed to circulate for 40 minutes to insure that it becomes fully saturated with dissolved air. Valves 5 and 6 are installed to allow drainage of the liquid from the system when necessary. The inline electric heater is connected to the system in order to better control the liquid temperature. The function of valve 7 is to release the system pressure. With valves 3 and 4 closed, valve 2 is opened and then valve 1 is opened in sequence. Adjusting the valves in the sequence described allows the test section to equilibrate to the same pressure as the liquid storage tank. The test section is mounted horizontally 30 cm below the centerline of the liquid tank. By gravity, liquid from the storage tank fills the test section while dissolved gas remains in solution. The pressure and temperature of the liquid in the test section are recorded. Valves 1 and 2 are closed and valve 3 is opened, which de-pressurizes the test section. The resulting temperature and pressure are recorded again. The waiting time between the filling test section and depressurization is on the order of 10 seconds. As the test section is depressurized, nucleation sites form on the test surface, which is photographed with a high-resolution digital camera from a side view. Using back lighting, each bubble directs the light toward the camera lens, and each individual bubble is identified by its bright spot. After recording all necessary data, the test section was drained and the sample surface was dried by blowing dry air on the top of the surface with the help of radiation from a 1000 W mercury lamp.

2.3 Test Section Design

Two transparent test sections with the same dimensions have been fabricated in this study: (1) A low pressure test section that can accommodate 3 bars and (2) A high pressure test section that can accommodate 10 bars.

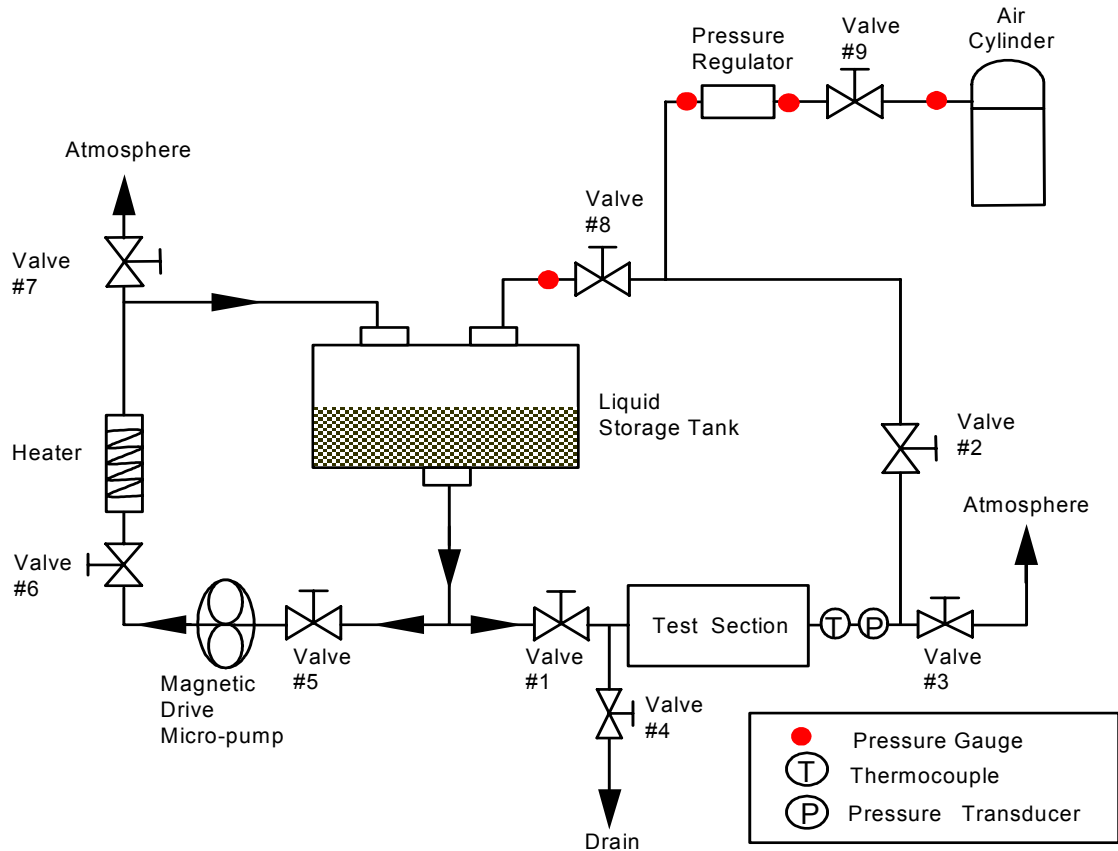


Figure 2.2. Schematic diagram of the gas nucleation facility.

2.3.1 Low Pressure Test Section

An assembled view of the low-pressure test section is shown in Fig. 2.3. The rectangular channel of the test section is fabricated from 19 mm thick polycarbonate with an inner cross section of 30.48 mm wide by 17.4 mm high. The test section must be designed with sufficient structural strength to withstand the operating pressure. After a considerable effort to determine an appropriate adhesive with slow drying speed and sufficient bond strength, urethane adhesive for polycarbonate is applied to bond together this test section. With the aid of a vacuum applied to the test section, a layer of epoxy is also applied on the joints of the polycarbonate pieces to further prevent leakage. The maximum pressure, which the final test section can accommodate, is 3 bars. The bottom

wall of the rectangular channel has a circular recess with 5 mm depth in which a 25.4 mm diameter metallic sample may be inserted. Each end of the channel inserts into a 38 mm polycarbonate flange that allows it to connect with the experimental facility.

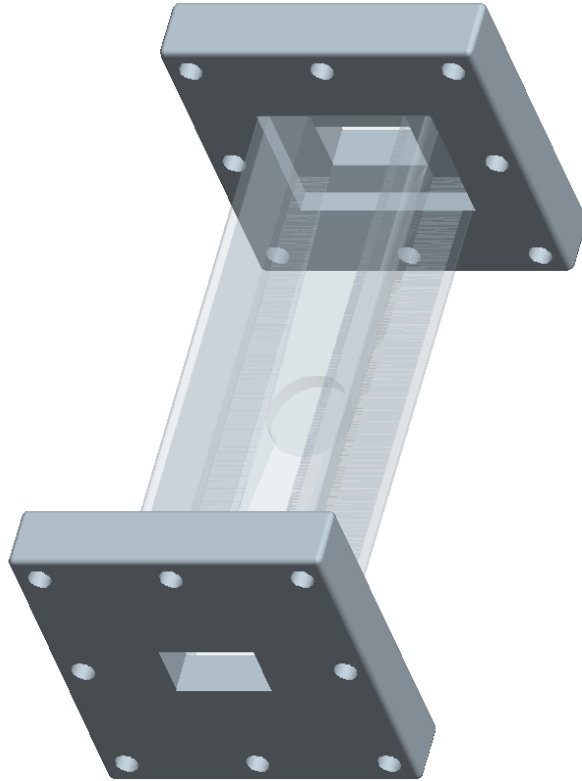


Figure 2.3. Overview of the low-pressure test section.

The interior details of the test section are illustrated with an exploded view shown in Fig. 2.4. The T shape of the top and bottom wall provides more contact area, and thus increases the bonding strength.

2.3.2 High Pressure Test Section

After significant struggles in the selection of various plastic adhesives and epoxy sealants, a gasket method was adopted to construct the high pressure test section.

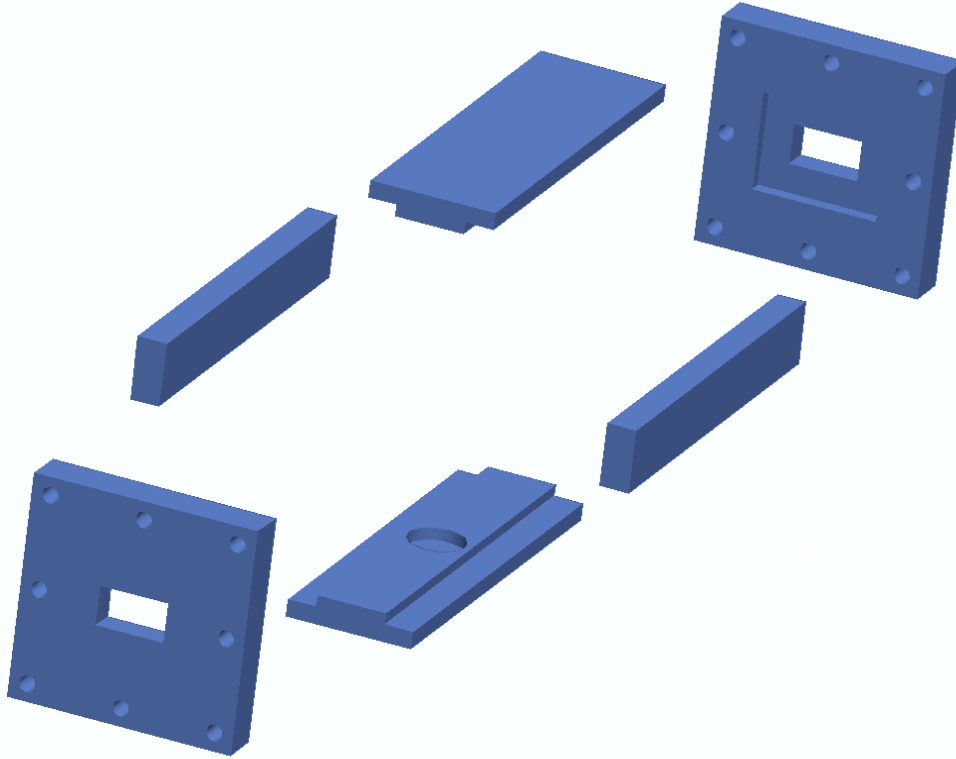


Figure 2.4. Exploded view of the test section.

A new transparent test section that can accommodate 10 bars pressure has been successfully fabricated in the lab. The assembled drawing of the test section is shown in Fig. 2.5. The visual portion of the test section is constructed from polycarbonate. Two thick metallic plates cover the top and bottom to prevent excessive polycarbonate deformation when under high pressure. All mating surfaces are sealed with viton gaskets, which provide a reliable way to prevent fluid leakage during operation. The advantage of gasket method over adhesives and epoxies is that it is easier to disassemble the whole structure without damaging the components. It saves time and cost because of the easy replacement of the components in the test section. 12 bolts are applied to tighten the rectangular channel. By correctly selecting the positions of bolts during the design process, the force is evenly distributed on the polycarbonate wall to achieve better

sealing. A thin layer of RTV sealant is applied on each end of channel before fitting the rectangular channel into the flange. This sealant is also used to cover the gap inside of the channel.

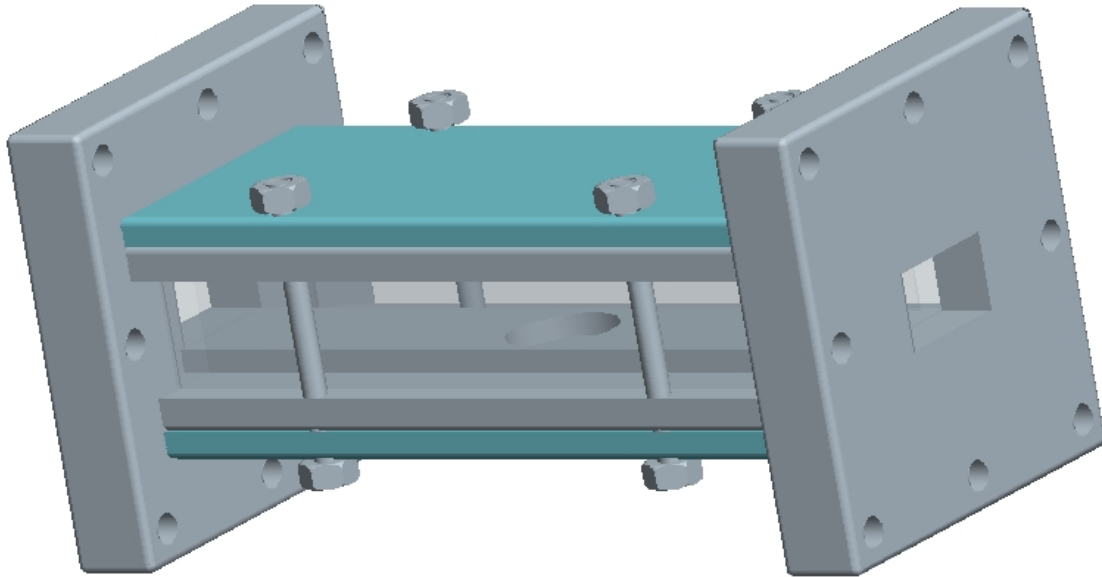


Figure 2.5. Overview of the high-pressure test section.

2.4 Surface Preparation

For the present study alloy 360 free machining (61.5% Copper, 35.25% Zinc, 3.25% Lead) brass and type 304 stainless steel surfaces have been investigated. The surface is prepared by first polishing it with 120 grit sandpaper. 400 grit silicon carbide sandpaper is used to put a final finish on the surface. Prior to inserting the metallic disk into the test section it is thoroughly cleaned with detergent solution and ethanol.

2.5 Instrumentation and Calibration

A data acquisition system has been assembled for recording the temperature and pressures during the experimental operation. The data acquisition hardware is an Access 12-8, 12 binary bit resolution and 8 channel analog-to-digit converter, interfaced with an Access AIM-16, 16 channel multiplexer card. The AIM-16 accepts and preamplifies the

analog input signals before passing them to the Access 12-8 located in an I/O slot of the host computer. The AD12-8 board and AIM-16 card were calibrated according to the manufacturer's recommendations. Appropriate gains were assigned for different channels. Channel 0 on the AIM-16 card is utilized to measure the reference temperature using a thermistor. A QUICKBASIC computer program was modified to process data using the drivers provided by the manufacturer.

The nucleating gas bubbles on the test surface are photographed with a digital imaging facility, which includes a Videk Megaplus CCD digital camera that has 1320(H) x 1035(V) pixel resolution, a computer system where an Epix 4 megabyte frame grabber card is installed to transfer the image and a Sony analog monitor with 1000 lines/inch resolution to display the image. The images were saved on the floppy disks for future analysis. After depressurizing in the test section, numerous bubbles will form on the top of the test section, so it is not possible to get a clear view from the direction normal to the sample surface. Therefore, the camera with a 50 mm macro lens was focused on the surface through the sidewall. A 100 watt light illuminates the test section from the opposite sidewall. Sigmascan image processing software is used to assist in identifying nucleation sites from the digital image.

The pressure in the test section is measured with a Viatran strain gauge type pressure transducer. The linear calibration curves, shown in Fig. 2.6, are obtained by comparing the output voltage of the pressure transducer to the liquid monometer. The temperature is measured with a single 36-gauge type E thermocouple. The calibration data and fitted curve are shown in Fig. 2.7. The uncertainty of the pressure measurement is ± 0.2 KPa and the uncertainty of the temperature measurement is ± 0.5 C. The pressure

and temperature measurements are quite simple since there is only one location where the parameters are monitored. Temperature and pressure are recorded at the exit of the test section, shown in Fig. 2.2.

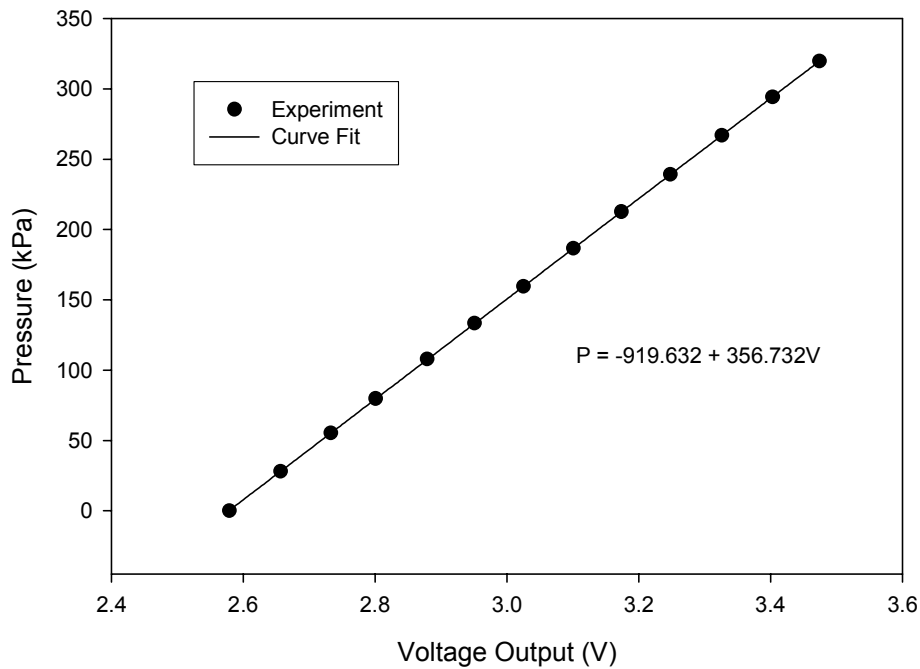


Figure 2.6. Viatran pressure transducer calibration curve.

2.6 Experimental Results

2.6.1 Static Contact Angle Measurements

The drop shape method is used to measure the static contact angle. The following are two principal assumptions used for this method: (1) the liquid drop is symmetric about the central vertical axis and (2) the interfacial tension and gravity are the only forces affecting the shape of water drop.

By measuring the shape of liquid drop on the solid surface, the slope of the tangent to the drop at the liquid-solid-gas interface line can be calculated as $\theta = 2 \tan^{-1}\left(\frac{2b}{a}\right)$, as

illustrated in Fig. 2.8. Here, θ is liquid-solid contact angle, b is the protrusion height of the liquid drop and a is the baseline length of the drop. The protocol for measuring the static contact angle is summarized in 5 steps, as listed:

- (1) Place the metal sample on a horizontal surface.
- (2) Establish the camera lens in a horizontal position.
- (3) Load the liquid in the disposable plastic syringe and dispense enough fluid to displace all the air in the needle.
- (4) Place the drop on the surface carefully so the liquid momentum does not cause further spreading of the drop. Position the needle tip above the metal surface so that the growing droplet contacts the surface and spreads due to its own weight.
- (5) Take a picture and measure the baseline length and height of drop. Optical magnification is necessary to assist the measurement in this step.

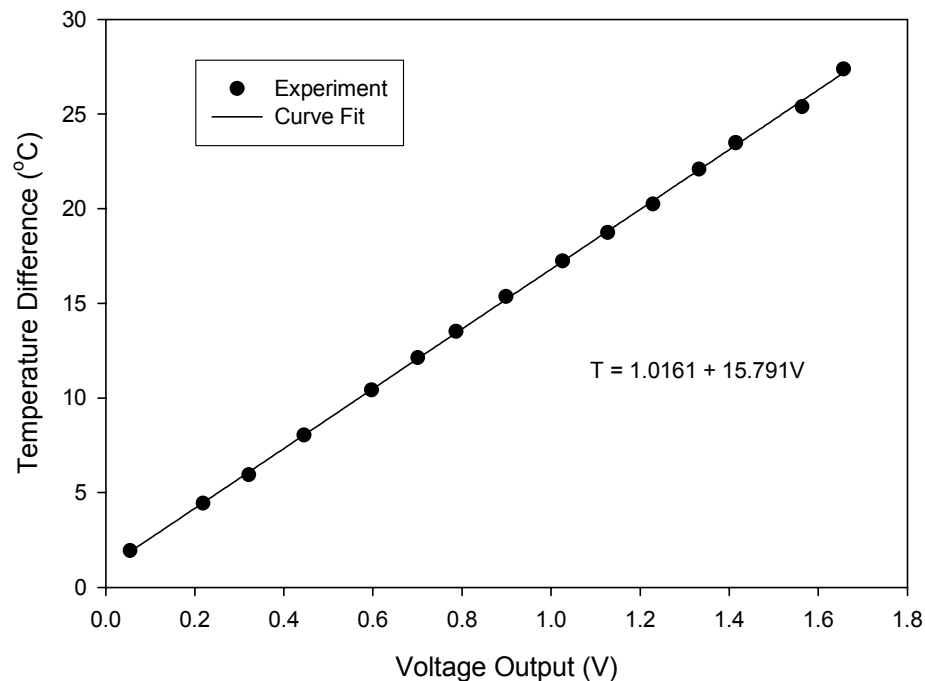


Figure 2.7. Thermocouple calibration curve.

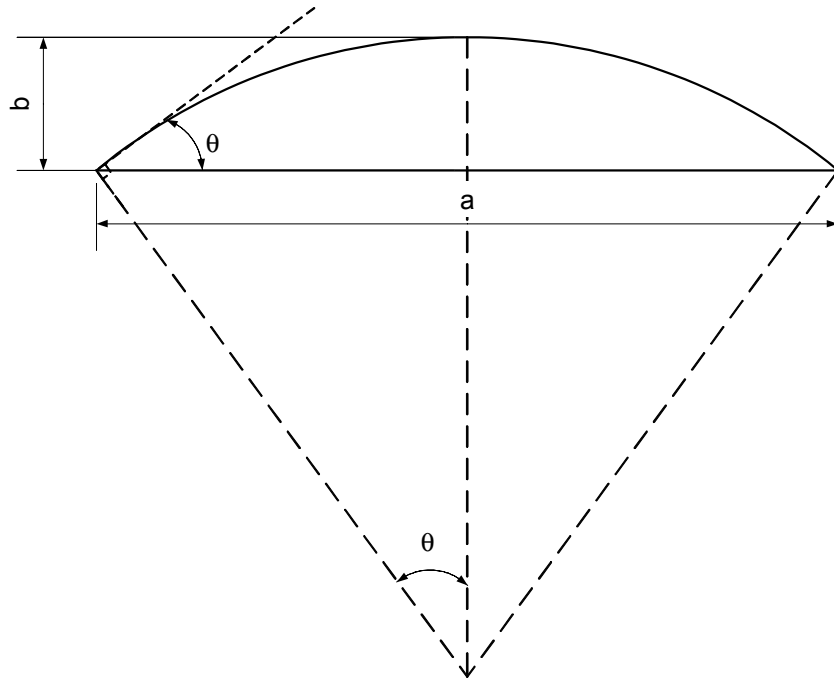


Figure 2.8. Liquid droplet configuration.

The static liquid/solid contact angles measured between the water and the stainless steel for an ensemble of 14 trials is 1.35 radians (77.4 degrees) with a standard deviation of 0.07 radians (4.2 degrees). Typical water-drop shapes on a stainless steel surface are shown in Fig. 2. 9. The static liquid/solid contact angle between the water and brass for an ensemble of 13 trials is 1.27 radians (73.1 degrees) with a standard deviation of 0.06 radians (3.7 degrees). Fig. 2.10 shows a typical drop shape of water on a brass surface. The measured data are listed in the Appendix A and B. The water is slightly more wetting on brass than on stainless steel, although the degree of wettability on both surfaces is quite similar.

Due to very high wettability of ethanol, it is not possible to measure the static liquid/solid contact angle for ethanol on sample surfaces. The measurements of advancing and receding contact angles are described in the following.

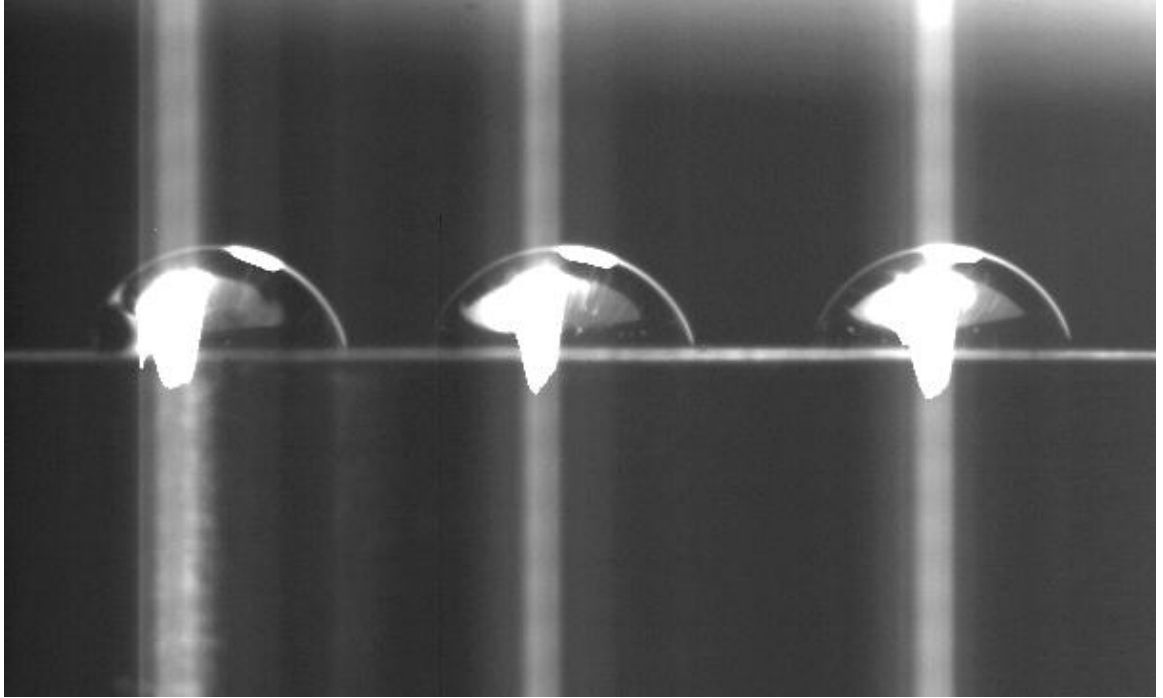


Figure 2.9. Typical water drops in static contact with the stainless steel surface.

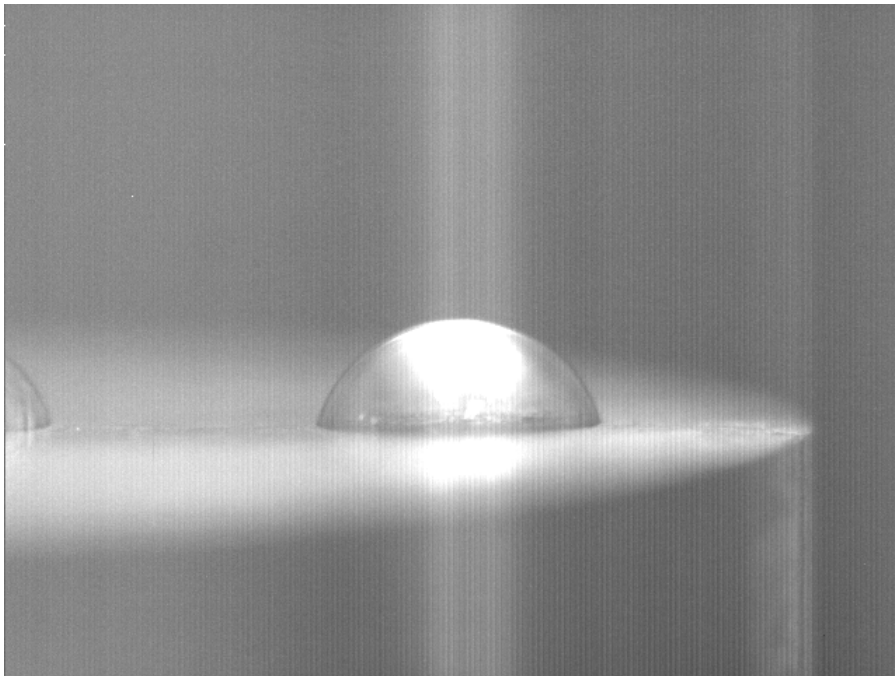


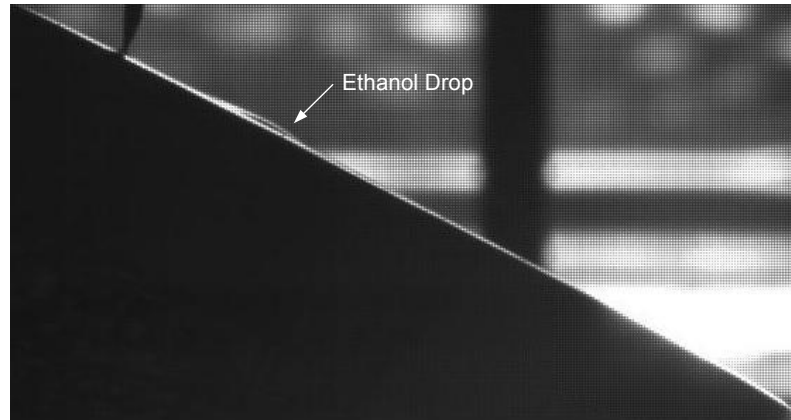
Figure 2.10. A typical water drop in static contact with the brass surface.

2.6.2 Advancing and Receding Contact Angle Measurements

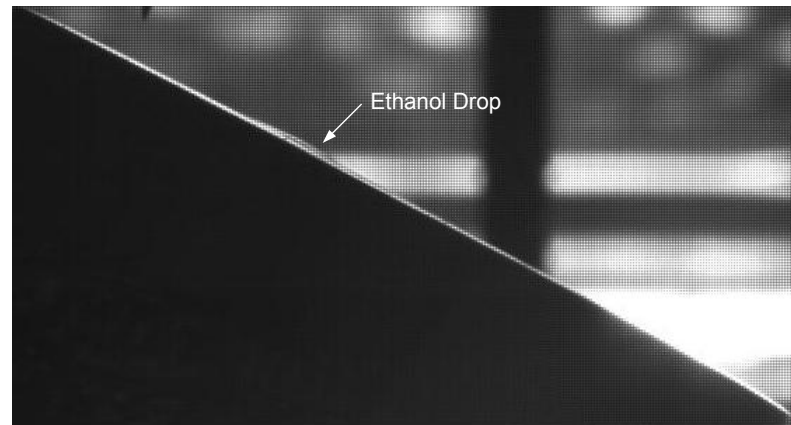
A pure ethanol drop will spread spontaneously when the metallic surfaces are mounted horizontally. Within 0.1 s the drops on both surfaces are indiscernible under 10X magnification. Here the digital camera is used to capture the dynamics using a 1000 fps frames rate. When measuring the advancing and receding angle on a 30° tilted brass sample, the ethanol drop will reach an indiscernible condition within 0.05s. The contact angle measurement is not considered reliable and is not reported. The time required for the stainless steel surface is slightly longer, about 0.15s. Figure 2.11 shows a typical ethanol drop spreading process on a stainless steel surface. The advancing and receding angles with standard deviations are listed in Table 2.1 although uncertainty remains as to whether an equilibrium condition was reached.

Table 2.1 Contact angle measurements

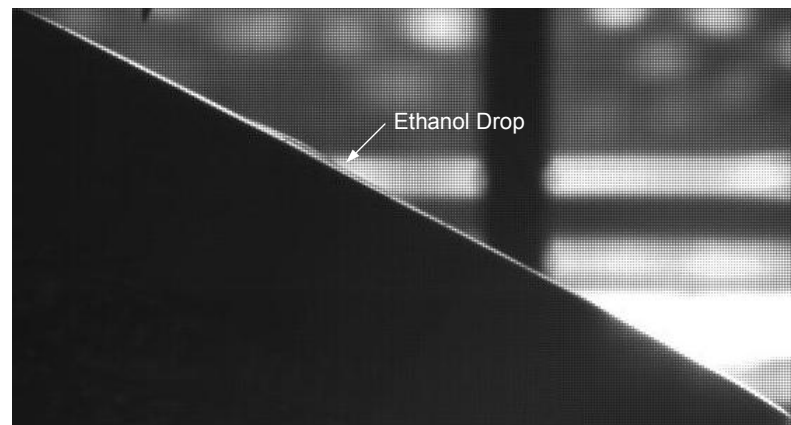
	Water	Ethanol
Brass surface	$1.27 \pm 0.06(\text{rad})$ $73.1 \pm 3.7(\text{deg})$	Not reported
Stainless steel surface	$1.35 \pm 0.07(\text{rad})$ $77.4 \pm 4.2(\text{deg})$	Advancing $0.14 \pm 0.0045(\text{rad})$ $8.0 \pm 0.26(\text{deg})$ Receding $0.10 \pm 0.0083(\text{rad})$ $5.7 \pm 0.47(\text{deg})$



0.01S after the drop is placed on the surface



0.05S after the drop is placed on the surface



0.10S after the drop is placed on the surface

Figure 2.11. Ethanol drop spreading on a stainless steel surface.

2.6.3 Nucleation Site Density Measurements Using Water

Nucleation site density measurements, n/A , have been made on the brass and stainless steel surfaces over a pressure range of 1.2-3 bars. Fig. 2.12 shows a typical image of gas nucleation sites on the brass surface and Fig. 2.13 shows the nucleation sites on the stainless steel surface. At low nucleation site density, the measurement is exact. At higher nucleation site density the measurement uncertainty is approximately $\pm 2\%$.

A total of 53 measurements have been made for the brass surface and 44 measurements for the stainless steel surface. According to classical heterogeneous nucleation theory, a gas bubble will nucleate from a conical cavity when the cavity mouth radius is greater than the critical cavity radius given by

$$r_c = \frac{2\sigma}{\Delta p} \quad , \quad (2.1)$$

where σ is the liquid/gas interfacial surface tension and Δp is the change in pressurization in the test section. Fig. 2.14 shows the variation of nucleation site density with $\frac{\Delta p}{2\sigma}$ for the brass surface while Fig. 2.15 shows that for the stainless steel surface. It is observed that the nucleation site density for the brass surface increases very rapidly with increasing $\frac{\Delta p}{2\sigma}$. Furthermore, the brass surface is observed to be very populated with gas bubbles. The nucleation site density is observed to be as high as 250 sites/cm². In contrast, the nucleation site density for the stainless steel surface does not increase as rapidly with $\frac{\Delta p}{2\sigma}$, and the largest nucleation site density observed over the pressure range considered is approximately 34 sites/cm². It is also observed that for the same change in

pressurization, the measured n/A are scattered. The data for the brass are more scattered than those for the stainless steel.

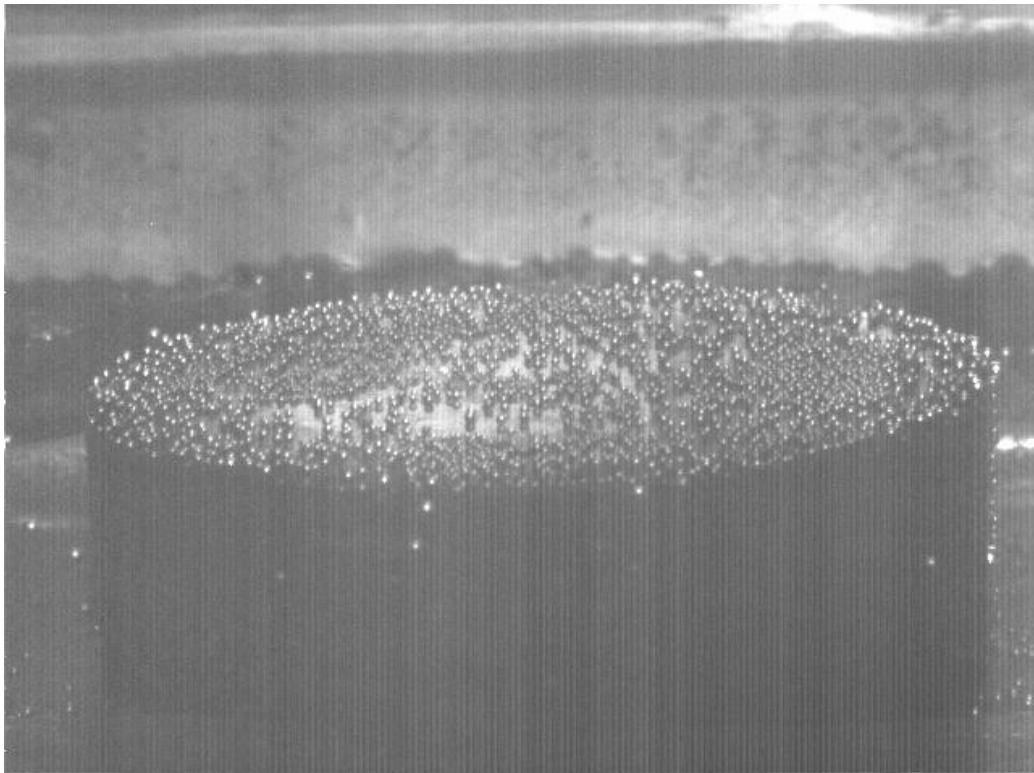


Figure 2.12. A typical image of gas nucleation sites on the brass surface.

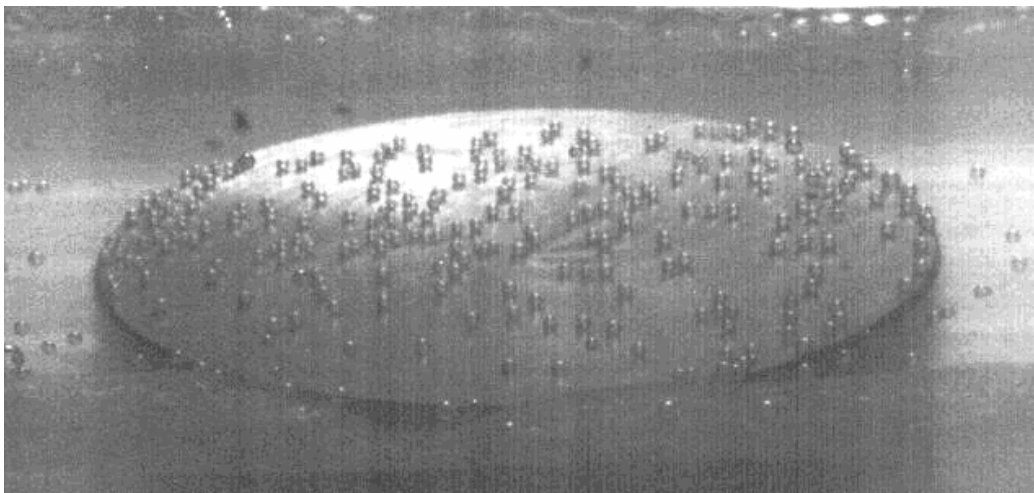


Figure 2.13. A typical image of gas nucleation sites on the stainless steel surface.

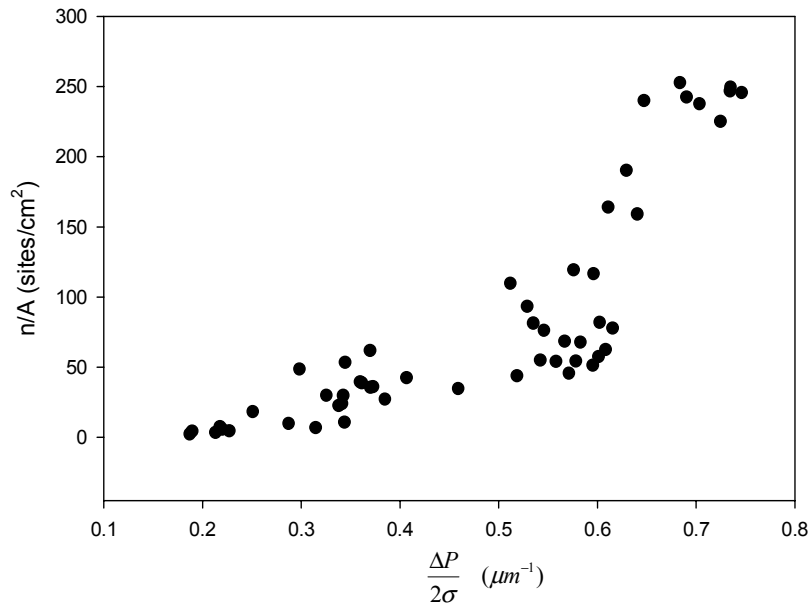


Figure 2.14. Variation of nucleation site density with $\frac{\Delta P}{2\sigma}$ for brass surface using water.

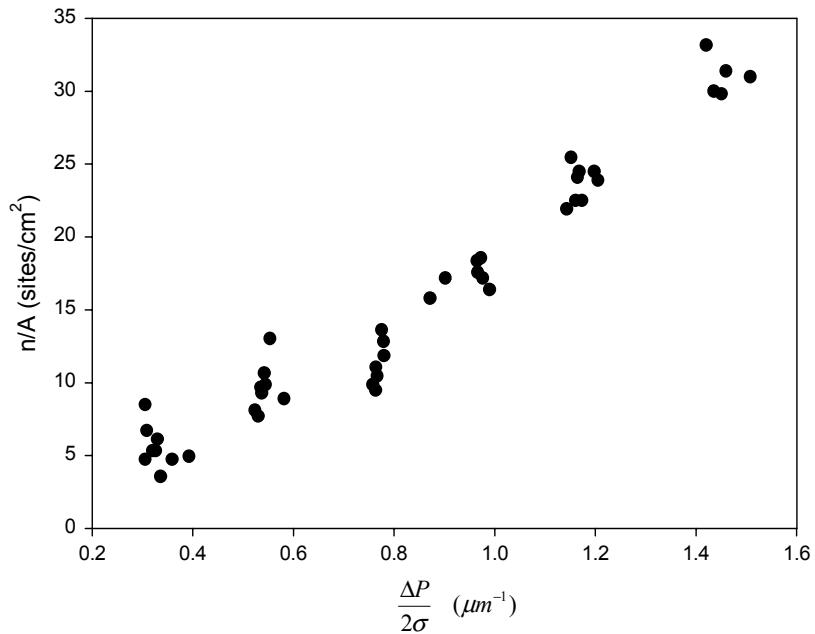


Figure 2.15. Variation of nucleation site density with $\frac{\Delta P}{2\sigma}$ for stainless steel surface using water.

2.6.4 Nucleation Site Density Measurements Using Ethanol

In order to further explore the gas nucleation characteristics, nucleation tests were also conducted on the brass and stainless steel surfaces using ethanol. Fig. 2.16 shows the variation of gas nucleation site density with ethanol on brass surface. Due to the high wettability of ethanol, most cavities on the surface are flooded. Only some very small cavities can trap vapor and thus a very high $\frac{\Delta P}{2\sigma}$ is required to activate sites for gas nucleation experiments. The increase in the number of sites activated is very small, even with an order of magnitude increase in $\frac{\Delta P}{2\sigma}$.

Ethanol gas nucleation experiments were done on the stainless steel surface with very high $\frac{\Delta P}{2\sigma}$ ($20 \mu\text{m}^{-1}$) and due to flooding, at most two nucleation sites were activated.

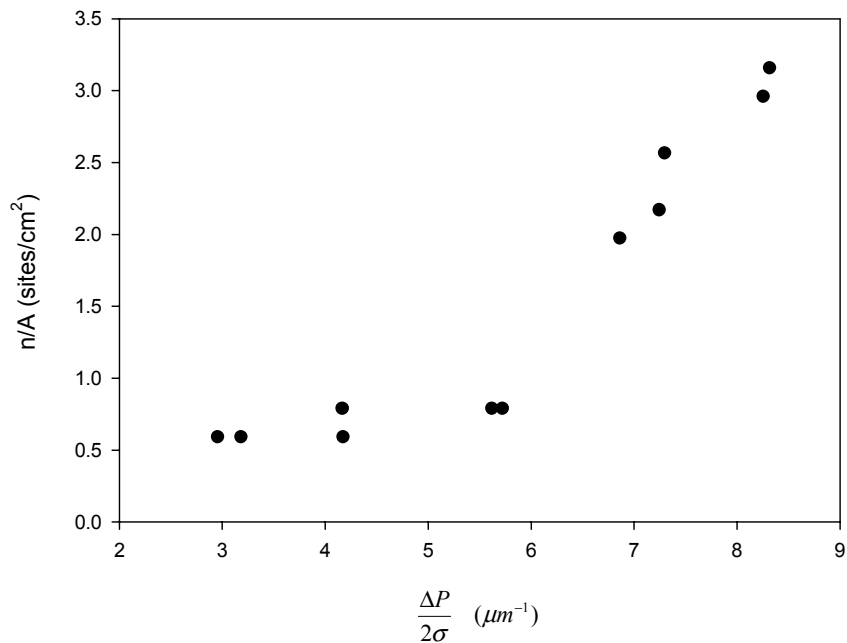


Figure 2.16. Variation of nucleation site density with $\frac{\Delta P}{2\sigma}$ for brass surface using ethanol.

CHAPTER 3 POOL BOILING TECHNIQUE

3.1 Pool Boiling Facility Overview

The purpose of fabricating this pool boiling facility is to directly compare the gas nucleation data for the same combination of surface and liquid.

A tilted assembled drawing of the pool boiling apparatus is shown in Fig. 3.1. This apparatus consists essentially of a pool boiling chamber and a liquid condenser. The boiling chamber consists of a low expansion borosilicate glass cylinder with inner diameter 101.6 mm, thickness 6.35 mm and length 0.45 m. The glass cylinder is held vertically in place between two stainless steel plates, on which the circular grooves are cut precisely to fit the glass cylinder. Holes are manufactured on the top stainless steel plate to install the discharge pipe, safety valve and pressure transducer. Heater assembly, drainpipe, liquid heater and thermocouples are installed on the bottom stainless steel plate. A viton rubber gasket lightly coated with the high temperature silicon grease is used to prevent leakage between these two plates and the glass chamber. A cooling coil that is connected with a small chiller is mounted on the upper part of the boiling chamber to maintain a constant pressure. The evaporated vapor rises to the cooling coil and the condensate returns to the bulk liquid by free circulation. The water temperature and mass flow rate passing through the cooling coil are adjustable. Accurate control of the pressure in the chamber is obtained by adjusting the heat supplied the bulk liquid and the mass flow rate of cooling water. The bulk liquid, either distilled water or ethanol, is heated by two heaters with a power of 200W each. The boiling surface, which is the

upper surface of the heater assembly, is mounted flush with the boiling chamber plate. The power to all heaters is controlled by autotransformers. The temperature of the liquid in the boiling chamber is measured with a type E thermocouple probe suspended 30 mm above the boiling surface. The boiling chamber was filled to a height of 70 mm with liquid that is allowed to boil for 1 hour prior to recording data to insure that the system reaches steady state conditions and the surface is degassed.

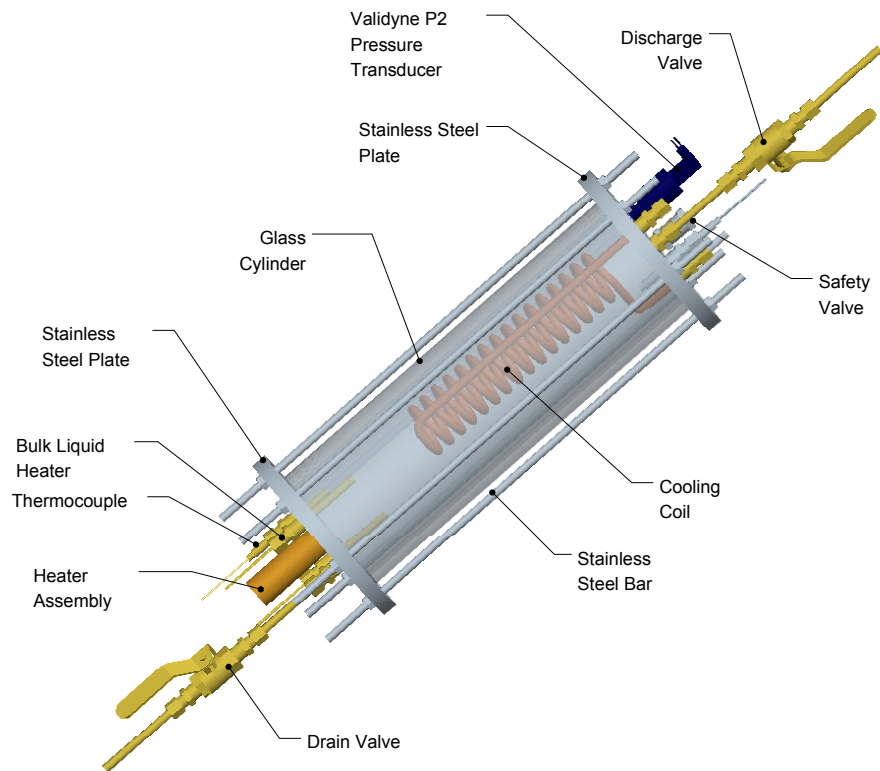


Figure 3.1. Assembled view of pool boiling chamber.

3.2 Fabrication of Heater Assembly

In this study, the boiling surface and heater consist of an integrated cylinder as shown in Fig. 3.2. Two cylinders, made of brass and stainless steel, have been manufactured. All surfaces are prepared in an identical manner. There is a thin and

small shoulder on the upper part of cylinder. A bushing is used to press the cylinder on the stainless steel plate.

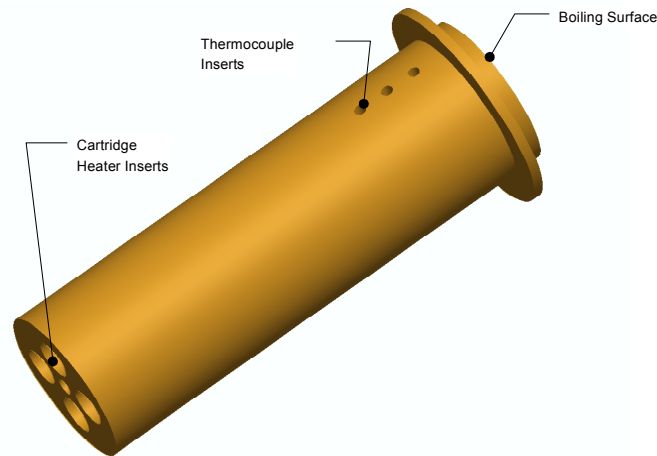


Figure 3.2. Cylindrical heater and heat transfer surface used in pool boiling experiments.

Heat is supplied to the boiling surface by four high-density cartridge heaters embedded in the cylinder. These four cartridge heaters are rated at 200W each, which yields a maximum heat flux of $1600 \text{ kW} / \text{m}^2$. Type J fine wire thermocouple probes with glass braid insulation are embedded along the length of cylinder at 10mm, 15mm, and 20mm from the boiling surface. The heated cylinder is heavily insulated. At each vertical location, two thermocouples are embedded with the tip located at a radial distance of 6.35 mm from the outer surface. High temperature air-cured Omegabond 400 is used to embed these thermocouple probes into the cylinder to measure the temperature distribution in the axial direction. The temperature readings from the thermocouples on the same horizontal plane are averaged. Thus the average temperature readings at the three vertical positions are used to evaluate the temperature gradient, boiling heat flux by

Fourier's first law and the surface temperature by extrapolation. A Teflon o-ring is as a seal to prevent leakage and as insulation to prevent the heat loss from the cylinder to the stainless steel base plate, shown in Fig. 3.3. It turns out that the gap between this o-ring and the brass cylinder is a very good promoter of ebullition. The bubble column arising from these gaps will obstruct the observation of the experimental surface. Eventually a thin layer of epoxy was carefully applied to seal the gap, which resolved the problem.

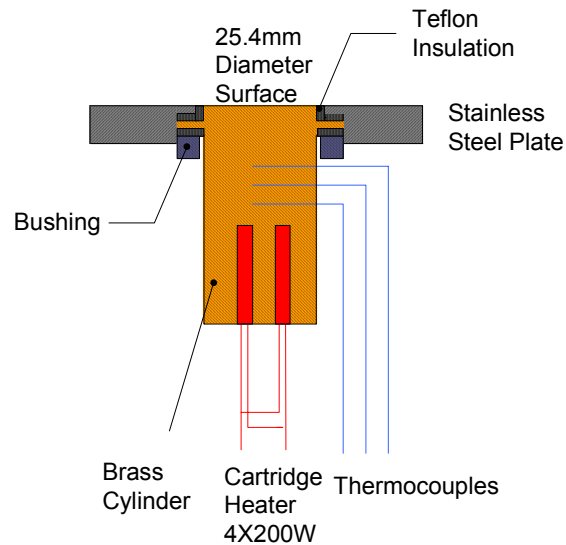


Figure 3.3. Schematic drawing of brass cylinder installation.

3.3 Surface Preparation

The rough surface preparation method is detailed in chapter 2. The mirror surface is polished initially with grit 400 aluminum oxide sandpaper followed by grit 1200 silicon carbide sandpaper and then gently polished with Brasso metal polish liquid and a felt Dremel tool bit. After these procedures, the surface attains a mirror smooth finish with an rms roughness of $0.018 \mu\text{m}$.

3.4 Instrumentation and Calibration

An Access 12-8 digital data acquisition system is used to record the pressure and temperature measurements. The pressure in the test chamber is measured with a Validyne P2 pressure transducer with an uncertainty of ± 0.2 kPa. The calibration curves are shown in Fig. 3.4. The uncertainty of temperature measurement is ± 0.5 °C. The uncertainty of the surface temperature is ± 1.5 °C. The bubble nucleation, growth and departure processes are captured using a high-speed CMOS digital camera, Hi-Dcam II from NAC Image Technology, which can run at 20,000 frames per second (fps). The camera images are stored and analyzed using the software Pixie Player that is accompanied with the camera. A 2000 fps frame rate with a resolution of 1280×256 is appropriate for this study.

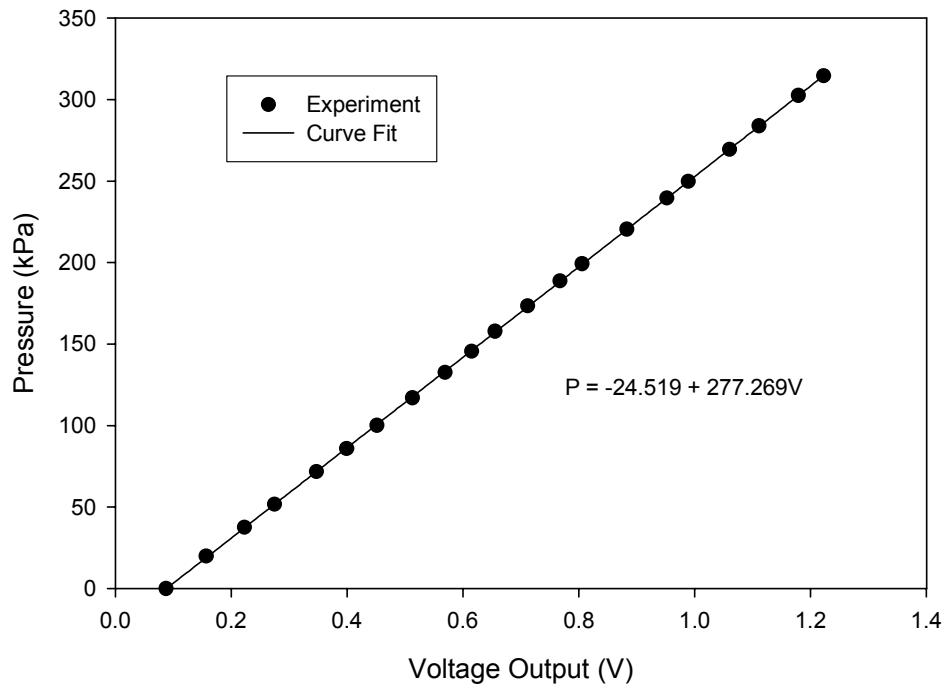


Figure 3.4. Validyne P2 pressure transducer calibration curve.

3.5 Experimental Results

3.5.1 Temperature Measurements

Figures 3.5 and 3.6 show the measured temperature distributions along the brass cylinder using water and ethanol with boiling conditions. For the brass surface, the temperature gradient between the top measurement point and the middle point is very close to the gradient between the middle point and the bottom point. So the temperature variation is linear, indicative of one-dimensional heat flow.

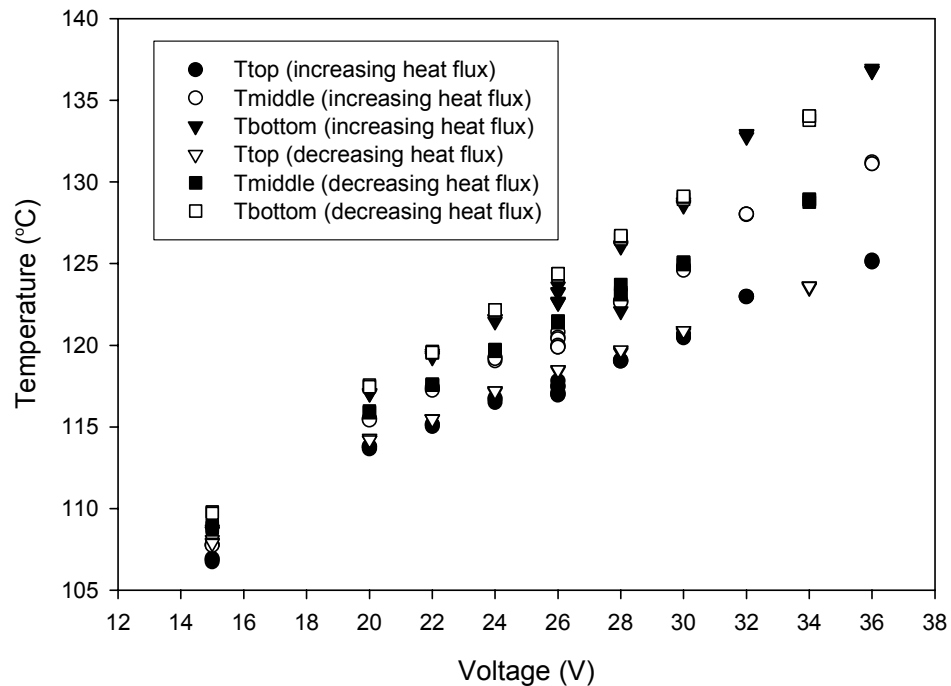


Figure 3.5. Measured temperature distribution with water on brass surface.

Figures 3.7 and 3.8 show the measured temperature distributions for the stainless steel cylinder using water and ethanol, respectively. For the stainless steel sample, the measured temperature distribution along the length of the cylinder is slightly non-linear, thus a finite volume inverse computational method is used to match the computed temperature distribution with that measured. The computed distribution is used to

evaluate the surface temperature. Due to smaller thermal conductivity, the stainless steel sample has a larger temperature gradient for the same heat flow.

Figure 3.9 shows the temperature distribution with ethanol on the mirror-finish brass surface. Here, the temperature distribution is also linear.

3.5.2 Boiling Curve

The measured temperature distribution is used to evaluate the boiling curve. Heat flux versus wall superheat curves for the brass surface using water and ethanol are plotted as Figs. 3.10 and 3.11. Two heat transfer regimes are observed, free convection and nucleate boiling. At very low superheat the free convection controls the heat transfer. At the incipient point, $\Delta T_{sat} = 9\text{ }^{\circ}\text{C}$, the nucleate boiling regime is observed. Very high heat fluxes are achieved with small increases in wall superheat. Ethanol has higher incipience point, $\Delta T_{sat} = 14\text{ }^{\circ}\text{C}$, and lower heat transfer rate than water. The ethanol on brass also exhibits boiling hysteresis, as is typical of highly wetting fluids. Zeng and Klausner (1989) also observed the hysteresis in saturated flow boiling.

Figures 3.12 and 3.13 show the heat flux as a function of wall superheat using the stainless steel heat surface with water and ethanol, respectively. Compared with the brass sample, the heat transfer rate is considerably lower.

Figure 3.14 shows the heat flux versus wall superheat for the mirror-finish brass surface using ethanol.

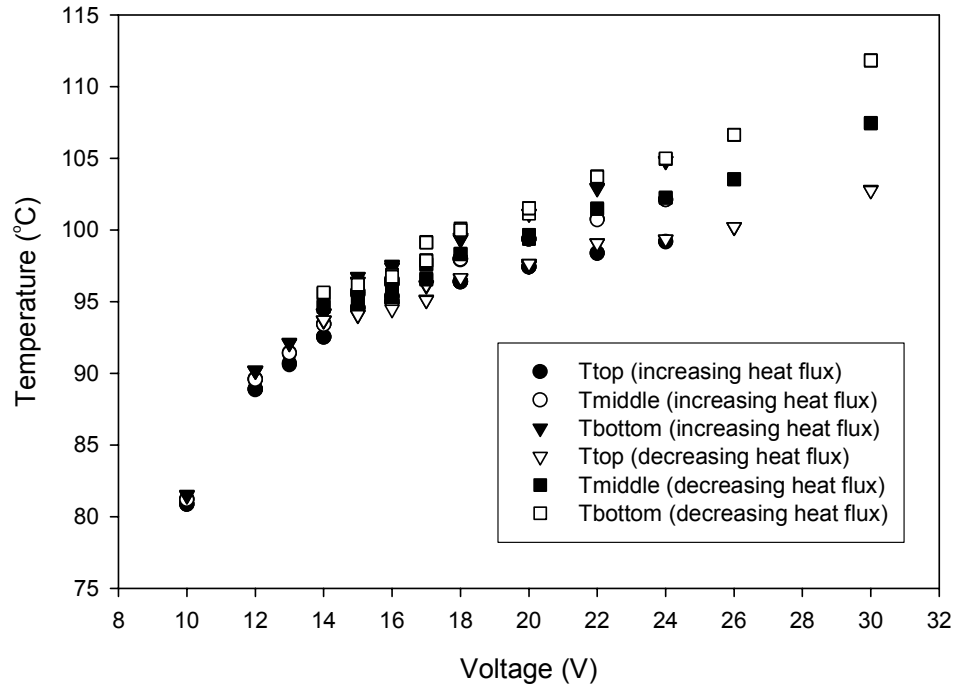


Figure 3.6. Measured temperature distribution with ethanol on brass surface.

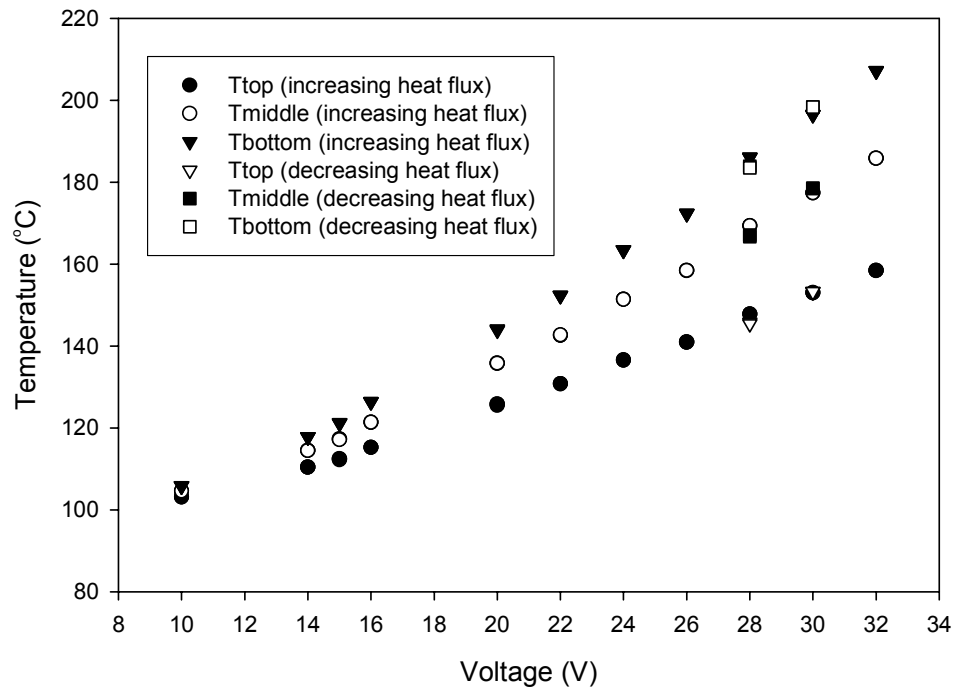


Figure 3.7. Measured temperature distribution with water on stainless steel surface.

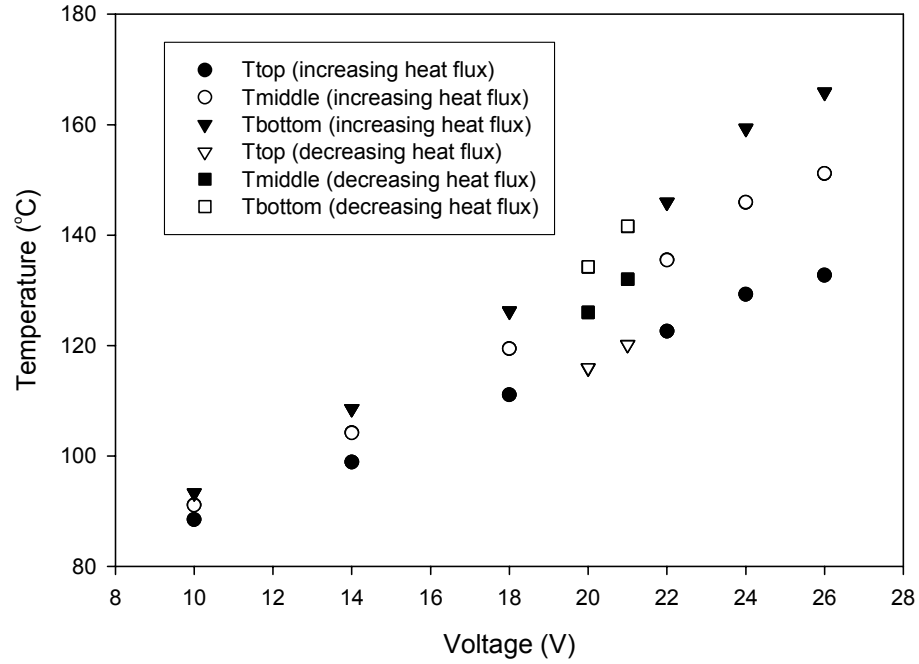


Figure 3.8. Measured temperature distribution with ethanol on stainless steel surface.

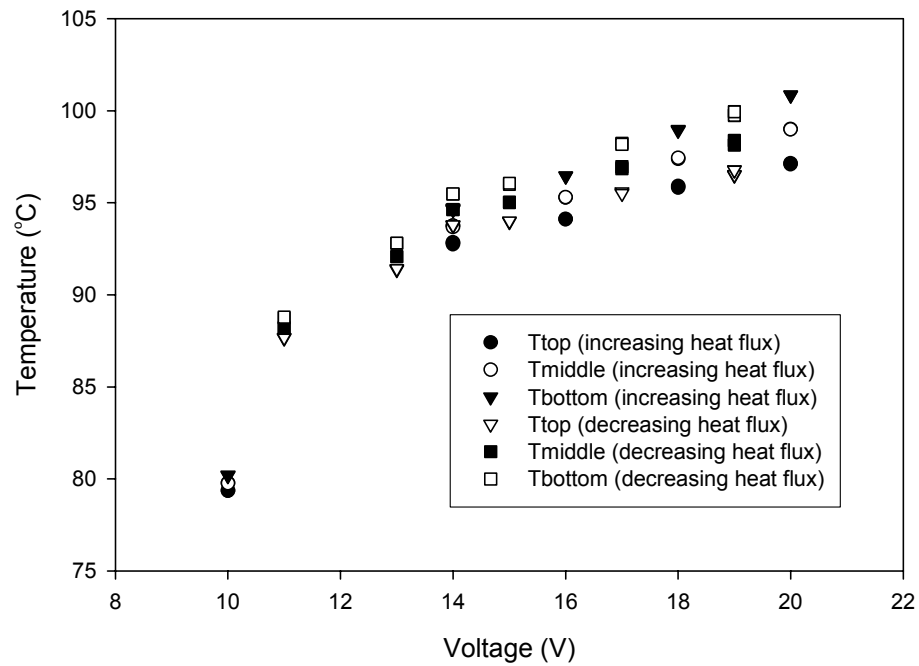


Figure 3.9. Measured temperature distribution with ethanol on the mirror-finish brass surface.

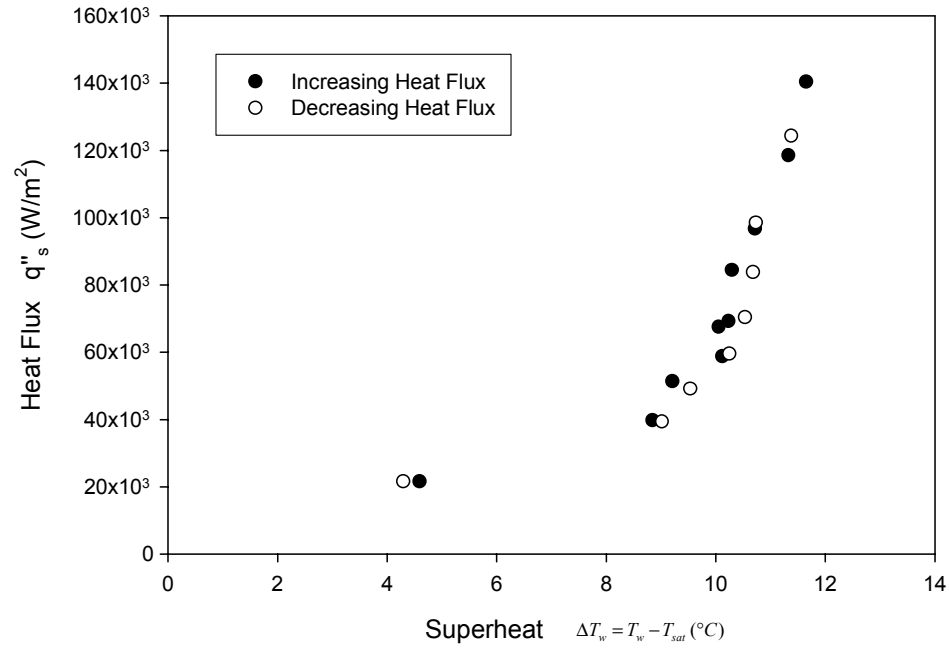


Figure 3.10. Heat flux as a function of wall superheat with water on brass surface.

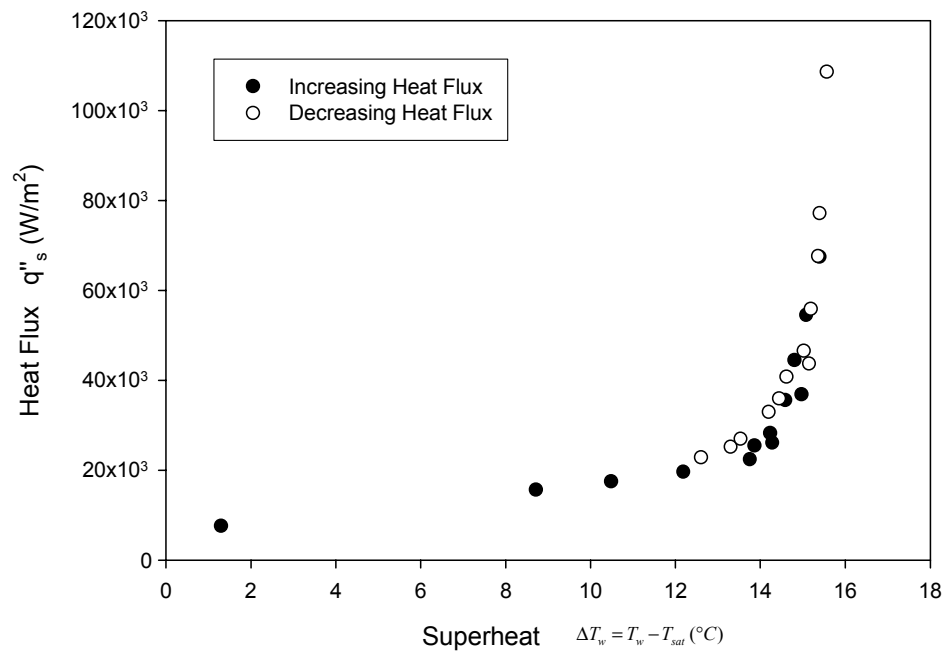


Figure 3.11. Heat flux as a function of wall superheat with ethanol on brass surface.

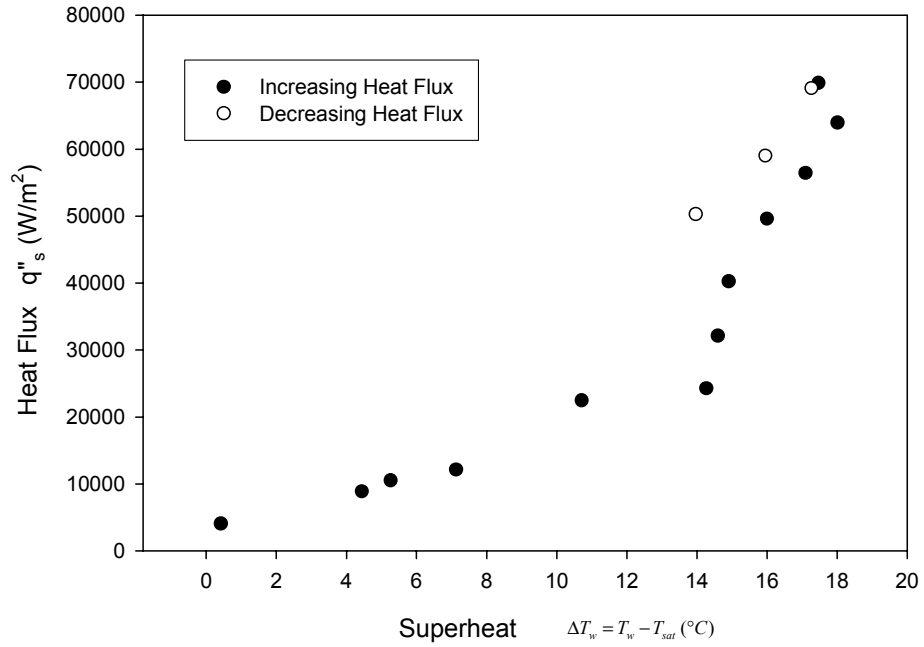


Figure 3.12. Heat flux as a function of wall superheat with water on stainless steel surface.

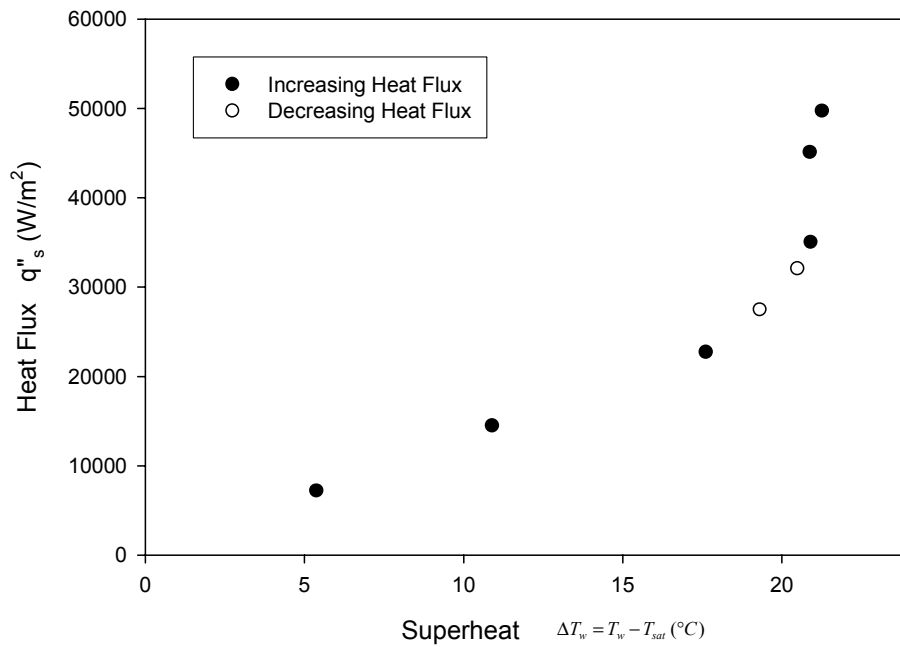


Figure 3.13. Heat flux as a function of wall superheat with ethanol on stainless steel surface.

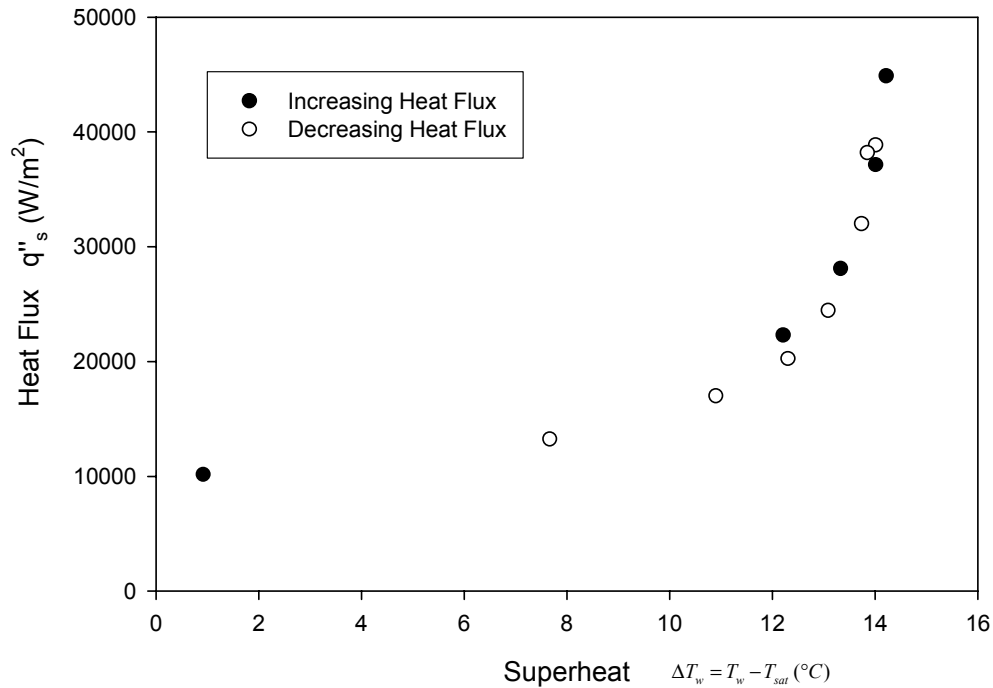


Figure 3.14. Heat flux as a function of wall superheat with ethanol on polished brass surface.

3.5.3 Experimental Observation

Nucleation site density has been measured for saturated pool boiling using distilled water and ethanol on brass and stainless steel surfaces with the same surface finishes as the samples in the gas nucleation experiments. A typical image of boiling on the heater surface captured by the high speed CMOS digital camera is shown in Figure 3.15.

From the observation, there are two types of sites at a certain heat flux condition: (1) intermittent and (2) continuous. Intermittent sites disappear for a period of time before re-appearing. The waiting time varies from several seconds to about 5 minutes. Continuous sites will continuously generate bubbles once the superheat is sufficient to activate the site.

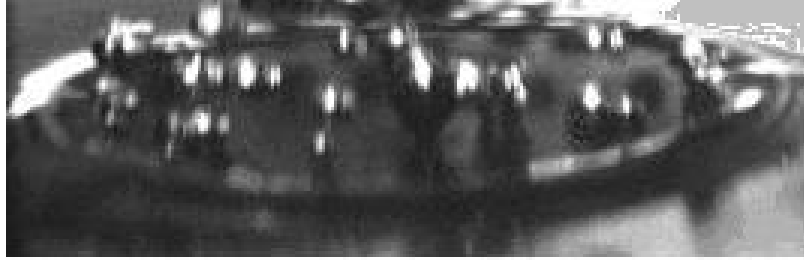


Figure 3.15. A typical image of pool boiling nucleation sites.



Figure 3.16. Deposits on the brass surface.



Figure 3.17. Deposits on the stainless steel surface.

Most of the active boiling sites, either distilled water or ethanol, deposited a small annular white stain on the heating surfaces as shown in Figs. 3.16 and 3.17. Obviously the stains on the brass surface are much larger than they are on the stainless steel surface. These stains may be used for identifying the locations of the active sites for a later study.

3.5.4 Nucleation Site Density Comparison for Pool Boiling and Gas Nucleation

A. Nucleation site density measurements with distilled water

According to classical heterogeneous nucleation theory the critical radius at the mouth of a cavity required for incipience is

$$r_c = \frac{2\sigma T_{sat}}{\rho_v h_{fg} \Delta T_{sat}}. \quad (3.1)$$

For gas nucleation it is expressed as

$$r_c = \frac{2\sigma}{\Delta P}. \quad (3.2)$$

Figure 3.18 shows the variation of nucleation site density as a function of $\frac{\Delta P}{2\sigma}$ for gas

nucleation and $\frac{1}{r_c}$ for pool boiling with water on brass. The variation of nucleation site

density in Fig. 3.18 is observed to follow the same trend for both gas nucleation and pool boiling. However, the gas nucleation data are typically higher for the same critical radius. This has also been observed by Eddington and Kenning (1978). Based on heterogeneous nucleation theory there are several possible explanations. One possible explanation is that in the vicinity of a nucleation site, energy is depleted from the heater substrate due to bubble growth and this suppresses the formation of nucleation sites in the surrounding vicinity. This is referred to as thermal interference. Another possible explanation is that a very thin thermal boundary layer results in an upper limitation on the

size of cavities that can become active, as analytically detailed by Hsu (1962). No such limitations exist for gas nucleation. As discussed by Cornwell (1982), another possibility is that cavities that might otherwise be flooded, could trap vapor during gas nucleation experiments as a result of contact angle hysteresis during pre-pressurization.

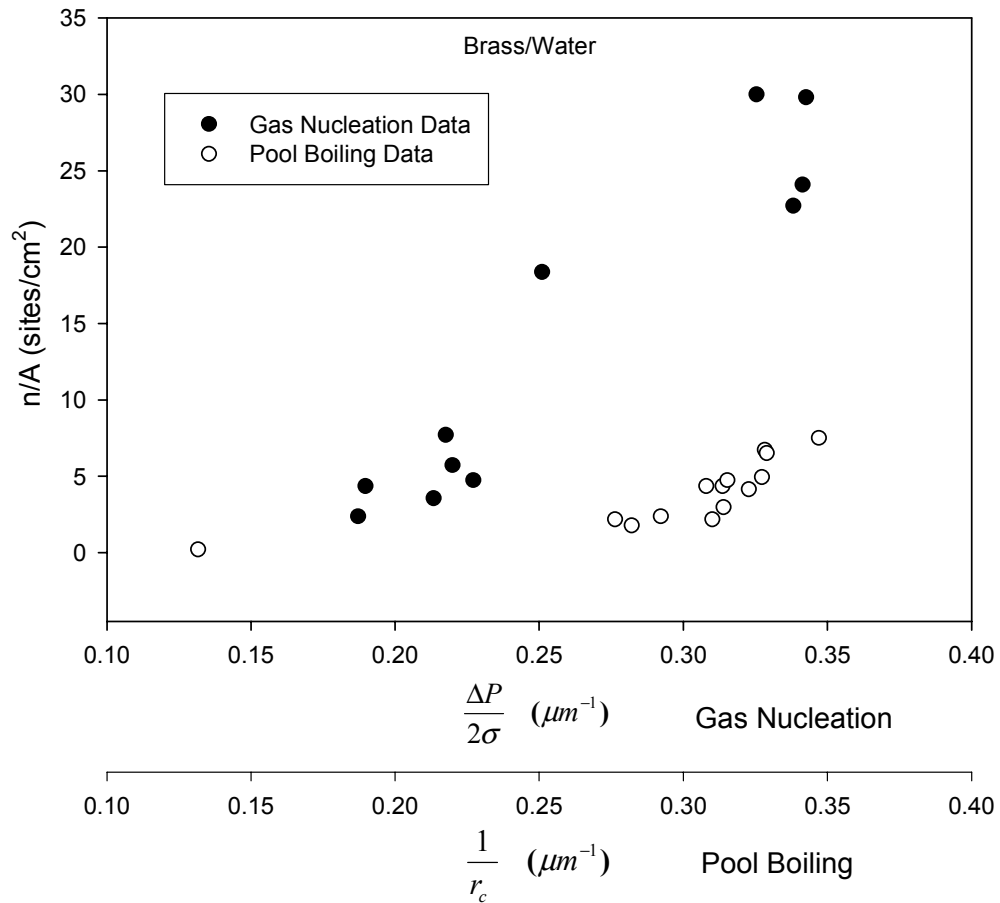


Figure 3.18. Variation of nucleation site density for water on brass surface using gas nucleation and pool boiling.

In order to further explore the differences in nucleation characteristics, both gas nucleation and pool boiling experiments were also done on the stainless steel surface. The observed variation of nucleation site density with water on stainless steel as a

function of $\frac{\Delta P}{2\sigma}$ for gas nucleation and $\frac{1}{r_c}$ for pool boiling is shown in Fig. 3.19. The nucleation site density is slightly higher for gas nucleation than for pool boiling at the same critical radius. In both cases, the nucleation site density increases with decreasing critical radius, as expected.

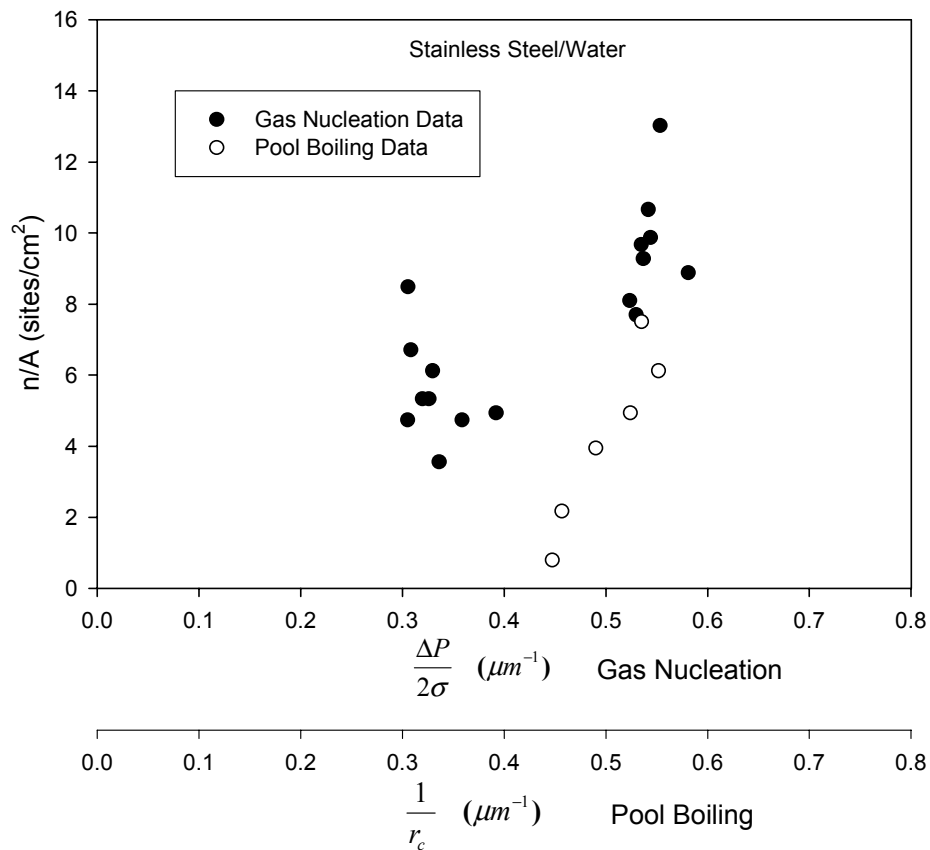


Figure 3.19. Variation of nucleation site density for water on stainless steel surface using gas nucleation and pool boiling.

B. Nucleation site density measurements with ethanol

Nucleation site density measurements have also been conducted with ethanol.

Figure 3.20 shows the variation of nucleation site density with ethanol on brass.

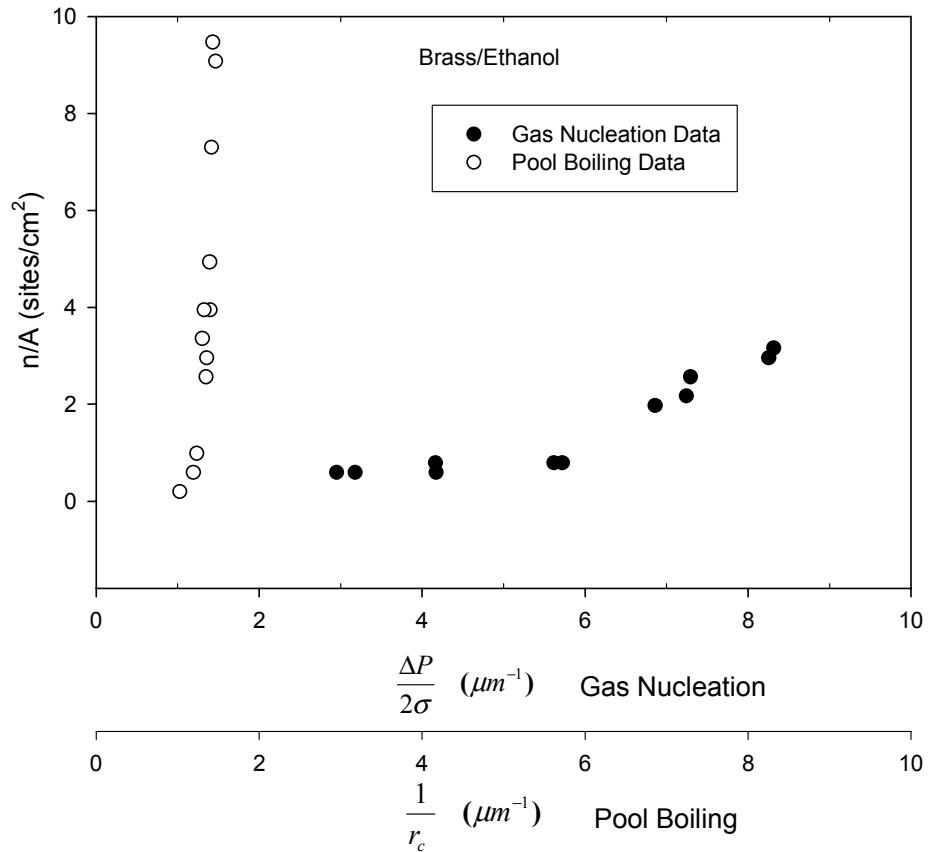


Figure 3.20. Variation of nucleation site density for ethanol on brass surface using gas nucleation and pool boiling.

Due to the high wettability of ethanol, most cavities on the surface are flooded. Only some very small cavities can trap vapor and thus a very high $\frac{\Delta P}{2\sigma}$ is required to activate sites for gas nucleation experiments. The increase in the number of sites activated with increasing pressure is very small, even with an order of magnitude increase in $\frac{\Delta P}{2\sigma}$. In contrast, nucleation sites are easily activated during pool boiling with ethanol on brass. A larger value of $\frac{1}{r_c}$ is required for incipience with ethanol on brass compared

with water on brass, as expected due to the higher wettability with ethanol. However, once the incipience point is reached, small decreases in the critical radius result in very large increases in nucleation site density. This is shown more clearly in Fig. 3.21, where the ethanol on brass pool boiling nucleation site density is shown with a refined scale for the inverse of critical radius. The reason these data are so surprising is the gas nucleation experiments reveal that most cavities are flooded and a very large value of $\frac{1}{r_c}$ should be required to activate nucleation sites during pool boiling. Instead, very moderate values of $\frac{1}{r_c}$ result in a substantial number of nucleation sites during pool boiling. It would appear that these nucleation sites are activated due to some other mechanism than classical heterogeneous cavity vapor trapping.

Ethanol gas nucleation experiments were done on the stainless steel surface with very high $\frac{\Delta P}{2\sigma}$ ($20 \mu\text{m}^{-1}$) and due to flooding, at most two nucleation sites were activated. In contrast Fig. 3.22 shows the variation of nucleation site density for pool boiling of ethanol on stainless steel with the inverse of the critical radius. A large nucleation site density is achieved at a very moderate critical radius. Slightly smaller critical radius is required for pool boiling on stainless steel than for brass to achieve a certain nucleation site density. However, once incipience is established, the pool boiling nucleation site density on stainless steel increases very rapidly with small decreases in the critical radius. This is in stark contrast to the gas nucleation experiments where it is extremely difficult to activate any nucleation sites due to cavity flooding.

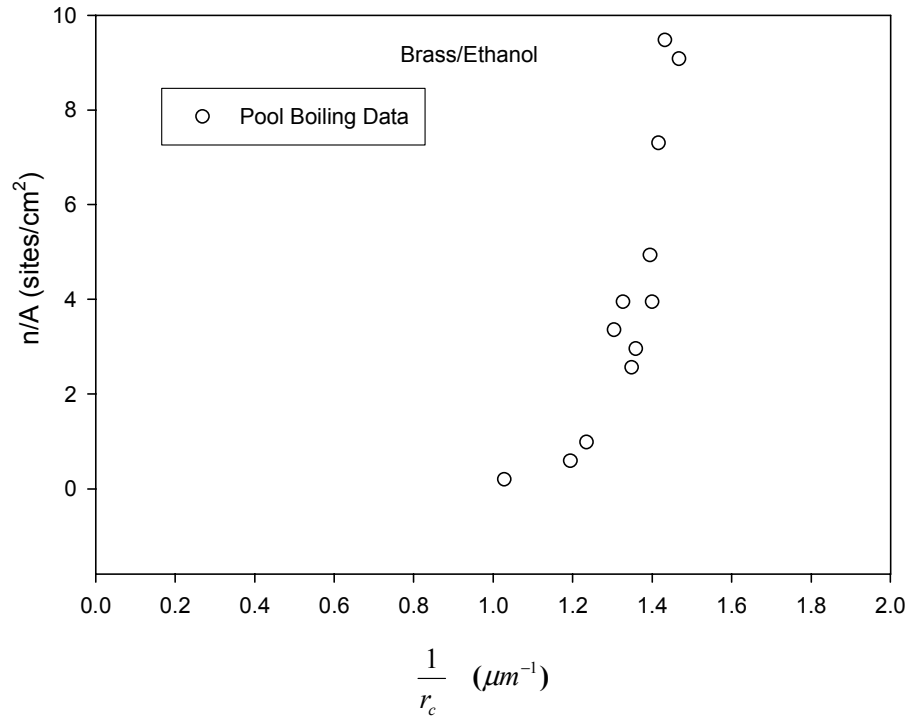


Figure 3.21. Variation of pool boiling nucleation site density for ethanol on brass surface.

If the variation of nucleation site density were controlled by some other mechanism than heterogeneous cavity vapor trapping, then on any given surface the nucleation site density should be independent of the surface roughness. In order to test an extreme case with ethanol, the brass surface was polished to a mirror-like finish. The measured rms roughness is $0.018 \mu\text{m}$ as compared with the rough brass surface that has an rms roughness of $1.02 \mu\text{m}$. The nucleation site density measured for the rough and polished brass surface are compared in Fig. 3.23. It is seen that slightly more superheat (1.7°C) is required to achieve incipience with the polished surface. However, once incipience is established, there is essentially no difference in the variation of nucleation sites on the coarse and polished surfaces. These results provide substantial additional evidence that

another mechanism other than heterogeneous cavity vapor trapping is involved in seeding pool boiling nucleation sites.

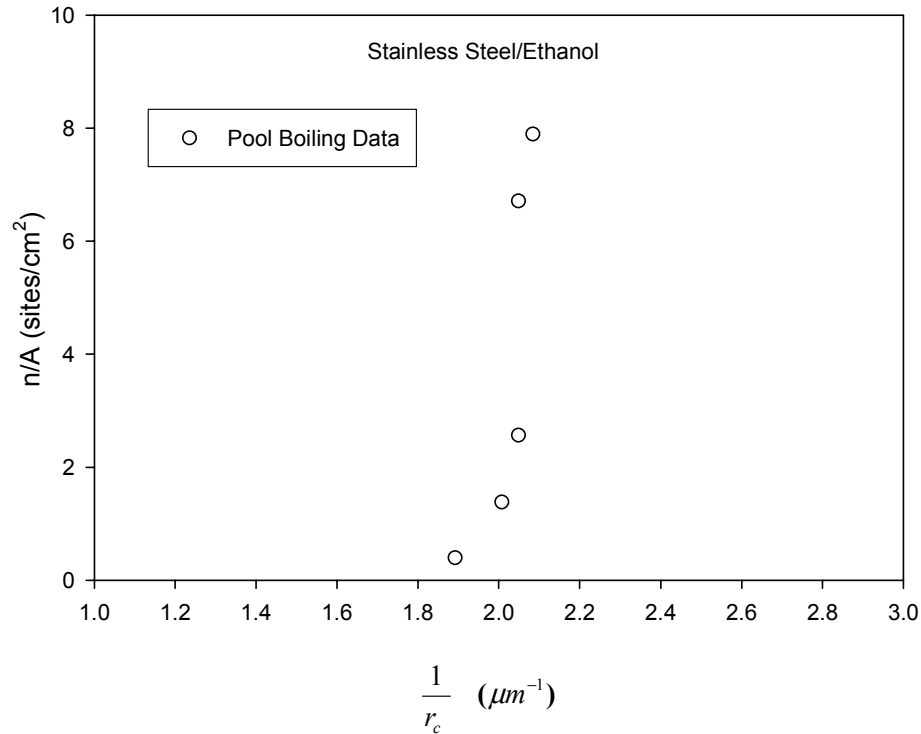


Figure 3.22. Variation of pool boiling nucleation site density for ethanol on stainless steel surface.

3.5.5 Discussion

There was some speculation that some dissolved gas might precipitate out of the ethanol to form micro-bubbles, and these may be responsible to seed the nucleation. To further explore the effect of dissolved gas in ethanol a rigorous degassing procedure was done. The degassing procedure consisted of attaching a vacuum pump to the boiling chamber and pumping down the chamber with and without boiling through several cycles. No chemical analysis was done on the ethanol, so the degree of degassing that was achieved is uncertain. Subsequent to the degassing procedure it was found that the incipient points of ethanol on brass and stainless steel are very similar to those reported in

Figs. 3.21 and 3.22. Furthermore, no micro-bubbles were visually observed in the liquid prior to incipience. So, micro-bubbles have been ruled out as the mechanism driving the present observations.

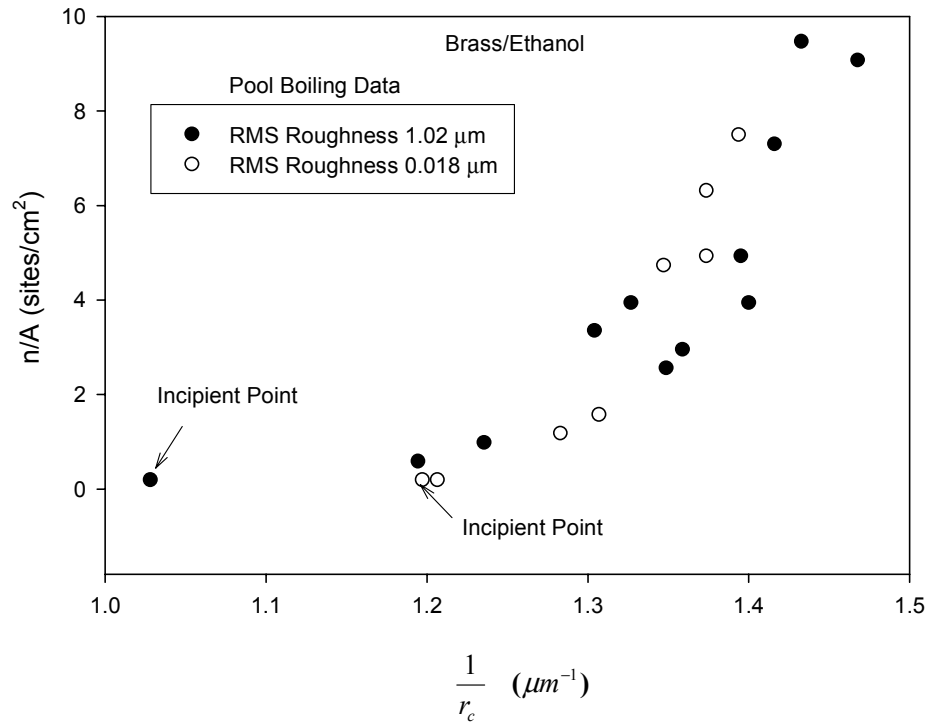


Figure 3.23. Variation of pool boiling nucleation site density for ethanol on coarse and polished brass surfaces.

Recently, Theofanous et al. (2002) reported nucleation site density measurements with pool boiling of water on a Ti film surface with a mean roughness of 4 nm. The surface was manufactured by electron beam metal vapor deposition on a glass substrate. It was found that the incipient superheat is approximately 10° C. According to cavity vapor trapping nucleation theory, the nano-scale surface features cannot activate nucleation sites at such low superheat. They speculated that cavity vapor trapping cannot be responsible for nucleation site formation.

Since the pioneering work of Corty and Foust (1955) and Griffith and Wallis (1960) heterogeneous nucleation theory based on cavity vapor trapping has been almost exclusively relied upon to predict incipience and nucleating characteristics of boiling systems. Based on the wealth of experimental observations reported in the literature and the incontrovertible microscopic measurements by Cornwell (1977), there is no valid reason to doubt that vapor trapping cavities are responsible for seeding nucleation sites in boiling systems. However, there is ample evidence from this work and Theofanous (2002) that vapor trapping cavities are not exclusively responsible for seeding nucleation sites. Certainly there is no other **obvious** mechanism that is responsible for seeding nucleation sites when vapor trapping cavities are not available. Nevertheless, after an exhaustive search, a plausible mechanism has been identified that can explain the formation of boiling nucleation sites when vapor trapping cavities are not available. This mechanism is discussed next.

Most recently Tyrrell and Attard (2001) obtained an atomic force microscope (AFM) image of very closely packed nanobubbles that cover a smooth hydrophobic surface (glass with 0.5 nm rms roughness) submerged in water. From theoretical considerations, stable spherical nanobubbles cannot exist because the high internal pressure would preclude equilibrium with the surroundings. However, the image reveals that the bubbles are pancake shaped with a large base and small height. The average height is reported to be 20-30 nm with a base diameter on the order of 200 nm. Modeling a nanobubble as the cap of a sphere, the radius of curvature of the cap is on the order of 0.3 μm . Although the dimensions of the AFM image are not quantitatively precise, since the AFM tip influences the shape of the deformable bubble, the uncertainty in the

dimensions are on the order of several nanometers. A radius of curvature on the order of $1\ \mu\text{m}$ is required to activate nucleation sites with low superheat. It is not unreasonable to expect that due to statistical variations in shape and size, pancake shaped nanobubbles exist with the appropriate critical radius of curvature for nucleation, especially since close packed nanobubbles can merge. Although the detailed surface physics controlling the nanobubbles are not well understood, it is clear that there is a strong attractive force holding these pancake shaped bubbles on the solid surface. It has been observed that the nanobubbles easily cover the whole surface within 10-20 minutes after scraping the surface. Ishida et al. (2000) also used AFM to image nanobubbles on hydrophobic surfaces. However, with water on a hydrophilic surface, nanobubbles were not observed. So, whether or not nanobubbles can cover an ethanol submerged surface is uncertain, especially since the mechanism for inducing and sustaining nanobubbles is not known. Nevertheless, the identification of nanobubbles as potential nucleation sites in boiling systems certainly requires further scrutiny.

The experimental observations of nanobubbles on a hydrophobic surface by Tyrrell and Attard (2001) and Ishida et al. (2000) remain controversial. However, indirect evidence of their existence has been provided by Tretheway and Meinhart (2002) who measured a slip length on the order of 0.92 microns between a fluid and a hydrophobic surface. Tretheway and Meinhart (2004) attribute the velocity slip to the presence of nanobubbles on the surface. They also report that increasing system pressure can inhibit the formation of nanobubbles and reduce the velocity slip. It is interesting that Mizukami et al. (1998) report experiments with pool boiling of ethanol on a 0.3 mm diameter platinum wire in which incipience occurs with low superheat and no pre-pressurization of

the boiling chamber. With moderate and high pre-pressurization, very high superheat is required for incipience. If nanobubbles do exist, the suppression of nanobubbles with pre-pressurization is a possible explanation for their results.

The ethanol dehydrogenation process may also be responsible to seed the nucleation. One main usage of industrial ethanol is for the production of ethanal (i.e. acetaldehyde). By passing the vapor phase ethanol over the copper catalyst at 280-340 °C, the conversion rate can reach 75% per pass. Two atoms of hydrogen are eliminated from each ethanol molecule to form hydrogen gas in this process termed dehydrogenation. The chemical reaction can be expressed as



Assume this reaction only consists of ideal gas, the variation of conversion rate with the temperature is shown in Fig. 3.24. As shown in this graph, the conversion rate is 1.43% at 373.15 K. This amount of hydrogen is enough to initiate the nucleate boiling.

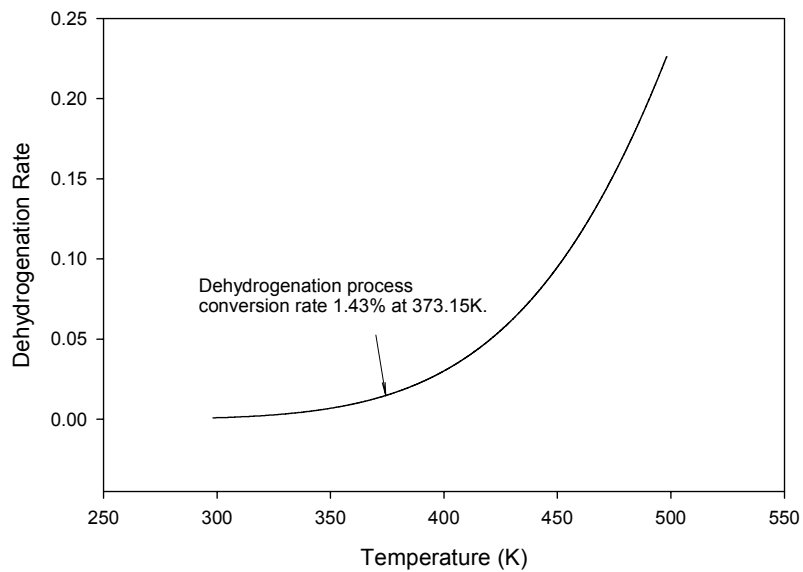


Figure 3.24. Dehydrogenation conversion rate with the temperature.

CHAPTER 4 STATISTICAL MODEL FOR HETEROGENEOUS NUCLEATION

4.1 History and Review

The heat transfer community has long sought after a mechanistic model to predict the phenomena of vapor bubble formation on heating surfaces. It has been well established that bubbles originate from cavities on the heating surface. This implies that detailed and precise information on the topography of the heating surface is a required foundation for a predictive model. In this chapter, a vertical scanning interferometer has been used to gather surface topography information. The statistical data on cavity mouth diameters and cavity half-cone angles for the brass and stainless steel surfaces have been used to predict the nucleation site density. The model used in this chapter is constructed based on the current understanding of heterogeneous nucleation theory, accounting for the effects of wettability and surface conditions.

4.1.1 Gas Trapping Criteria

The current explanation of heterogeneous nucleation theory suggests vapor bubbles are initiated from trapped gas/vapor in surface cavities. There are currently two theories to describe the mechanism of gas/vapor entrapment. One theory is based on the criterion for thermodynamic stability. Wang and Dhir (1993) developed a gas entrapment criterion for spherical, conical and sinusoidal cavities based on supposition that gas filled cavity achieves minimum Helmholtz free energy at the liquid-gas interface. It is suggested that gas or vapor will be entrapped if the contact angle and cavity side angle satisfy the following condition:

$$\theta > \psi_{\min}, \quad (4.1)$$

where θ is the contact angle and ψ_{\min} is the minimum cavity side angle of a spherical, conical, or sinusoidal cavity. For the conical cavity, the location of ψ_{\min} is at the mouth of the cavity, as shown in Fig. 4.1. For a conical cavity, cavity side angle ψ_{\min} is usually larger than 90 degree. It implies that the conical cavity cannot trap gas or vapor when the liquid/solid contact angle is smaller than 90 degrees. This supposition is directly contrary to Shoji and Zhang's findings (2003). Shoji and Takagi (2001) manufactured two artificial conical cavities on a thin cooper plate. Ebullition was easily achieved from the artificial cavities where ψ_{\min} are 2.27 and 2.36 radians, respectively. The measured liquid/solid contact angle for water on brass in this study is $\theta = 1.27$ radians. This large discrepancy between the experimental observation and the theoretical derivation casts doubt on the validity of the gas trapping criterion based on the Helmholtz free energy analysis.

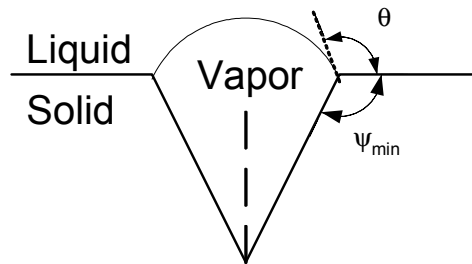


Figure 4.1. Condition for the gas entrapment (Wang).

Bankoff (1958) proposed a mechanistic model for identifying gas trapping cavities with known mouth diameter and cone angle. The model may be represented graphically as shown in Fig. 4.2. Considering the displacement of liquid across a V-shape cavity, it will only trap vapor and avoid flooding when $\theta > 2\beta$. Here β is the half-cone angle.

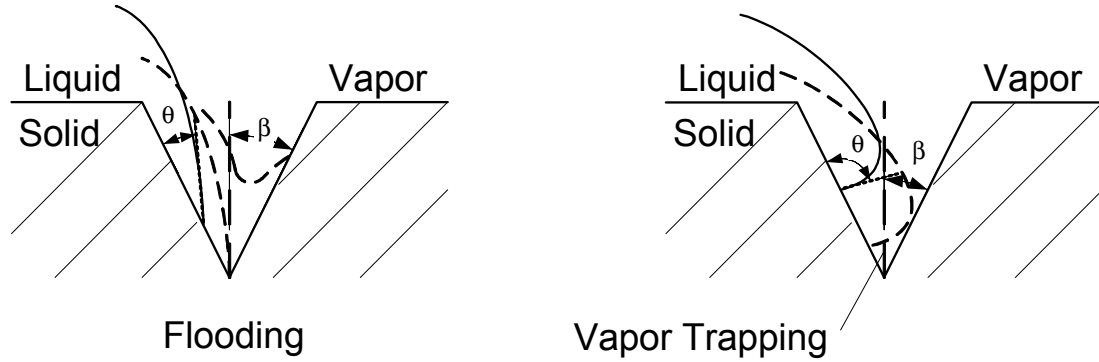


Figure 4.2. Condition for gas entrapment (Bankoff).

It is noted that systems of long grooves (appear as scratches) are common on most rough surface finishes, such as occur with machining and polishing. The artificial cavities in Shoji and Takagi (2001) study have half-cone angles 0.7 and 0.78 radians, respectively. Following Bankoff's criterion, the cavity with $\beta = 0.7$ radians will serve as a nucleation site if the contact angle is larger than 1.4 radians. For the cavity with half-cone angle $\beta = 0.78$ radians the contact angle need to be larger than 1.56 radians. The two values are close to the measured liquid/solid contact angle for water on brass. Based on these considerations, Bankoff's vapor trapping model is more reasonable and used in this study.

4.1.2 Bubble Inception

According to Young-Laplace equation, stable equilibrium conditions for a small spherical bubble formed within a superheated liquid requires that

$$P_v - P_l = \frac{2\sigma}{r}. \quad (4.2)$$

Making use of the assumption that $P_v = P_{sat}(T_l)$, where $P_{sat}(T_l)$ is the saturated pressure corresponding to the superheated bulk liquid temperature, and combining the Clausius-

Clapeyron equation with the assumption that vapor specific volume is far greater than liquid specific volume and Eq. (4.2), the minimum radius (critical radius) for a cavity to be active under certain superheat is derived as Eq. (3.1).

Griffith and Wallis (1960) used this critical radius to quantitatively relate the heating surface microstructure to nucleation phenomena. At certain wall superheat, the cavity mouth radius must be larger than the critical radius to have bubble incipience. Hsu (1962) suggested that both minimum and maximum critical cavity radii exist to allow the bubble incipience. Nucleation is only possible in those cavities for which the radius of cavity mouth is between $r_{c,\min}$ and $r_{c,\max}$. The relation for $r_{c,\min}$ and $r_{c,\max}$ were expressed by Hsu (1962) as

$$r_{c,\min} = \frac{4\sigma T_{sat} C_2}{h_{fg} \rho_v (\Delta T_{sat})_{inc} C_1} \left[1 - \sqrt{1 - \frac{(\Delta T_{sat})_{inc}}{\Delta T_{sat}}} \right] \quad (4.3)$$

and

$$r_{c,\max} = \frac{4\sigma T_{sat} C_2}{h_{fg} \rho_v (\Delta T_{sat})_{inc} C_1} \left[1 + \sqrt{1 - \frac{(\Delta T_{sat})_{inc}}{\Delta T_{sat}}} \right], \quad (4.4)$$

where two constants C_1 , C_2 are calculated from the angle, ϕ , between the side of the vapor embryo at the triple contact point and the horizontal. These are expressed as

$$C_1 = \frac{1 + \cos \phi}{\sin \phi} \text{ and } C_2 = 1 + \cos \phi \text{ respectively.}$$

4.1.3 Surface Characterization

The following researchers have conducted the surface characterization using variety of techniques. Luke (1997) performed propane boiling on a horizontal tube with three different surface roughness finishes prepared by emery grinding, rough and fine sandblasting. The surface roughness and topography were measured by a contact stylus

instrument. The author concluded that a single roughness parameter cannot account for the effect of surface structure on boiling heat transfer. Luke and Gorenflo (1999, 2000) showed that different heating surfaces with the same mean roughness can have very different heat transfer characteristics, depending on the surface preparation. Benjamin and Balakrishnan (1997) demonstrated that nucleation site density does not increase monotonically with the average roughness and developed an empirical expression for nucleation site density that depends on the surface material-fluid combination. Luke et al. (2000) used an ultrasonic stylus system to record detailed information on the surface microstructure. In order to identify potential vapor trapping cavities from the three-dimensional surface microstructure, a rolling ball technique was proposed.

4.1.4 Statistical Model

Many naturally occurring events can be described by the statistical method. Gaertner (1963) concluded that the local nucleation site population could fit the Poisson equation. Yang and Kim (1988) were the first researchers who suggested that the nucleation site density for a given surface may be quantitatively computed from knowing the size distribution of cavities $f(d)$, the distribution of the cavity half-cone angles $g(\beta)$, the minimum cavity mouth radius required for nucleation r_c , and the liquid/solid contact angle θ . A scanning electron microscope (SEM) and a differential interference contrast microscope (DIC) were used to analyze the surface microstructure to get the size distribution and half-cone angle distribution. It was found that the cavity size distribution could be fitted as

$$f(d) = 0.9797e^{-0.4898d / 2}, \quad (4.5)$$

and the half-cone angle distribution was expressed as

$$g(\beta) = 1.4006 \exp \left[\frac{-(\beta - 0.3744)^2}{0.5698} \right], \quad (4.6)$$

where d is the diameter of cavity and β is the half-cone angle. Yang and Kim proposed that nucleation site density could be predicted from

$$\frac{n}{A} = \frac{N}{A} \int_{d_{\min}}^{d_{\max}} f(d) dd \int_0^{\theta/2} g(\beta) d\beta, \quad (4.7)$$

where d_{\min} and d_{\max} are the minimum and maximum critical cavity diameters to allow the bubble incipience. They compared three nucleation site density data points for pool boiling of water on a mirror-finished stainless steel heating surface with those computed, and the data appear to agree well. Yet, the maximum superheat tested was only 2.6 °C. Wang and Dhir (1993) also proposed a statistical method for predicting nucleation site density based on surface microstructure. A copper surface was well polished and surface cavities were viewed with an optical microscope. The cavity mouth size distribution and surface wettability were considered for spherical cavities. Many data were considered with varying wettability conditions, and the nucleation site density data agreed with the predicted data to within $\pm 60\%$.

These prior successes in predicting the nucleation site density with a statistical model are the motivation for applying this method to commercial surfaces.

4.2 Surface Characterization

4.2.1 Instrumentation

Tracing back to the 1930s, a stylus techniques was developed to record the vertical deflection when scribed over a surface. The parameters including Ra (average roughness) and Rq (root mean square average roughness) were devised to quantify the two-dimensional measurement information. While Ra and Rq remain useful to provide

general guidance on surface characteristics, they do not provide sufficiently detailed information to characterize boiling nucleation. Surfaces with sharp spikes, deep pits or general isotropy may have the same average roughness value. A measurement system that can provide three-dimensional surface information will help to provide great insight into the cavity identification process. Here, a Wyko NT1000 optical profiler manufactured by Veeco Metrology Group is used in order to characterize the surface structure for the present experiments. The Wyko NT1000 uses non-contact interferometry and highly accurate, fast three dimensional surface height measurements can be obtained with a resolution of 0.1nm. Wyko Vision 32 analytical software accompanied with this machine automatically calculates the surface measurement statistics, such as Ra and Rq. The system includes a manual x/y stage, coarse/fine focus and tip/tilt adjustments, with multiple objectives and field-of-view lenses. The surface area covered by a single scan depends on the lens objective utilized. For the analysis of the brass surface an area of 595 x 453 μm is typically covered. The VSI will scan the surface and store the three dimensional location of every point on the surface with a resolution of approximately 0.1 nm. The rms roughness of the stainless steel surface is 0.88 μm , while that of the brass is 1.02 μm . The brass surface is rougher than the stainless steel, but this difference alone cannot account for the substantial difference in n/A observed between the two surfaces, which is detailed in Chapter 3. With the three dimensional topography data, it is desired to identify gas trapping cavities on the surface. After much deliberation it was concluded that a unique algorithm for identifying gas trapping cavities from the three dimensional data is not feasible due to the highly irregular topography. As an alternative, it was decided to analyze two-dimensional cross-

sections of the surface. For the current work, the brass and stainless steel surfaces have been fully analyzed.

4.2.2 Identifying Gas Trapping Cavities

A typical x-z profile of the surface is shown in Fig. 4.3, where z is in the direction of the surface depth. This scan shows the relative change in surface height along the x-direction. The length of the scan in the x-direction is 301 μm . Typically 22 x-z profiles separated by a distance of 20 μm are considered for each spot on the brass surface analyzed. The analysis of the brass surface considers data collected from 3 randomly selected spots for a total of 66 x-z profiles. It is assumed that the statistical distribution of cavities on the surface is homogeneous since a uniform surface polishing technique was used along the entire surface.

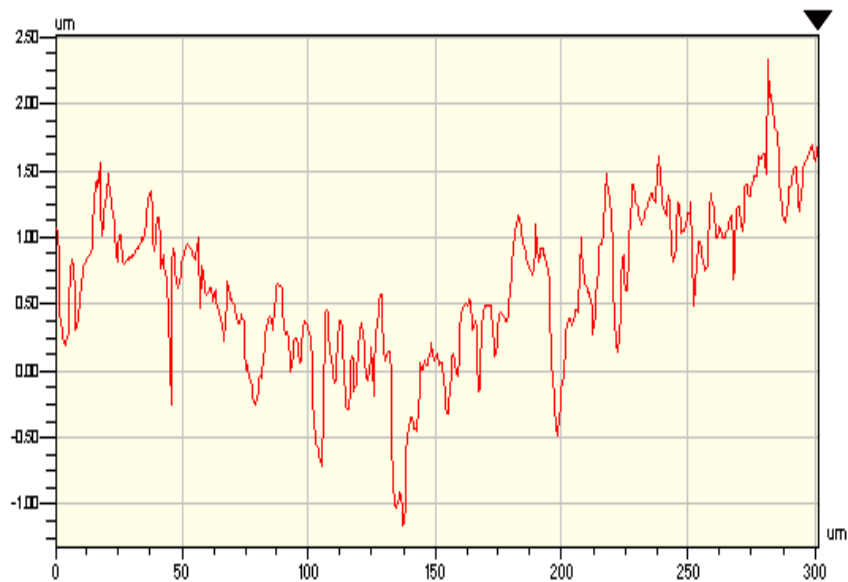


Figure 4.3. A typical x-z surface profile using VSI.

In order to identify gas trapping cavities the following procedure is implemented. Every peak in the x - z profile is identified. There exists a cavity on either side of the peak. In order to find the characteristic diameter associated with the cavity, a horizontal line is extended from the peak until it intersects the sidewall of a higher peak. The length of the extended horizontal line is taken to be the characteristic cavity diameter. It is important to note that the VSI is not capable of identifying re-entrant type cavities.

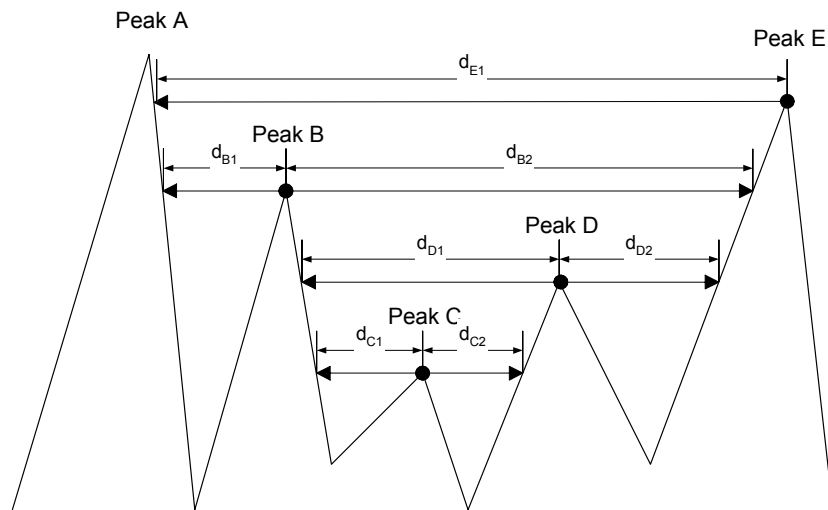


Figure 4.4. Cavity identification diagram.

An illustration is given in the Fig. 4.4. There are five peaks in this example, where peak A is the local maximum and peak C is the local minimum. A line is extended to the left from the rightmost peak, peak E. This line will stop at the declining slope of peak A since peak E is lower than peak A and higher than all others. So a cavity diameter d_{E1} is identified. Then move to the peaks located at the left side of peak E and other cavity diameters can be obtained, such as d_{D1} , d_{C1} , and d_{B1} . Up to this step, every diameter of cavities that are located at the left side of every peak is found. The second sweep includes moving from the leftmost peak, peak A, and extending the line to the right.

Using the same procedure as the first step, all mouth diameters of the cavities located at the right hand side of the peaks were found, such as d_{B2} , d_{C2} , and d_{D2} in this example. All cavity diameters can be identified by these two sweeps.

However, an uncertainty arises when cavities are located within cavities as shown in Fig. 4.5a. Two cavities A and B are located inside of a possible larger cavity C. The two possibilities are that A and B serve as separate gas trapping cavities with respective diameters of d_A and d_B or cavities A and B are merged to behave as a single gas trapping cavity C with diameter d_C . The following arguments are used to resolve this uncertainty. As the nucleating surface is flooded, the single merged cavity C will trap gas, provided cavities A and B are recessed far enough into C and C has a sufficiently small half-cone angle, β , so that it does not flood. A gas/liquid interface will form over C as shown in Fig. 4.5b. Due to pressure fluctuations in the bulk liquid that exist during the nucleating process the liquid vapor interface may be deformed as shown in Fig. 4.5c. As the pressure wave passes, the gas/liquid interface will recover to a static position as shown in Fig. 4.5b and cavity C will be preserved as a gas trapping cavity. If cavities A and B are not sufficiently recessed in C, a pressure fluctuation can cause the gas/liquid interface to deform as shown in Fig 4.5d. After the pressure wave passes, the gas liquid interface will recover to a static position as shown in Fig. 4.5e, in which gas cavities A and B will serve as the vapor trapping cavities.

In order to determine which outcome is more probable a cavity with a static gas/liquid interface is shown in Fig. 4.6 with a uniform radius of curvature, r . The cavity is dimensioned as follows: diameter, d ; half-cone angle, β ; and liquid solid contact angle,

θ . From geometrical considerations, the height of the gas/liquid interface above the cavity, h , is given by

$$h = \frac{d}{2} \tan \left[\frac{\pi/2 - \theta + \beta}{2} \right]. \quad (4.8)$$

Given that H is the distance between peaks that form cavity C and cavities A and B as shown in Fig. 4.5a, it is postulated that a single merged cavity C is most probable, when $h < H$, otherwise recessed cavities A and B are most probable as shown in Fig. 4.5e.

Using this criterion to identify the most probable potential gas trapping cavities, a computer code was developed to automate the process of identifying cavity mouth diameters and half-cone angles from the x-z surface profiles obtained using the VSI. 66 profiles are examined for the brass surface and a total of 6,025 cavities were identified with an associated cavity mouth radius and half-cone angle. For the stainless steel surface 77 profiles are examined and a total of 6704 cavities were identified. After examining the data, it is readily apparent that most of the cavities are shallow and will be flooded according to Bankoff's gas trapping criterion: cavities will trap gas or vapor when $\theta > 2\beta$. In fact, finding a cavity that does satisfy Bankoff's gas trapping criterion is a very low probability event.

The prediction of the nucleation site density requires information on the statistical distribution of cavity mouth diameters and cavity half-cone angles. In order to better resolve the distribution with cavities that are more likely to trap gas, a filtering procedure was applied. The ratio of the cavity depth to mouth diameter was identified for each cavity, and the mean and standard deviation were determined. Only those cavities in which the ratio of the cavity depth to mouth diameter is greater than the mean plus one standard deviation are used to construct cavity diameter and half-cone angle distributions.

After filtering, only 1412 cavities remain out of the original 6,025 cavities originally identified on the brass surface and 1039 cavities remain for the stainless steel surface.

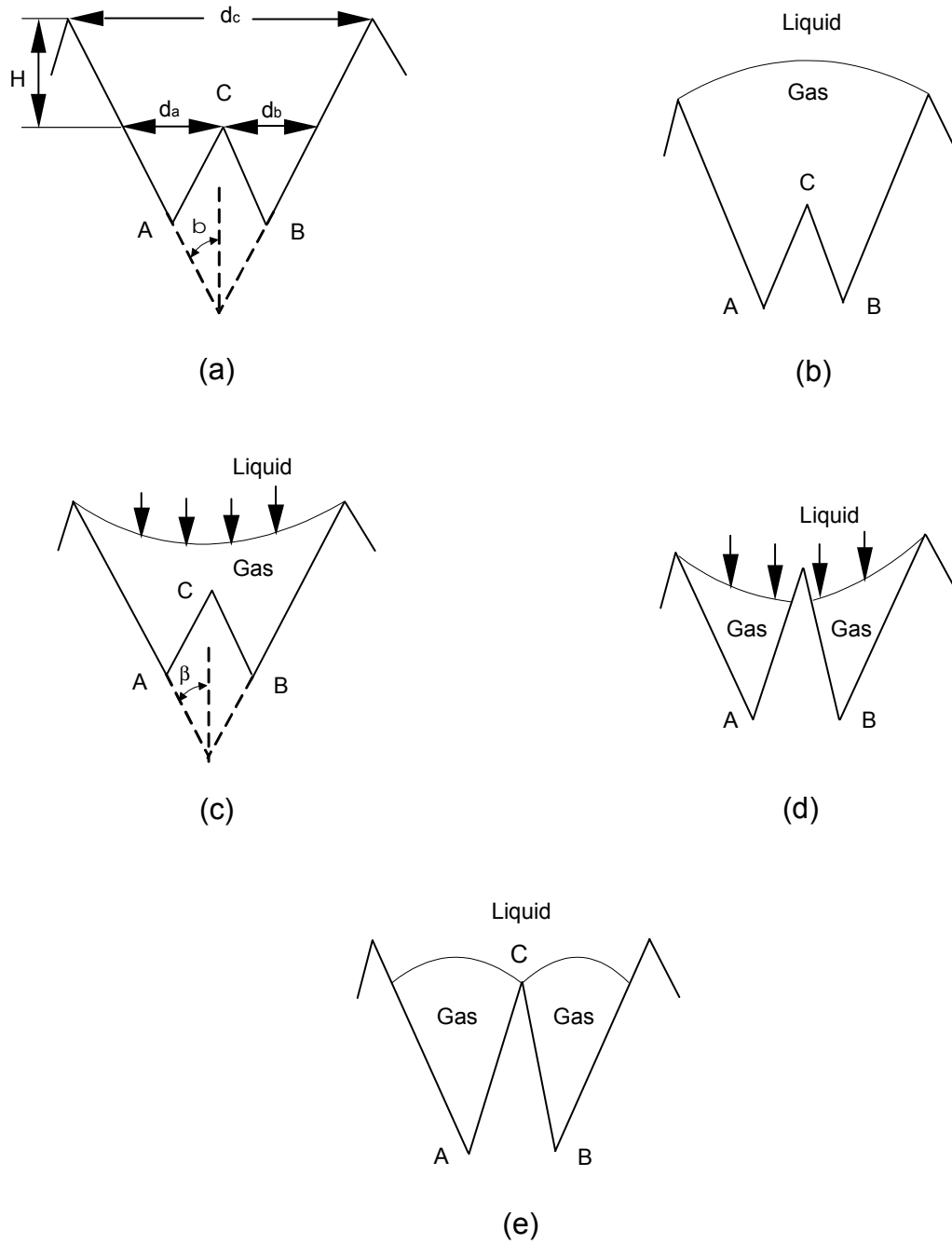


Figure 4.5. Different gas/liquid interface configurations for cavities residing inside a cavity.

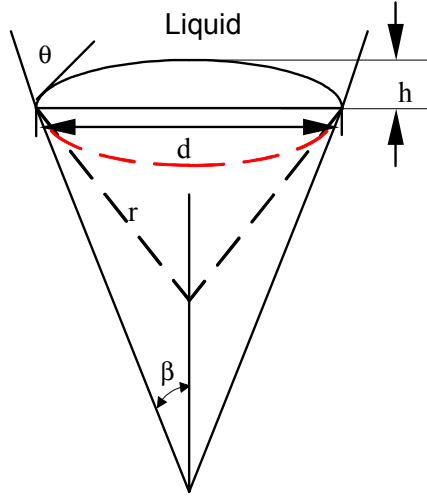


Figure 4.6. Cavity dimension with gas/liquid interface at cavity mouth.

4.2.3 Distribution of Cavity Diameters

4.2.3.1 Introduction of Weibull distribution

A continuous random variable X has a Weibull distribution if its probability density function (pdf) has the form

$$f(x; w, \lambda) = \frac{\lambda}{w} \left(\frac{x}{w}\right)^{\lambda-1} \exp\left[-\left(\frac{x}{w}\right)^\lambda\right]; \quad x \geq 0; \quad w, \lambda > 0, \quad (4.9)$$

where λ, w are two parameters. The mean and variance of this two-parameter Weibull distribution can be expressed as

$$\mu = w\Gamma\left(1 + \frac{1}{\lambda}\right), \quad (4.10)$$

$$\sigma^2 = w^2\Gamma\left(1 + \frac{2}{\lambda}\right) - \mu^2. \quad (4.11)$$

Eqs. 4.11 and 4.12 can be rewritten as:

$$w = \frac{\mu}{\Gamma\left(1 + \frac{1}{\lambda}\right)}, \quad (4.12)$$

$$\lambda = \frac{-2 \ln w^{-\lambda}}{\ln \frac{\sigma^2 + \mu^2}{\Gamma(1 + \frac{2}{\lambda})}}. \quad (4.13)$$

If the mean and variance of variable X are known, the values of these two parameters w and λ can be obtained by substituting the mean and variance into Eqs. 4.13 and 4.14.

4.2.3.2 Distribution of cavity diameters

After filtering the surface cavity data as described, the probability density function for finding a cavity within a specified size range was computed with the remaining cavity size data. The interval used to calculate the frequency for the brass and stainless steel surface is 0.28 and 0.23 μm , respectively. It was found that the best fit to the majority of size distribution data follows a Weibull distribution in the form Eq. 4.10. From the measured distribution of cavity sizes the mean cavity diameter, denoted as $\mu_{d,\text{meas}}$, and the standard deviation, denoted as $\sigma_{d,\text{meas}}$, are found. Here, $\mu_{d,\text{meas}} = 4.72 \mu\text{m}$, $\sigma_{d,\text{meas}} = 3.9 \mu\text{m}$ for brass surface; $\mu_{d,\text{meas}} = 2.68 \mu\text{m}$, $\sigma_{d,\text{meas}} = 1.79 \mu\text{m}$ for stainless steel surface. With the exception of a couple of data points, the Weibull distribution fits the data reasonably well as shown in Figs. 4.7 and 4.8. It is observed that the cavity mouths on the stainless steel surface are statistically smaller than those on the brass surface, which partially accounts for the smaller nucleation site density on the stainless steel surface compared with the brass.

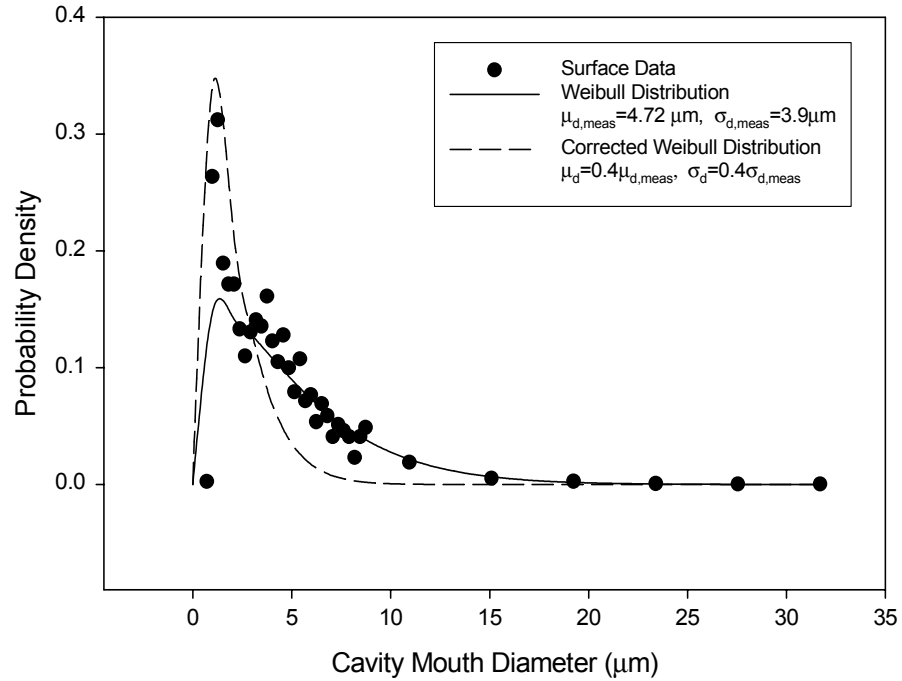


Figure 4.7. Cavity mouth diameter distributions for brass surface.

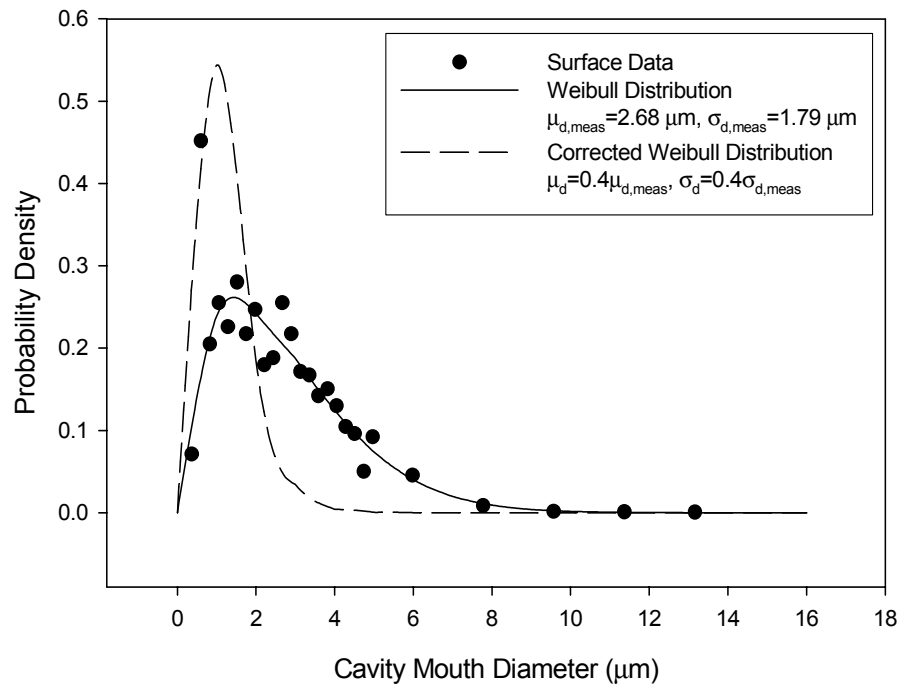


Figure 4.8. Cavity mouth diameter distributions for stainless steel surface.

4.2.4 Distribution of Cavity Half-cone Angles

Of the remaining cavity data, it was found that the probability density distribution of cavity half-cone angles are best represented with the function,

$$g(\beta) = \frac{A\left(\frac{\pi}{2} - \beta\right)^2}{B + \left(\frac{\pi}{2} - \beta\right)^6}, \quad (4.14)$$

where $A = 0.01913$ and $B = 0.0001$ for the brass surface while $A = 0.091$ and $B = 0.0023$ for the stainless steel surface. Figure 4.9 shows the probability density distribution of cavity half-cone angles for the brass surface compared with Eq. 4.15, while Fig. 4.10 shows the same data on a log-log scale. Figures. 4.11 and 4.12 show similar trends for the stainless steel surface. It is of significant interest to note at smaller cavity half-cone angles, $g(\beta)$ follows the scaling law $\left(\frac{\pi}{2} - \beta\right)^{-4}$. This behavior is indicative that the cavity geometry has a fractal nature. Yang et al. (2001) also suggested that the nucleation site density of a heating surface has the fractal feature. It is also particularly noteworthy that finding cavities with smaller half-cone-angles is a very low probability event.

Following Bankoff's gas trapping criterion, on the brass surface only cavities with half-cone angles less than $\beta = 0.635$ radians can serve as nucleation sites since the liquid/solid contact angle for water on brass was measured to be $\theta = 1.27$ radians. To satisfy the gas trapping criterion on the stainless steel surface, the half-cone angle must be less than $\beta = 0.675$ since the liquid/solid contact angle $\theta = 1.35$. It is observed from Figs. 4.9, 4.10, 4.11, and 4.12 that finding a cavity that satisfies the gas trapping criterion is a very low probability event. In fact, it has been observed that only very deep cavities

satisfy the vapor-trapping criterion. This may give some insight as to why rougher surfaces tend to produce more nucleation sites.

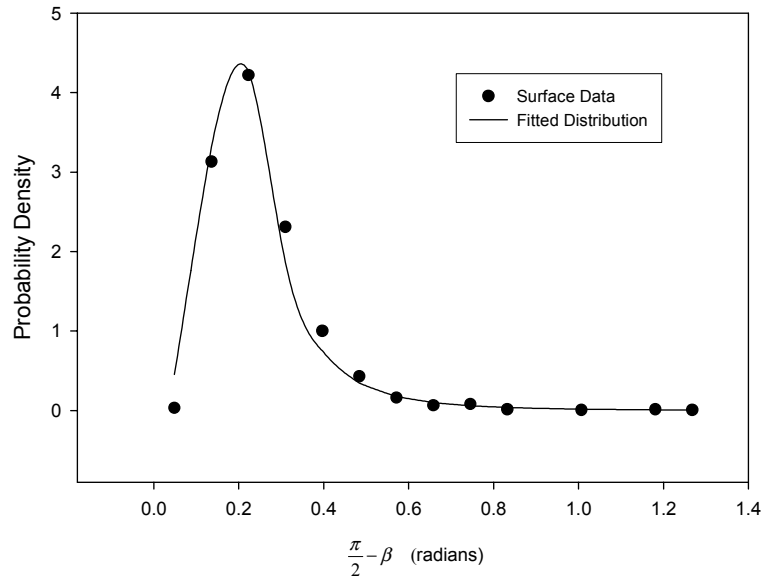


Figure 4.9. Cavity half-cone angle distribution for brass surface using the linear scale.

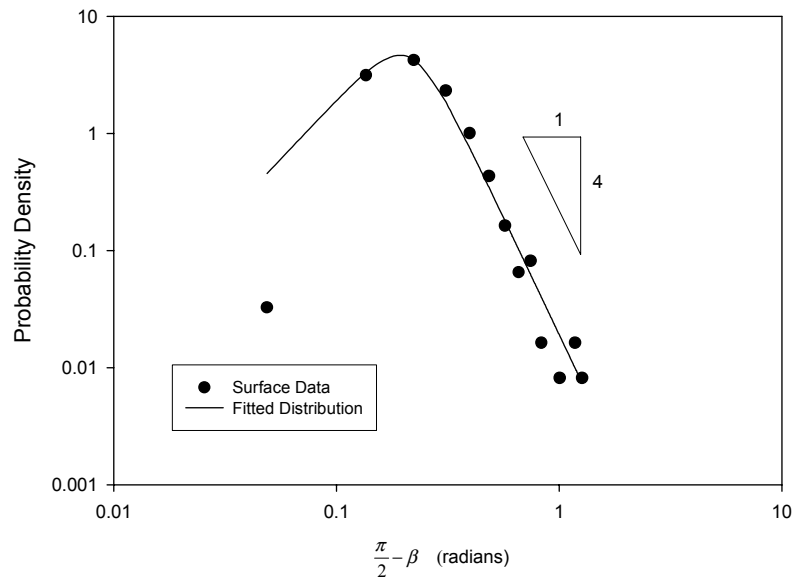


Figure 4.10. Cavity half-cone angle distribution for brass surface using the log-log scale.

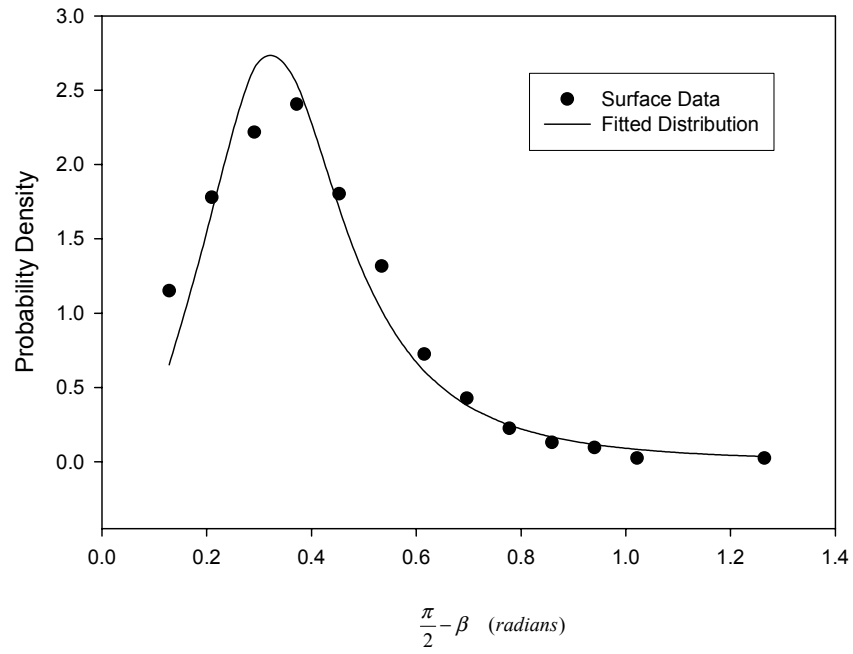


Figure 4.11. Cavity half-cone angle distribution for stainless steel surface using the linear scale.

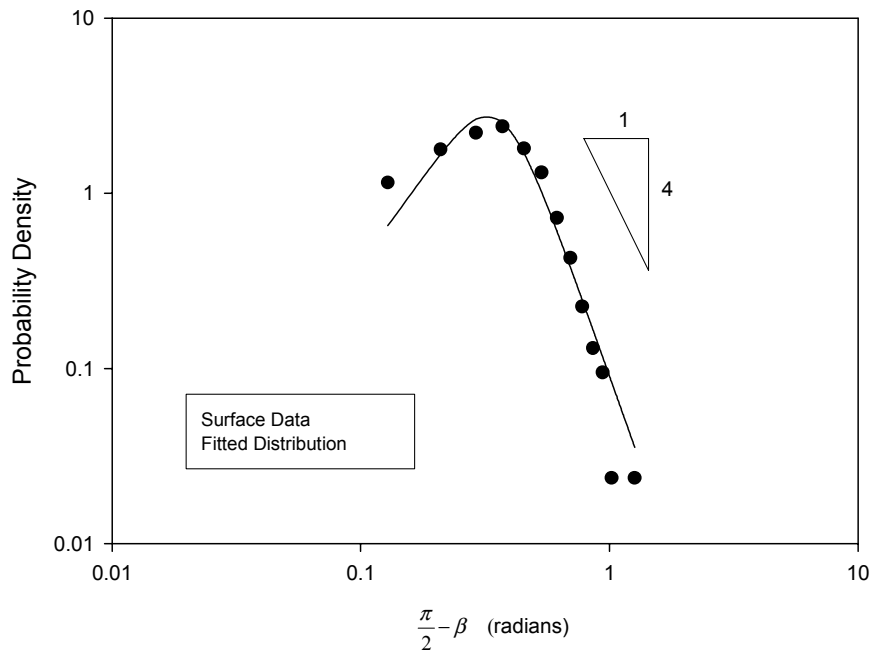


Figure 4.12. Cavity half-cone angle distribution for stainless steel surface using the log-log scale.

4.3 Prediction of Nucleation Site Density

Here the statistical method is used to predict nucleation site density. Following Yang and Kim (1988) an estimation of the nucleation site density is given by

$$\frac{n}{A} = \frac{N}{A} \int_{2r_{min}}^{2r_{max}} f_{3D}(d) dd \int_0^{\theta/2} g(\beta) d\beta, \quad (4.15)$$

where $\frac{N}{A}$ is the number of cavities per unit area, $f_{3D}(d)$ is the probability density distribution of cavity size, $g(\beta)$ is the probability density distribution of cavity half-cone angles, r_{min} and r_{max} are the minimum and maximum cavity radius which will permit the incipience of vapor bubbles and θ is the contact angle. Based on the investigation of Bankoff (1958), the vapor entrapment condition is expressed as $\theta > 2\beta$. This means that cavities with half-cone angle larger than $\theta/2$ cannot entrap gas or vapor; thus, these cavities cannot be activated under heterogeneous nucleation theory. Only those cavities with half-cone angle smaller than $\theta/2$ have the possibility to be activated. So the second integration upper limit is set as $\theta/2$.

4.3.1 Prediction with Gas Nucleation Results

The upper limit of the first integration term in Eq. 4.16 is set as infinity since there is no thermal boundary in gas nucleation to result in r_{max} . However, it is recognized that if the cavity is too large the cavity will be flooded. This is assured to occur with cavity sizes much larger than those observed on the surface and it is not considered in this analysis. r_{min} is evaluated from Eq. 3.1. Although it has been assumed that the cavity mouths are circular in shape, it is recognized that their shape is likely to be non-uniform. Therefore, the identification of cavity diameters from a two-dimensional profile is biased.

In determining the parameters w and λ for the Weibull distribution using Eqs. 4.13 and 4.14 the measured mean cavity mouth diameter and standard deviation are corrected. $f_{3D}(d)$ is modified from Eq. 4.10 by using $\mu_d=C\mu_{d,meas}$ and $\sigma_d=C\sigma_{d,meas}$ in Eqs. 4.13 and 4.14 where $C=0.4$ is an empirical correction. The modified distribution, f_{3D} , is also shown in Figs. 4.7 and 4.8. For the 1412 brass cavities, $\frac{N}{A} = 2.1 \times 10^5$ cavities/cm², and $\frac{N}{A} = 2.37 \times 10^5$ cavities/cm² for the stainless steel cavities. The last integral in Eq. 4.16 represents the probability of finding a cavity with $\beta < \theta/2$. As mentioned earlier, this is a very low probability event, and the degree of accuracy to be expected from a fitted distribution at such low probability is poor. Therefore, the last integral in Eq. 4.16 is replaced by the measured probability $P(\beta < \theta/2)$ even though it also has large statistical uncertainty. $P(\beta < \theta/2)$ is 0.0028 for the brass surface and 0.012 for the stainless steel surface.

Combining Eqs. 4.10 and 4.16 the estimated nucleation site density variation with $\frac{\Delta p}{2\sigma}$ for the brass and stainless steel surfaces are respectively shown in Figs. 4.13, 4.14, and 4.15. There are several observations worthy of discussion. The first is that the apparently good agreement for the brass surface is purely fortuitous. As seen in Figs. 4.14 and 4.15 there is considerable error between the predicted and measured $\frac{n}{A}$ on the stainless steel surface. The cause of this error is the very large statistical uncertainty associated with the probability of finding gas-trapping cavities. One approach to reducing the statistical uncertainty is to increase the sample size by several orders of magnitude.

The main drawback with this approach is that it would be restrictively laborious. As it is, many hours of labor were required just to obtain the current sample size.

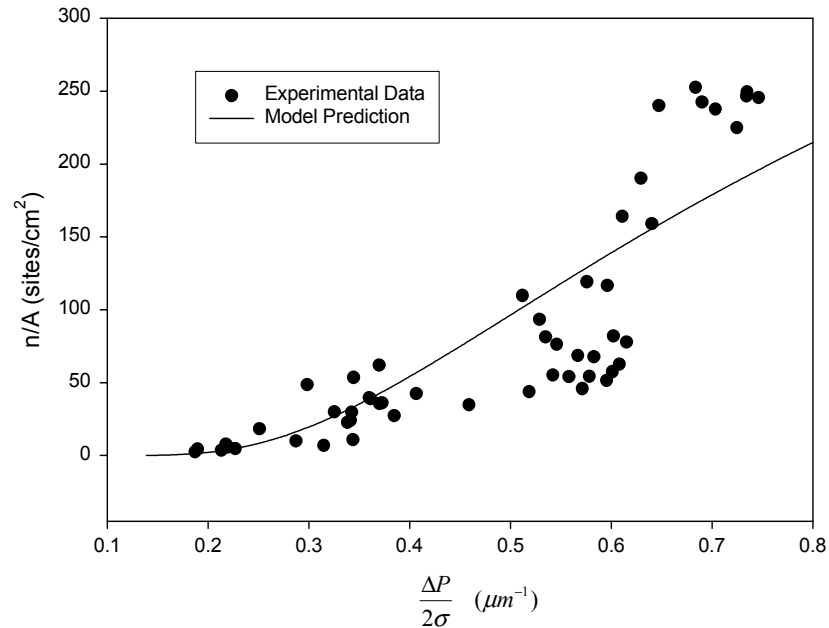


Figure 4.13. Comparison between measured and predicted nucleation site density on brass surface.

A basic premise in using the statistical method for predicting nucleation site density is that the statistical distribution of cavities on the surface is homogeneous. While this appears to be valid for the distribution of cavity mouth diameters and half-cone angles in general, the distribution of cavity half-cone angle that actually trap vapor appears to be inhomogeneous. This is likely the reason nucleation sites are non-uniformly distributed on the nucleating surface.

These findings suggest that the statistical method for predicting nucleation site density on commercial heat transfer surfaces with randomly distributed cavities is not likely to be accurate using the current state-of-the-art in surface metrology technology. However, the qualitative trends predicted by the model are supported by the data.

Therefore, the model may be useful in designing specially prepared surfaces that promote high nucleation site density and heat transfer.

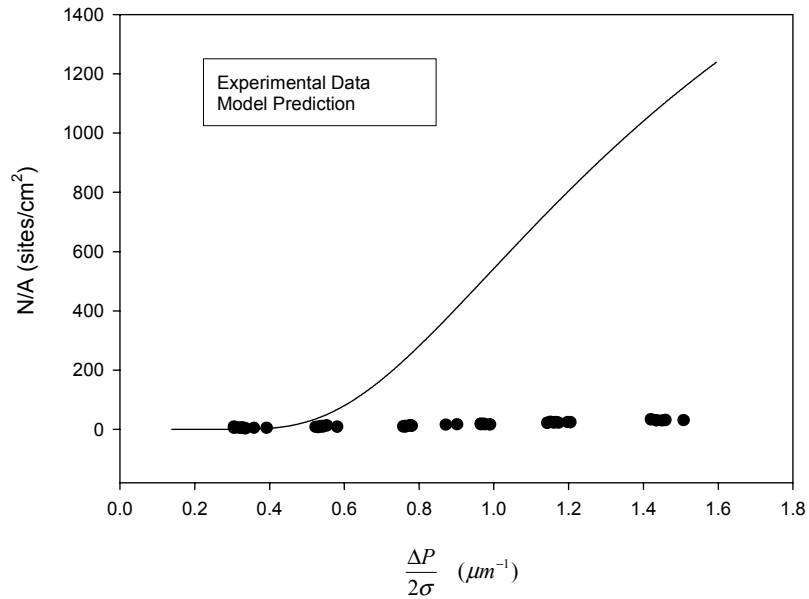


Figure 4.14. Comparison between measured and predicted nucleation site density on stainless steel surface.

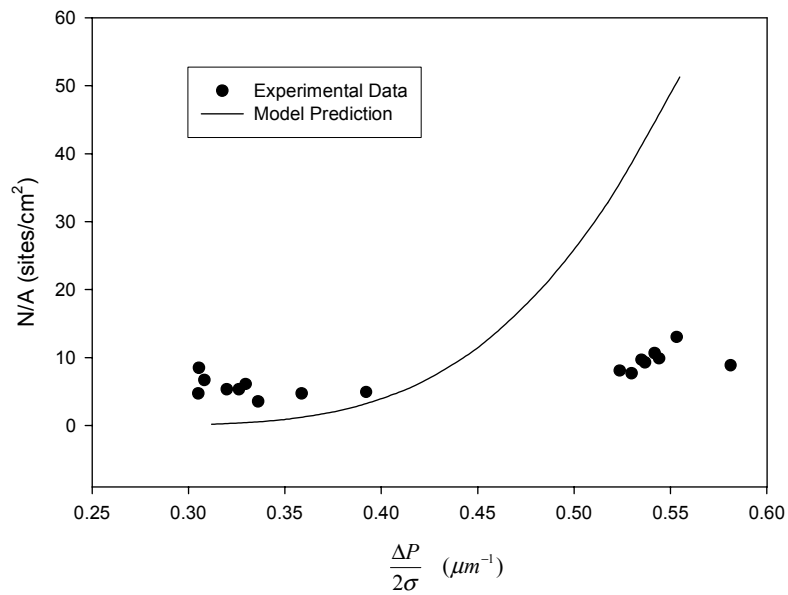


Figure 4.15. Comparison between measured and predicted nucleation site density on stainless steel surface within low pressure change range.

4.3.2 Prediction with Pool Boiling Results

According to Hsu (1962) r_{min} and r_{max} for pool boiling are estimated from Eqs. 4.4 and 4.5. Two constants in Eqs. 4.4 and 4.5 are evaluated using $C_1 = \frac{1 + \cos \phi}{\sin \phi}$ and $C_2 = 1 + \cos \phi$, where ϕ is angle between the side of the vapor embryo at the triple contact point and the horizontal. Here $C_1=1.0$ and $C_2=1.0$ for the brass surface; $C_1=0.84$ and $C_2=0.83$ for the stainless steel surface. Since finding vapor trapping cavities is a very low probability event and the accuracy from a fitted distribution of cavity half-cone angles is poor, the last integral in Eq. 4.16 is determined from the measured $\frac{n}{A}$ for gas nucleation. This integral value is 0.0028 for the brass surface and 0.0005 for the stainless steel surface. Figure 4.16 shows a comparison between the measured and predicted pool boiling nucleation site density for water on brass. Here, the prediction is in excellent agreement with the measurements. Figure 4.17 shows a comparison between the measured and predicted pool boiling nucleation site density for water on stainless steel. Here the measured nucleation site density is significantly greater than the prediction. This raises the possibility of another mechanism seeding boiling nucleation in addition to vapor trapping cavities.

4.3.3 Discussion

This study presented a method to find the characteristic dimension associated with a cavity on the surface although future study needs to concentrate on finding a unique way to fully use the three dimensional information gained by scanning process. Probability density distributions of cavity mouth diameter and half-cone angle are also presented. Due to the limited resolution more data in the small diameter range are

necessary to construct a more reasonable cavity mouth distribution curve. This is also suggested by the observation that the prediction curve will change to convex shape if the diameter distribution curve tends to be flat.

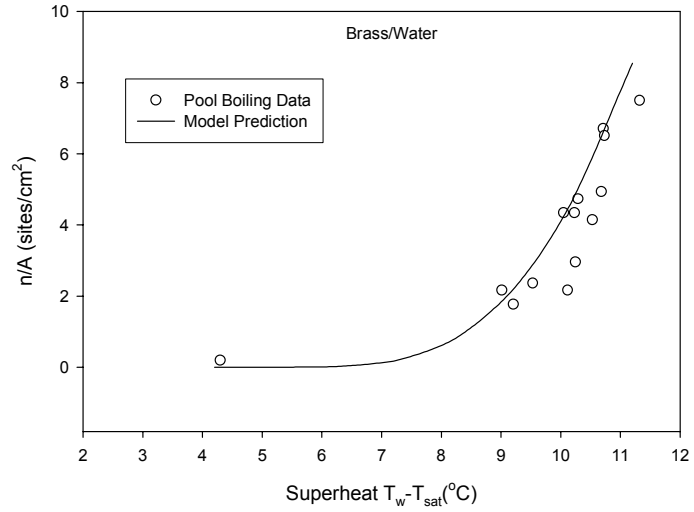


Figure 4.16. Comparison between measured and predicted nucleation site density on brass surface using water.

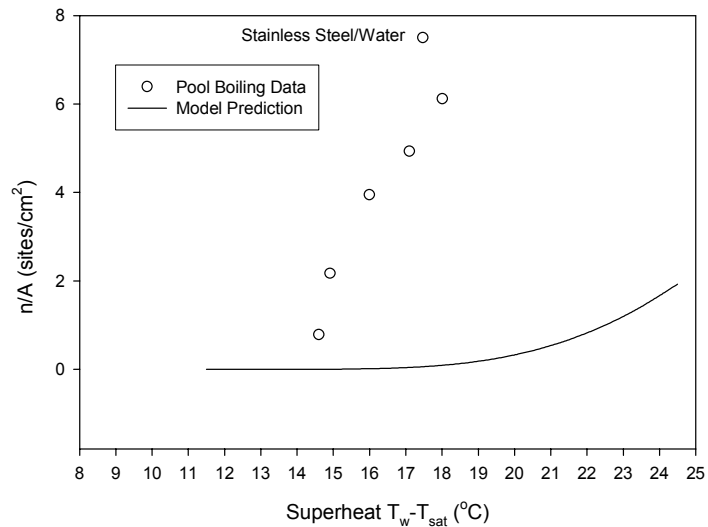


Figure 4.17. Comparison between measured and predicted nucleation site density on stainless steel surface using water.

CHAPTER 5 HETEROGENEOUS NUCLEATION WITH ARTIFICIAL CAVITIES

The main shortcomings of the statistical models discussed in Chapter 4 are (1) they do not allow for interference from adjacent sites, (2) the critical radius is calculated based on a mean wall superheat, when in reality the wall superheat for heterogeneous nucleate boiling surfaces experiences substantial temporal and spatial variations and (3) the model assumes all nucleation sites are found at cavities. Kenning and Del Valle (1981) argued that as the heating surface becomes increasingly populated with nucleation sites, adjacent sites may thermally interfere with one another. Calka and Judd (1985) found that existing nucleation sites tend to activate adjacent sites that are within a distance of a bubble diameter and inhibit the formation of sites that are at a distance greater than a departure diameter and within three departure diameters of the active site. No influence of the active site was noted at a distance greater than three departure diameters. Golobic et al. (1996) and Kenning and Yan (1996) used liquid crystal thermography to demonstrate that large spatial and temporal variations of wall superheat are characteristic of boiling surfaces and thermal interference between adjacent nucleation sites occurs even at low heat fluxes. The studies by Wienecke et al. (1999) of a single active nucleation site on a vertical plate in pool boiling, showed that unlike the horizontal pool boiling case, successive bubbles did not always activate at the same local superheat. The variability increased with increasing heat flux. It was suggested that the observed behavior could not be explained in terms of time-averaged temperature gradients at the wall. Most

recently, Gjerkes and Golobic (2002) studied the interaction between an artificially activated nucleation site and a naturally activated nucleation site. The results showed that the influence of active nucleation sites on each other's activity is mutual. Others who studied nucleation site interaction include Gorenflo et al. (1998), Zhang and Shoji (2003), and Chatpun et al. (2004). These data cast doubt as to whether each cavity on a surface has a unique critical radius required for nucleation. Pasamehmetoglu and Nelson (1991), Pasamehmetoglu et al. (1993), and Sadasivan et al. (1995) developed a large-scale computer simulation that explored the interactions between hundreds of randomly distributed nucleation sites. This multi-cell model demonstrated the importance of transient conduction and resultant thermal interaction among nucleation sites, which could lead to non-linear behavior.

As discussed previously, the bubble interactions and possible nonlinear nature impede the development of a mechanistic model of nucleation boiling. Another difficult problem involved is that the actual surface structure is very complicated and capturing the appropriate surface characteristics is difficult as discussed in Chapter 4. A possible way to clarify these discrepancies is to simplify the process as much as possible, and using artificial cavities will advance the understanding of the principles of nucleation boiling.

5.1 History and Review

Griffith and Wallis (1960) were the first to develop a predictive model for the minimum wall superheat required to activate a conical vapor trapping cavity formed on a copper surface with a steel gramophone needle. With water they observed that the measured wall superheat required to activate the artificial cavity is in reasonably good agreement with the prediction. Sernas and Hooper (1969) observed boiling nucleation

from artificial cavities made with a diamond phonograph needle on a chromel heating strip. It was observed that the activation of water vapor bubbles from the cavities was unstable. Ebullition from the artificial cavities ceased after some time, leaving boiling activity at only naturally formed sites. Preckshot and Denny (1967) studied the ebullition of carbon tetrachloride from conical and cylindrical cavities. It was observed that steep walled and deep cavities served as the best sites for nucleation. The cavity depth to mouth diameter ratio should exceed unity in order to activate cavities with a highly wetting fluid. Rammig and Weiss (1991) investigated nitrogen incipience, bubble growth and departure from artificial cavities with mouth diameters ranging in size from 27 to 70 μm . It was observed that the 0.04°K superheat required to activate the 70 μm cavity is in good agreement with the incipience model suggested by Griffith and Wallis. Kosky (1968) studied the dynamics of the meniscus as water vapor bubbles depart from a 100 μm glass capillary tube. High speed cinematography revealed that the meniscus penetrates deep into the capillary tube just following bubble departure. The maximum penetration ranged from 200-300 μm .

Heled et al. (1970) manufactured an array of cylindrical cavities on a highly smooth surface electroplated with nickel. They studied pool boiling heat transfer rates with highly and moderately wetting fluids. Surfaces with more densely packed arrays of cavities yielded higher heat transfer rates. Messina and Park (1981) also studied pool boiling heat transfer of R113 from polished copper surfaces in which a precise array of pits was formed using wet etching. It was observed that increasing the pit density enhances the heat transfer rate. It was also observed that extremely shallow or jagged pits were substantially more efficient for nucleation than well-formed pits.

Recently Shoji and Takagi (2001) and Shoji and Zhang (2003) conducted extensive stability and dynamical studies of bubble incipience with water on a thin copper surface. The smooth surface contained conical, cylindrical, and re-entrant artificial cavities that were manufactured using diamond bit pricking and micro-electrical discharge machining. It was observed that cylindrical and re-entrant cavities are typically stable, while conical cavities demonstrate intermittent behavior. It was also found that cavities with a smaller mouth diameter are typically more stable than those with a larger mouth diameter.

In a very recent investigation Pesse et al. (2004) studied the gas entrapment process in precisely manufactured rectangular cavities with entrance widths of 5, 15, 30, and 50 μm . The cavities were manufactured by micromachining rectangular channels into silicon and adhering a glass cover over the channels to form the cavities. Isothermal tests were conducted with water flooding the test surface. Different cleaning procedures were used to alter the wettability conditions. In all cases, the liquid/solid contact angle is less than the cavity minimum side angle (90°). Air is initially trapped as water spreads over the cavities, and the cavities eventually flood as air diffuses into the water. The time scale for flooding ranges from hours to days. For larger contact angles a single meniscus typically forms, while for smaller contact angles two menisci typically form within the cavity.

According to the vapor trapping heterogeneous nucleation theory proposed by Griffith and Wallis a convex vapor meniscus will protrude from a vapor trapping cavity, with radius r , as shown in Fig. 5.1 and the amount of wall superheat required to activate that cavity for boiling is

$$\Delta T_{sat} = \frac{2\sigma T_{sat}}{\rho_v h_{fg} r}, \quad (5.1)$$

where σ is the surface tension, ρ_v is the vapor density, and h_{fg} is the latent heat of vaporization. When the gas nucleation technique (discussed in detail by Lorenz (1974), Eddington and Kenning (1978,1979), and Qi and Klausner (2004) is used to activate the same cavity the magnitude of depressurization required is

$$\Delta P = \frac{2\sigma}{r}. \quad (5.2)$$

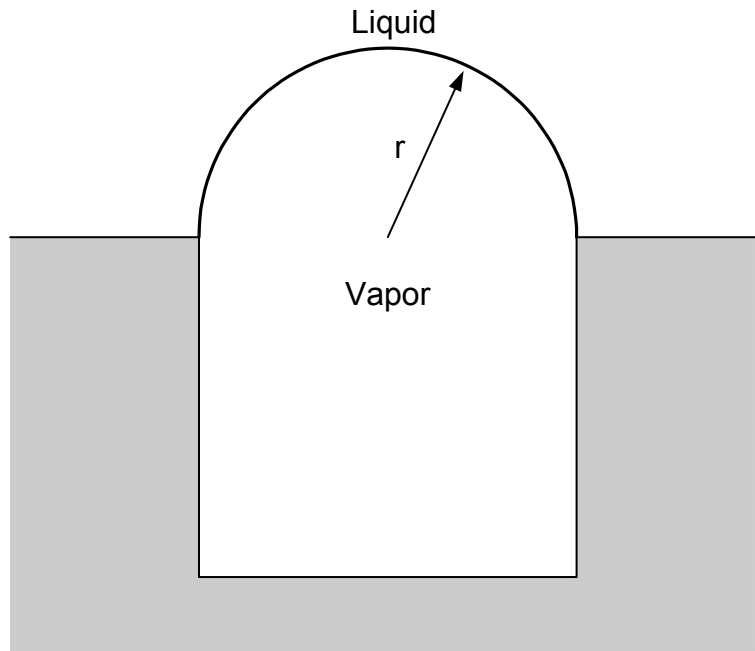


Figure 5.1. Convex vapor meniscus protruding from a cylindrical cavity.

Cornwell (1982) was unconvinced that re-entrant cavities on naturally formed surfaces were responsible for incipience in boiling. Instead, he studied the micro-roughness inside cavities and taking into account contact angle hysteresis he demonstrated that a concave meniscus, as shown in Fig. 5.2a can be stable in the system. The observations of Kosky (1968) in a glass capillary tube seem to support this idea. The amount of superheat required to activate a cavity with a concave meniscus will depend on its radius of curvature R . The maximum superheat required occurs when the meniscus

radius of curvature equals the cavity diameter, $r=R$. In order to activate the cavity the meniscus first needs to be flipped over as shown in Fig. 5.2b and then activated. The maximum superheat required to achieve incipience is double that predicted by Eq. (1). Likewise, the magnitude of the maximum depressurization required to activate a cavity with a concave meniscus, as shown in Fig. 5.2a, is double that given by Eq. (2).

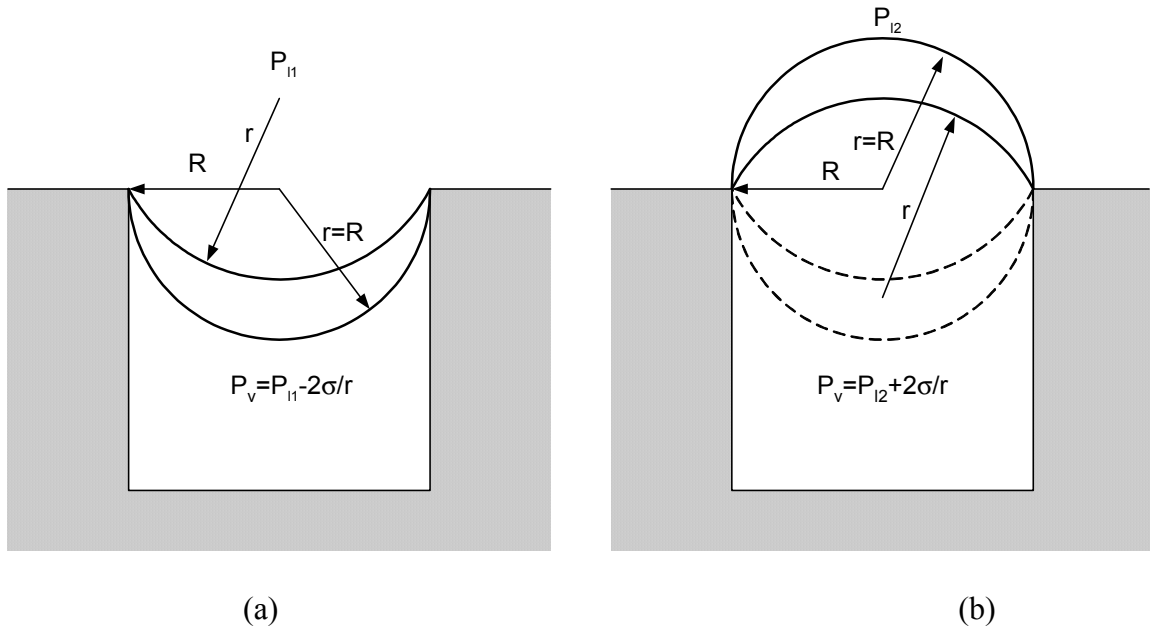


Figure 5.2. Schematic drawing of liquid/vapor interface.

(a) Stable Concave meniscus (b) Convex meniscus protruding from a cylindrical cavity

5.2 Cavity Fabrication Methods

5.2.1 Lithography

The lithography process includes the wafer surface preparation, applying the photoresist, alignment of the mask and wafer, exposure and developing. A schematic drawing of lithography process is shown in Fig. 5.3.

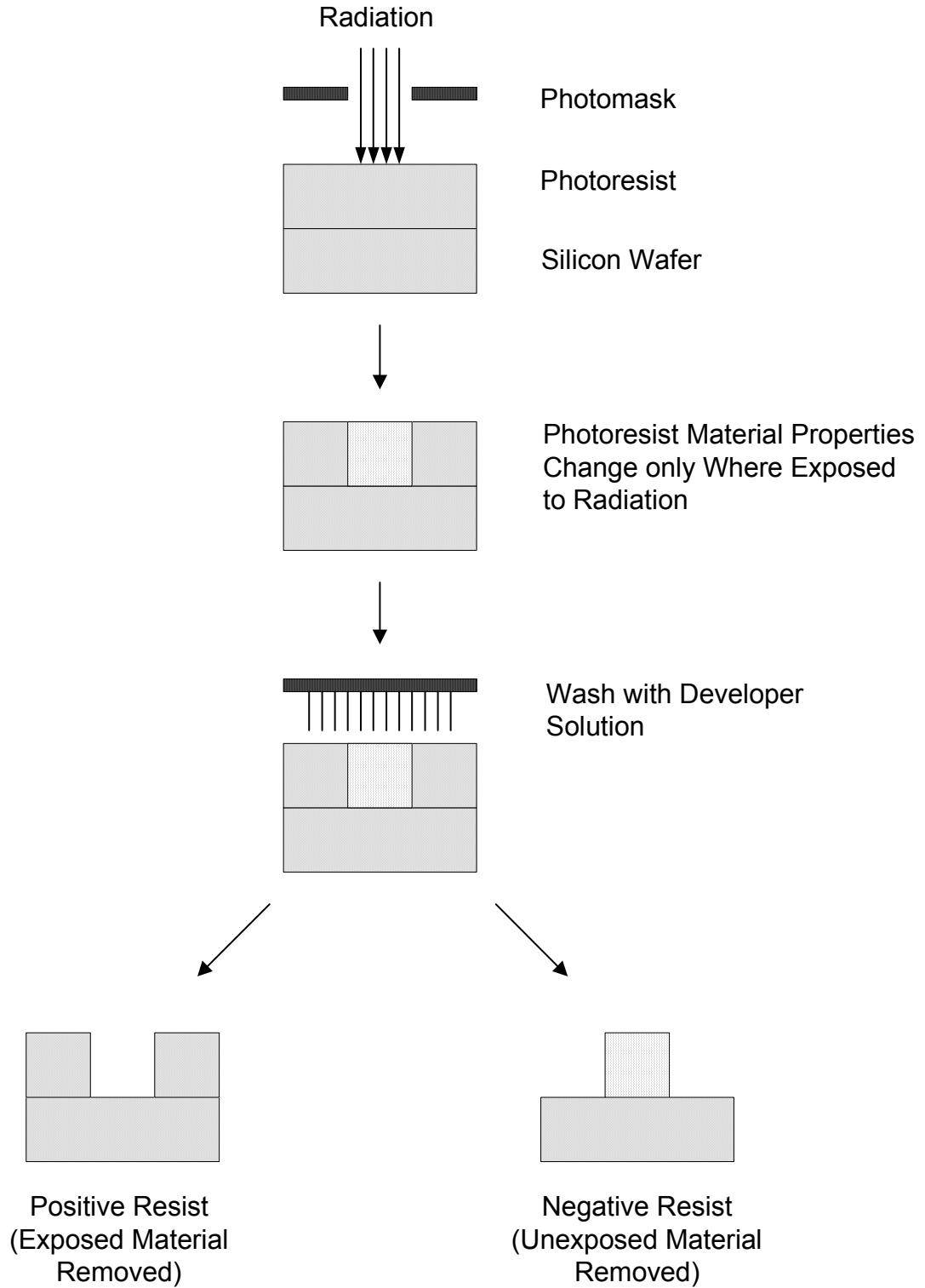


Figure 5.3. Lithography process.

5.2.1.1 Photomask design

In order to use the lithography technique, a pattern (photomask) must be designed geometrically using a CAD system. The photomask is divided into 6 areas, as shown in Fig. 5.4.

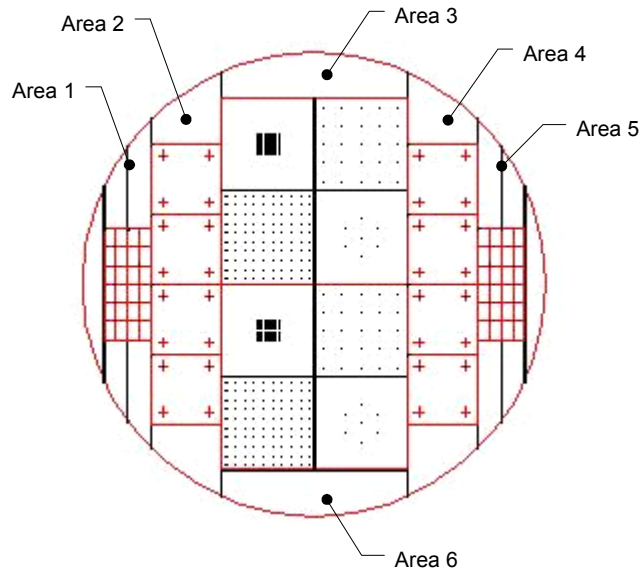


Figure 5.4. Photomask overview.

The schematic drawing of Area 1, which is same as Area 5, is shown in Fig. 5.5 a. In order to investigate the cavity size effect on heterogeneous nucleation, this area is designed to make the cavities with different sizes and same depths. There are 10 circles with diameter ranging from $2\ \mu\text{m}$ to $60\ \mu\text{m}$. The distance between the centers of circles is 4 mm.

The schematic drawing of Area 2, which is same as Area 4, is shown in Fig. 5.5 b. In order to reveal the effect of cavity shapes on bubble nucleation, this area is designed to make the cavities with different shapes. The designed shapes include circle, square, triangle and rectangle. The dimensions are summarized in Table 5.1.

Table 5.1 Cavity design dimensions in area 2 of the photomask

	Circle Diameter (μm)	Rectangle Width \times Length (μm)	Square Edge Length (μm)	Equilateral triangle Lateral Length (μm)
1	2	2 \times 20	2	1.74
2	6	6 \times 60	6	5.22
3	10	10 \times 100	10	8.7
4	14	14 \times 140	14	12.1

The schematic drawing of Area 3, which is same as Area 4, is shown in Fig. 5.5 c. Four cavity patterns are considered, which include a 10 \times 10 matrix with spacing 0.5 mm, a 10 \times 10 matrix with spacing 2 mm, a 5 \times 5 matrix with spacing 5 mm, and hexagon with edge length 5 mm. All circles have uniform diameter 10 μm . Detailed geometry dimensions are listed in Table 5.2.

Table 5.2 Cavity design dimensions in area 3 of the photomask

Pattern		Matrix 10 \times 10	Matrix 10 \times 10	Matrix 5 \times 5	Hexagon
Spacing	Transverse direction	0.5 mm	5 mm	2 mm	The distance between two adjacent circles is 5 mm.
	Longitudinal direction	0.5 mm	5 mm	2 mm	

After finishing the design, the document was sent to the photo science Inc. who manufactured the mask.

5.2.1.2 Spin coating

Spin coater 2 with PWM32 controller has been used in this study. A polymer drop, photoresist, is applied on the center of the silicon wafer that is mounted on the rotatable chunk of the spin coater. Here, AZ9260 from AZ Electronic Material is chose as the photoresist. The wafer is then spun at a very high speed. So the droplet is spread very evenly across the wafer surface and a uniform layer of photoresist is achieved on the wafer.

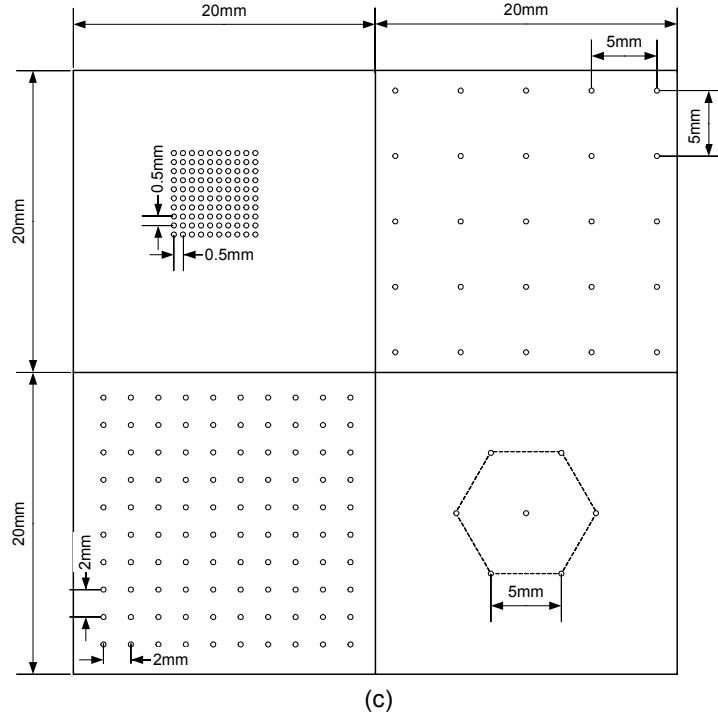
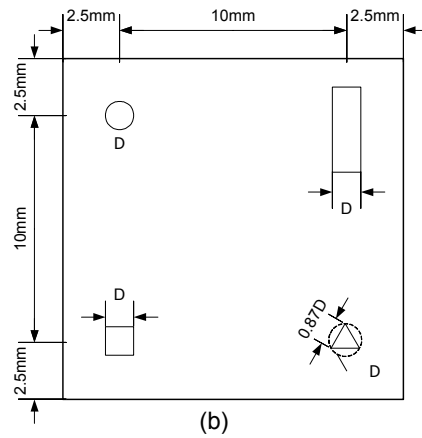
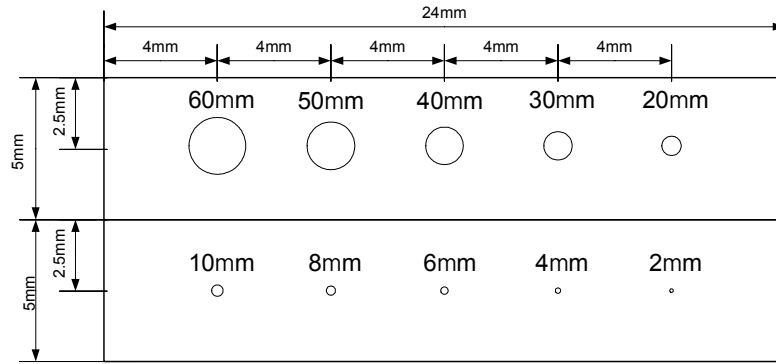


Figure 5.5. Schematic drawing of the photomask.

5.2.1.3 Pattern transfer

After the spin coating, the wafer and photomask are loaded into Karl Suss MA-4 mask aligner, a precision mask alignment and exposure system. The alignment system utilizes a high intensity chromatic light source that produces large infrared output. After aligning with the photomask, the wafer is exposed under the UV light produced by a 350W high pressure mercury lamp. The selected exposure time is 35 S. The pattern of the mask is now transferred into the photoresist on the surface of the wafer. In this study, a positive resist is used. The chemical properties of the photoresist will change after exposed to a radiation source and the irradiated and non-irradiated regions on the resist have different solubility in a particular solvent (developer). As the characteristic of positive resist, the exposed areas are dissolved, whereas the non-exposed areas remain untouched. AZ300 MIF developer is used and the appropriate develop time is 270 S. Thus, the subsequent process such as etching is possible.

5.2.2 DRIE Etching

To etch a cavity on the substrate, two etching processes may be used. One is the wet etching where the material is dissolved when immersed in a chemical solution as the way Messina and Park (1981) used and the other is the dry etching where the material is removed using reactive ions or vapor phase etchant. The cost of wet etching is small, however, the undercutting under the photoresist will be large. Compared with the wet etching, using deep reactive ion etching (DRIE) can achieve very small features, nearly vertical sidewalls and 3-4 times higher etch rates than the wet etching. DRIE etching was used in this study. The schematic illustration of the process is shown in Fig. 5.6. The etch cycle uses chemically reactive neutrals (eg. F) and ions (eg. SF_x^+) that are accelerated under the high frequency electromagnetic field to etch silicon. In the

passivation cycle, a fluorocarbon polymer is deposited on the bottom and sidewall of a trench. In the following etch cycle, the reactive species remove the protective layer at the bottom, but the film remains relatively intact along the sidewall. The repetitive alternation of these two cycles result in a very directional etch which exhibits good surface planarity.

The DRIE facility manufactured by Surface Technology Systems (STS) is used in this study. With its inductively coupled plasma (ICP) technology, this system can anisotropically etch for wide range of materials including compound semiconductors, metals, dielectrics, ferroelectrics, polymers and magnetic materials.

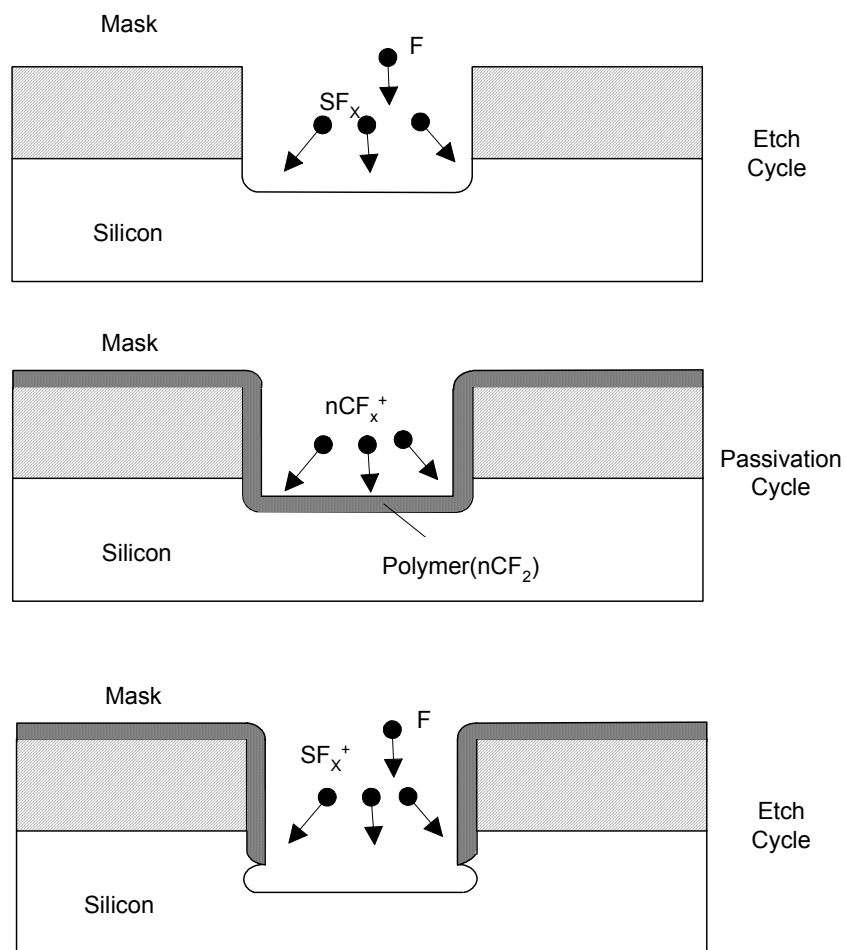


Figure 5.6. Deep reactive ion etching process.

5.2.3 Wafer Cleaving Procedure

After the wafer is etched and the features are on it, the chips are separated by cleaving crystalline silicon wafer using a diamond tipped scribe. The operation is described as follows. First, press the tip of the scribe at the edge of the wafer to make a notch after placing the wafer on several cleanroom wipes on a flat place. Then insert the tip of the scribe underneath of the wafer and press on the wafer with even force. This will cause the crack to propagate across the silicon wafer along its natural cleaving planes. However, dicing saw is recommend from my personal experience.

5.2.4 Wafer Cleaning

In order to remove the organic, ionic and metallic contamination covered on the tested chip after running the experiments for a long period of time, a standard procedure of wafer cleaning is set up. The procedure is described as follows:

- (1) Heat appropriate amount of Nitric Acid (HNO_3) in a Pyrex beaker on a hot plate.
- (2) Remove beaker from hot plate and add some hydrogen peroxide (H_2O_2). The liquid will begin to bubble vigorously.
- (3) Immerse the wafer chip in the solution for 15 minutes and heat it on the hot plate if it becomes cooler.
- (4) Rinse the chip in running DI water.
- (5) Prepare a fresh solution with sulfuric acid (H_2SO_4) and H_2O_2 .
- (6) Immerse the chip in this solution as procedure 3.
- (7) Immerse in acetone for 1 minute after rinsing the chip with DI water.
- (8) Rinse with methanol and DI water.

After these procedures, the chip will get a shining face again.

5.3 Cavity Measurements

The smallest feature achieved in this study is 8 μm since the selected photoresist AZ9260 is too thick. To achieve a smaller feature a thin resist is required and appropriate spin speed, exposure time, and develop time should be found. The purchased silicon wafer has the specification as listed in Table 5.3.

Table 5.3 Silicon wafer specification

Grade	Test	Diameter	4 inch
Type	P	Resistivity	10.0-20.0 OHM/CM
Dopant	B (Boron)	Thickness	475-575 μm
Orientation	100	Flats	2 SEMI STD

The manufactured artificial cavities with dimension larger than 20 μm are measured by Wyko NT 1000 interferometer. Figure 5.7 shows the features of a 60 μm nominal diameter artificial cavity. Two-dimensional profiles from the scan are shown in Fig. 5.8. It is observed that the cross section of the cavity is very uniform, and micro roughness within the cavity is evident. The bottom of the cavity is nearly flat with some curvature at the corners. Table 5.4 lists the measurements of diameter and depth on the circular cavities.

Table 5.4 Cylindrical cavities measurements

Cavity nominal diameter (μm)	Measured diameter (μm)	Measured depth (μm)	Figures
20	19	40	Appendix C
30	28	42	Appendix C
40	38	42	Appendix C
50	49	42	Appendix C
60	58	43	Figs. 5.7, 5.8

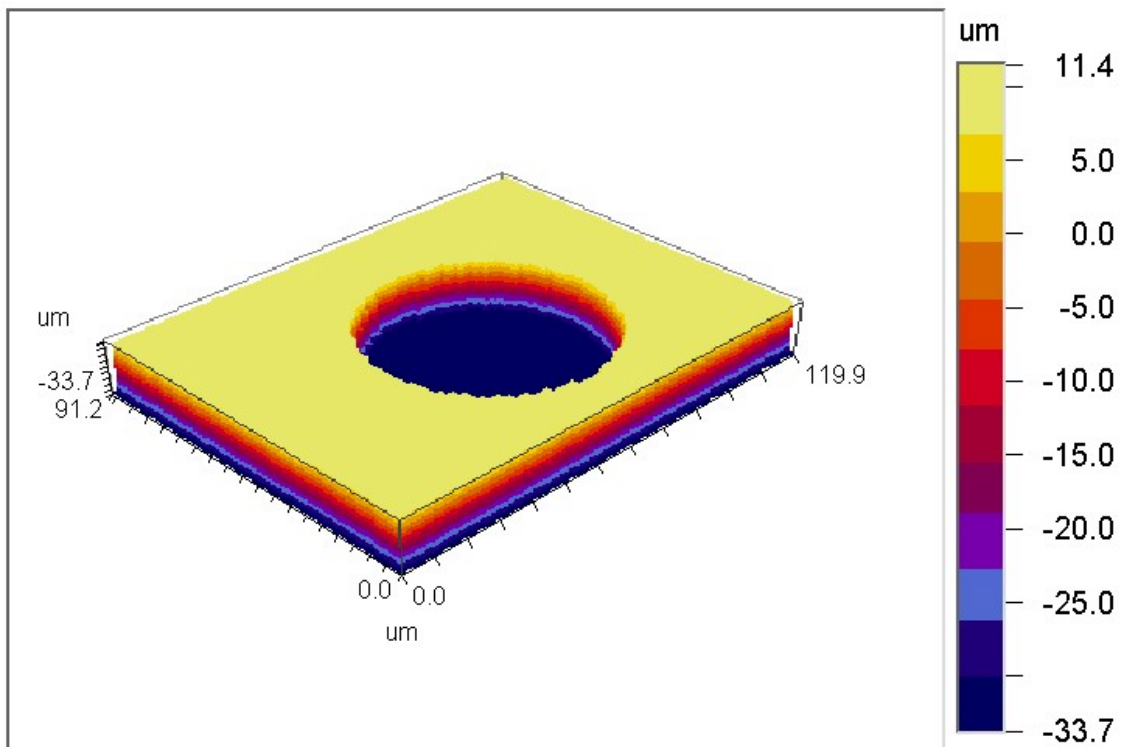


Figure 5.7. Three-dimensional profile of cylindrical cavity with 60 μm mouth diameter and 45 μm depth.

X Profile



Y Profile

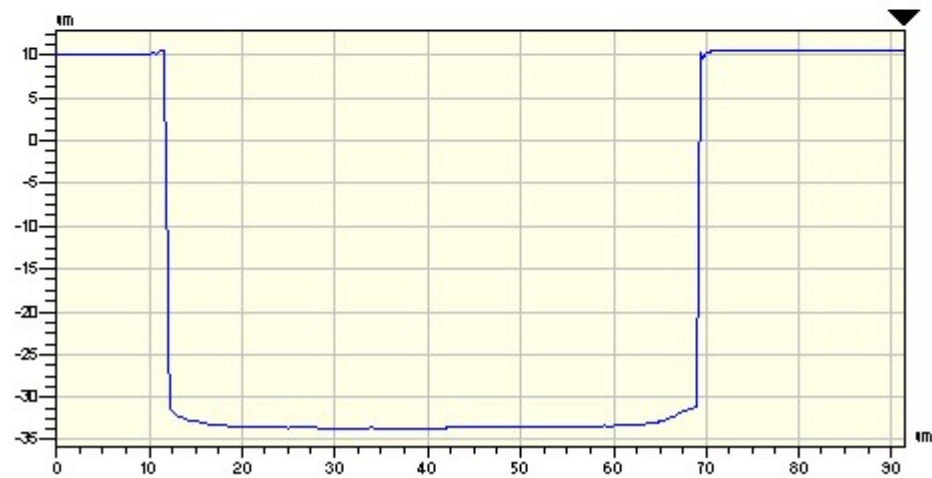


Figure 5.8. 2-D measurement of cylindrical cavity with 60 μm mouth diameter and 45 μm depth.

5.4 Experimental Facilities

The existing gas nucleation and pool boiling facilities, described in Chapter 2 and Chapter 3 and shown in Figs. 2.2 and 3.1, respectively, were used for present experiments.

The silicon surface is adhered to a brass insert, which resides in a 25.4 mm recess at the test section in gas nucleation experiments. The outlet of valve 3 leads either to atmosphere or a pressure regulator attached to a compressed air supply. The pressure regulator permits backpressure to be placed on the test section following depressurization. Since the pressure observed during the experiments covers a wide range, two types of pressure transducers are used to cover different pressure ranges. A Viatran strain gauge type pressure transducer is used to measure the high pressure range (35-150 kPa). A Validyne magnetic reluctance pressure transducer is used to measure the low pressure range (0-35 kPa). The calibration curve is shown in Fig. 5.9. The uncertainty of the Viatran pressure measurement is ± 0.2 kPa and that of the Validyne pressure measurement is ± 0.08 kPa. The uncertainty of the temperature measurement is ± 0.5 °C.

The pool boiling facility is used to compare boiling incipience on the micro-fabricated surface with that in the gas nucleation facility. Heat is supplied to the boiling surface by four high-density cartridge heaters embedded in a brass cylinder. The upper surface of the cylinder is mounted flush with the lower end plate. The silicon boiling surface is adhered to the brass surface using aluminum based high conductivity Duralco 132 cement. Five thermocouples are adhered underneath five fabricated cavities to measure the site temperatures. The pressure in the boiling chamber is measured with a Validyne P2 pressure transducer and has an uncertainty of ± 0.2 kPa. The uncertainty of the temperature measurements is ± 0.5 °C. Prior to recording data, the boiling chamber is allowed to operate with high heat flux for an hour in order to achieve a steady thermal state and degas the facility. The boiling chamber is oriented vertically for all experiments

and visualization of vapor bubble incipience is accomplished with the high-speed digital camera from the side view.

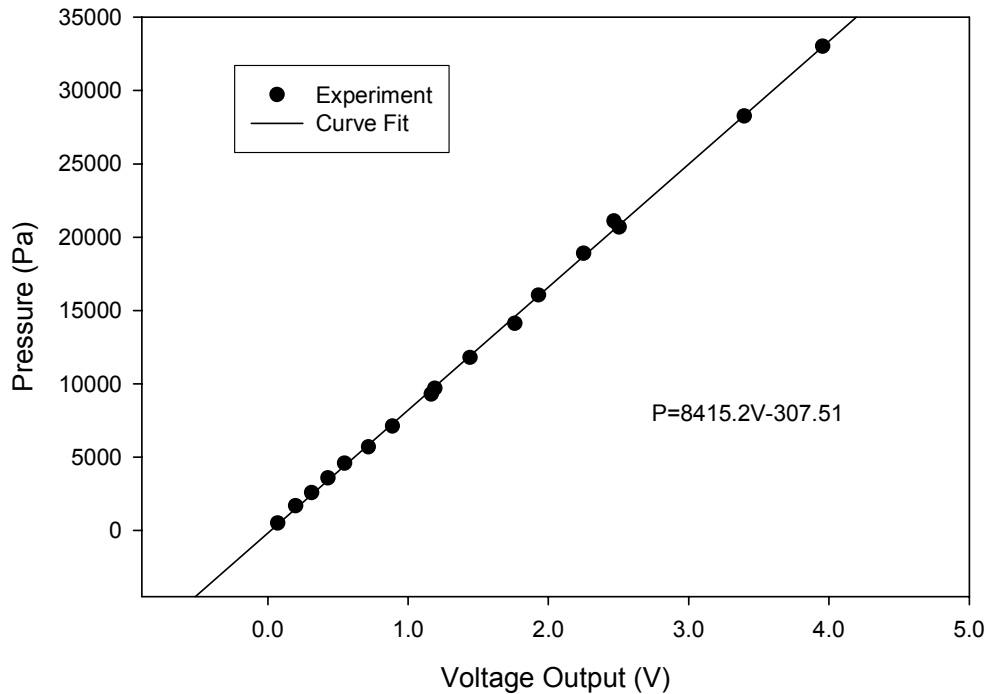


Figure 5. 9. Validyne differential pressure transducer calibration curve.

5.5 Gas Nucleation Experimental Results for Water

5.5.1 Effect of Backpressure on Gas Nucleation Bubble Activation

According to Eq. (5.2), whether or not a bubble is activated at a vapor trapping cavity during gas nucleation depends only on the pressure change during depressurization. It should be independent of the backpressure. However, there has been recent concern that the magnitude of the backpressure may influence bubble activation. In order to study the effect of backpressure on gas nucleation cavity activation, a silicon surface containing a linear array of cylindrical cavities ranging in diameter from 8-60 μm was prepared. Each cavity has a depth of 45 μm and is separated by a spacing of 4 mm

as shown in the layout in Fig. 5.10. The surface was placed in the gas nucleation facility using water as the test fluid with different magnitudes of depressurization (ΔP). During depressurization the test section was either allowed to expand to atmospheric pressure or it expanded to a backpressure ranging from (25-45 kPa). The net depressurization ranged from 11-76 kPa. Following depressurization, each cavity was examined to determine whether or not it activated. The results are summarized in Fig. 5.11. As seen in Fig. 5.11, whether or not backpressure is applied to the test section, there is essentially no difference in the magnitude of depressurization required to activate a cavity with a particular size. The remainder of gas nucleation experiments were done with the test section expanding to atmospheric pressure.

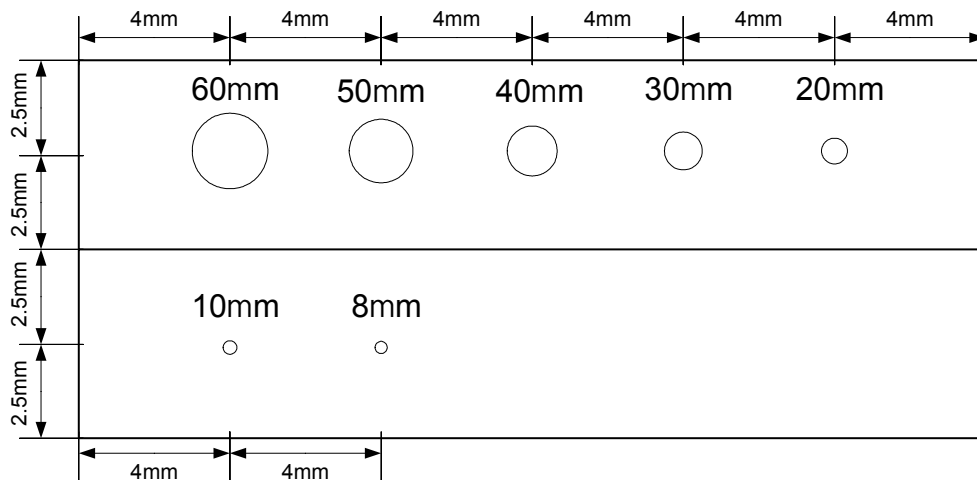


Figure 5.10. Layout of cylindrical cavities on silicon surface.

5.5.2 Activation of an Array of Cylindrical Cavities Using Gas Nucleation

Extensive gas nucleation tests were done with water on the silicon surface with an array of cylindrical cavities laid out as shown in Fig. 5.10.

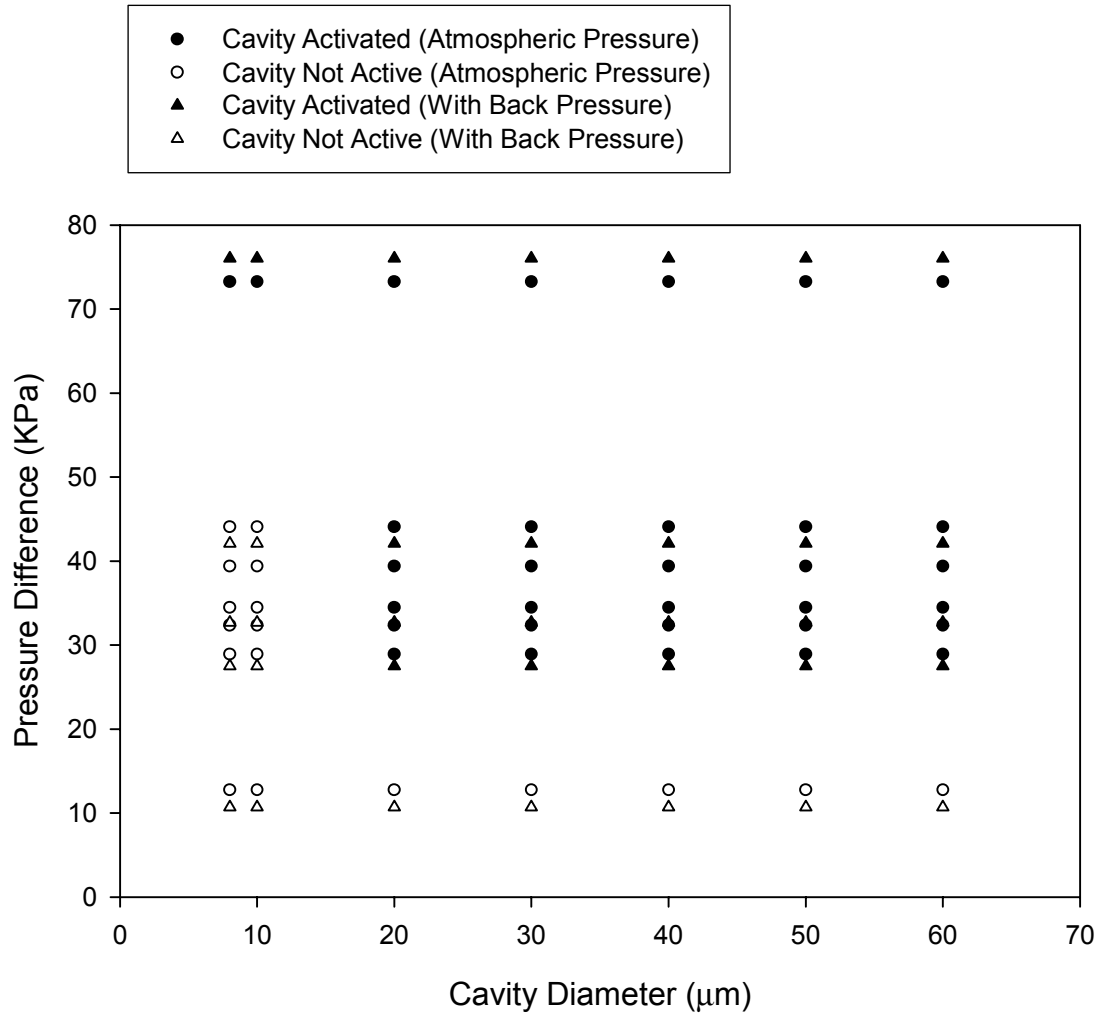


Figure 5.11. The influence of backpressure on gas bubble activation.

Figs. 5.12 (a-g) show photographs of the vapor bubbles protruding the artificial cavities following activation. Knowing the precise location of the cavities relative to one another aided in the identification of site activation. The activation results are summarized in Fig. 5.13. Also shown in Fig. 5.13 is the predicted depressurization required to activate the cavities using the Griffith and Wallis model (Eq. 5.2) and the maximum depressurization required based on the Cornwell hypothesis (double the prediction from Eq. 5.2). There is very good agreement between the observed cavity activation and the prediction based on the Cornwell hypothesis. These data provide

additional evidence to support the supposition that a concave meniscus within the cavity is probable. This is quite a significant result because it demonstrates that the energy potential required to activate a vapor trapping cavity is twice that predicted from Eqs. 5.1 and 5.2, which are commonly used with incipience models.

There are two additional observations of importance from Fig. 5.13. The first is that all cylindrical cavities are stable when activated using gas nucleation. That is, once the depressurization exceeds that required for activation, the cavity activates; adjacent cavities do not interfere with one another. The second observation is that there appears to be a threshold magnitude of depressurization below which no cavity will activate, even when the cavity is sufficiently large. For cavities 40 μm or larger, a depressurization of 13 kPa is required for activation. It is believed that this is due to vapor trapping considerations and will be discussed later.

The experiments were repeated with ethanol. None of the cavities were activated despite the application of very high levels of depressurization. Presumably, all of the cavities are flooded with ethanol.

5.5.3 Activation of an Array of Cylindrical Cavities in Pool Boiling

Incipience experiments with water on the silicon surface imbedded with cylindrical cavities, laid out as shown in Fig. 5.10, were also done in the pool boiling facility. The measured wall superheat required to activate the cavities is summarized in Fig. 5.14. Also shown in Fig. 5.14 are the predicted incipience wall superheats based on Eq. 5.1 and those predicted based on the Cornwell hypothesis (double the prediction from Eq. 5.1).

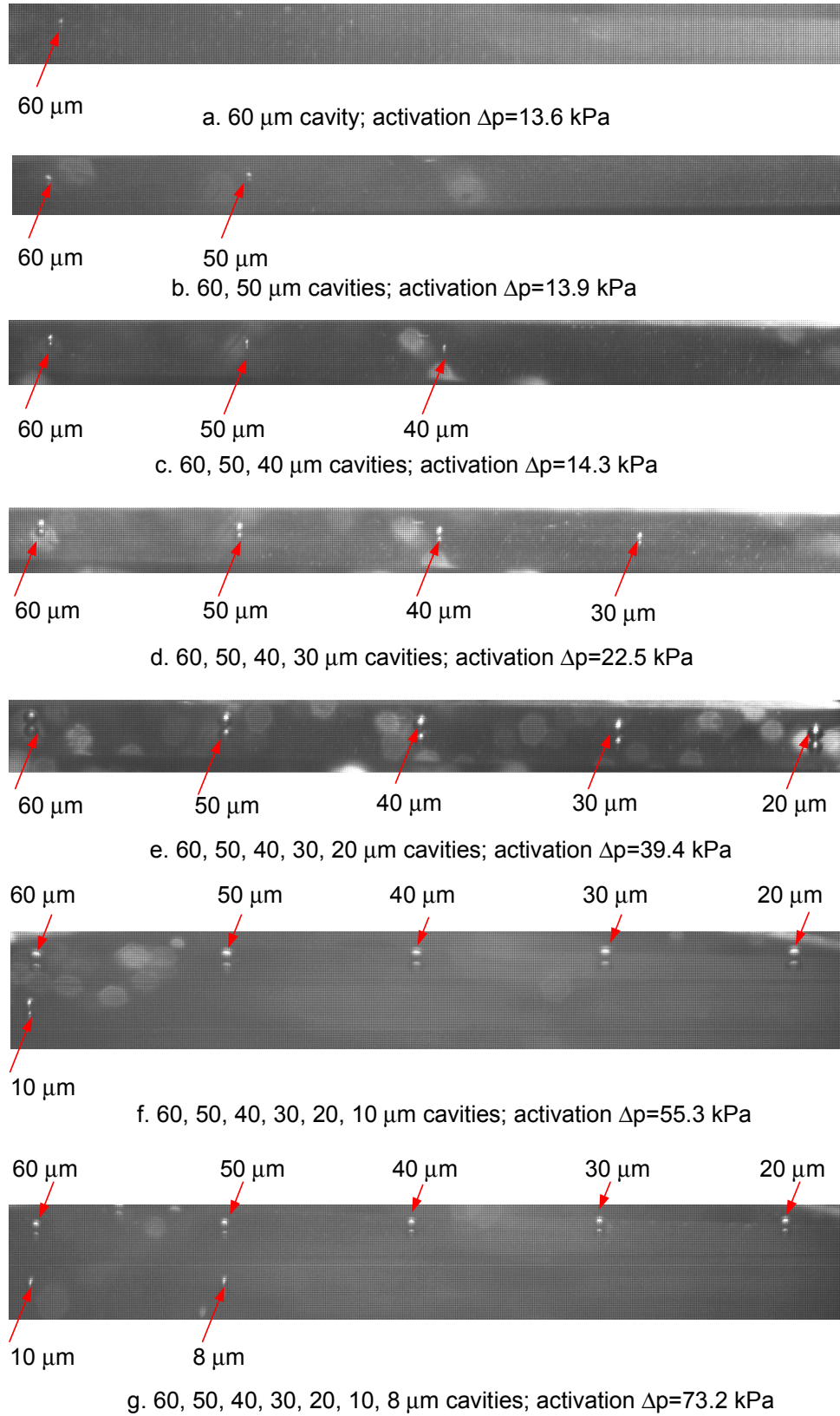


Figure 5.12. Typical images of bubble activation on cavities with different diameters.

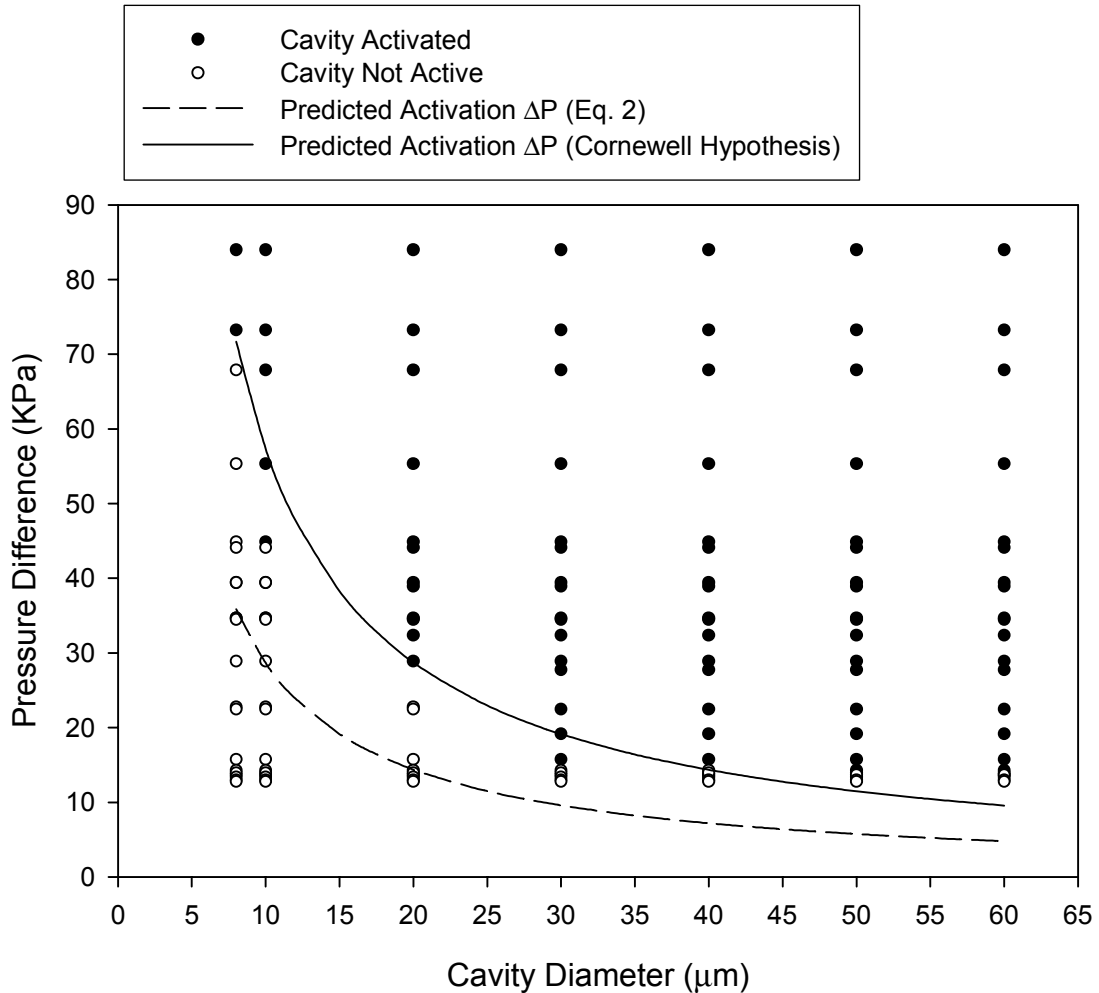


Figure 5.13. Comparison between measured and predicted gas bubble incipience.

Several observations are in order. The artificial cavities are not stable for boiling. It is observed that cavities are selectively active, depending on the magnitude of the wall superheat. The separation distance between adjacent cavities is 4 mm center-to-center and the bubble detachment diameters are on the order of 1 mm. Due to the large separation distance it is not expected that cavity-to-cavity thermal conductive interference is the cause for the site instability. During the boiling mode, there is significant ebullition around the periphery of the silicon test surface. This ebullition creates strong convective currents that sweep across the silicon surface, and it is likely that these strong convective

currents act to suppress incipience at some of the cavities as the thermal boundary layer is thinned.

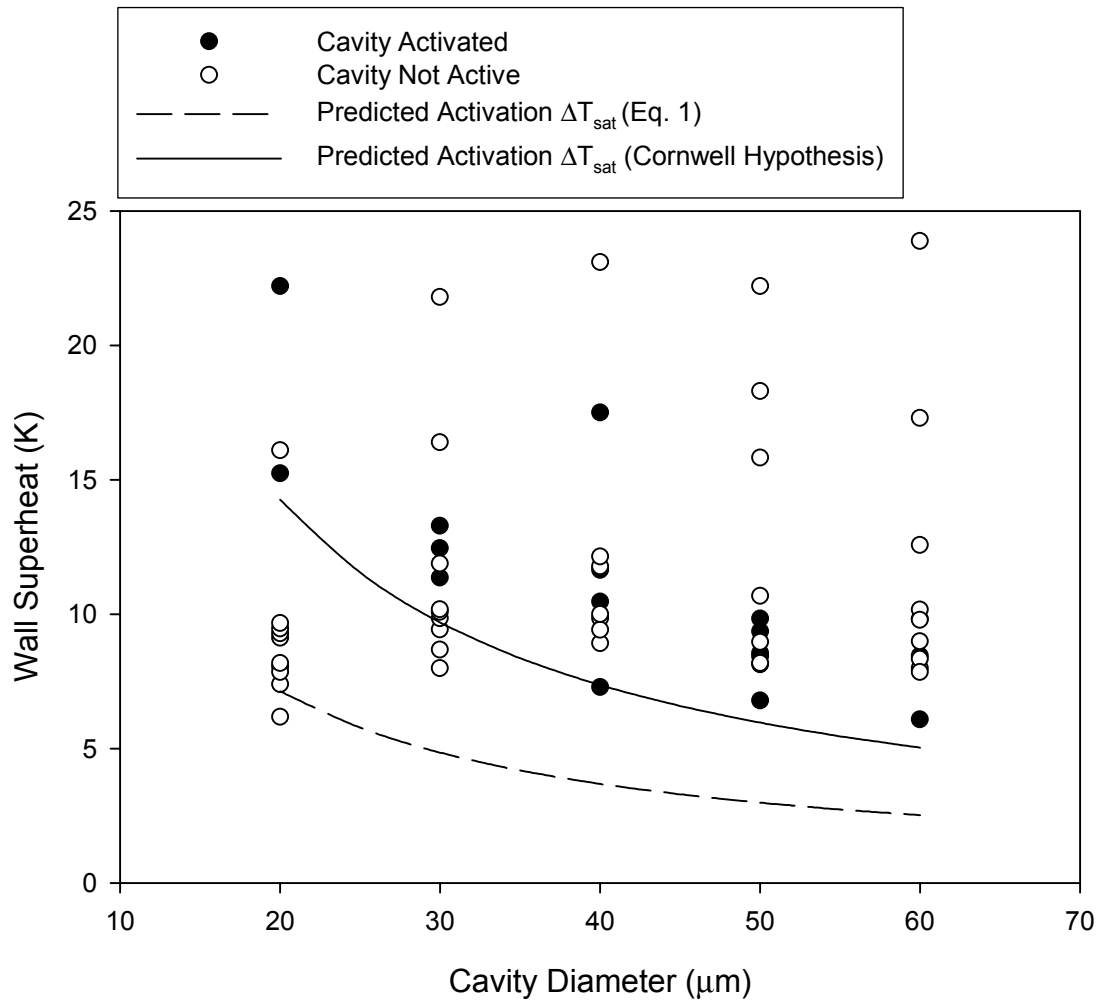


Figure 5.14. Comparison between measured and predicted boiling incipience.

It is also observed the minimum superheat required to activate the artificial cavities agrees reasonably well with the superheat calculated based on the Cornwell hypothesis, giving further credence to the supposition that the meniscus that resides within the cavities is concave. The agreement in the measured incipience criteria using gas nucleation and pool boiling, suggests that gas nucleation experiments are useful for studying incipience criteria. However, the instability of active cavities observed during

pool boiling suggests that gas nucleation is not very useful to study nucleation site density.

The pool boiling experiments were repeated with ethanol on the silicon surface. The wall superheat of the surface was gradually raised near 60 °C, and no ebullition was observed from the cavities. Eventually, the silicon surface delaminated from the brass heater and cracked; no more experiments were possible. These results are consistent with the gas nucleation experiments, where none of the cavities were activated, presumably due to flooding. In contrast, Qi and Klausner (2004) recently reported that a highly polished brass surface without any vapor trapping cavities, efficiently produced nucleation sites during pool boiling with a wall superheat as low as 10°C. In this study, the ethanol pool boiling experiments were repeated on a smooth silicon surface with no vapor trapping cavities. The wall superheat was gradually raised, and when it reached 60°C several nucleation sites formed on the surface.

5.5.4 Gas Nucleation Experiments with a Cavity Matrix

A silicon surface was prepared in which a 10 x 10 matrix of cylindrical cavities was etched into the silicon. All the cavities are separated by a distance of 2 mm in the transverse and longitudinal directions and have a uniform diameter of 10 µm and depth of 45 µm. With water covering the silicon surface, a depressurization of 73 kPa activates nearly all of the 100 cavities on the surface as shown in Fig. 5.15. This test provides additional evidence of the stability of bubble producing cavities using gas nucleation incipience.

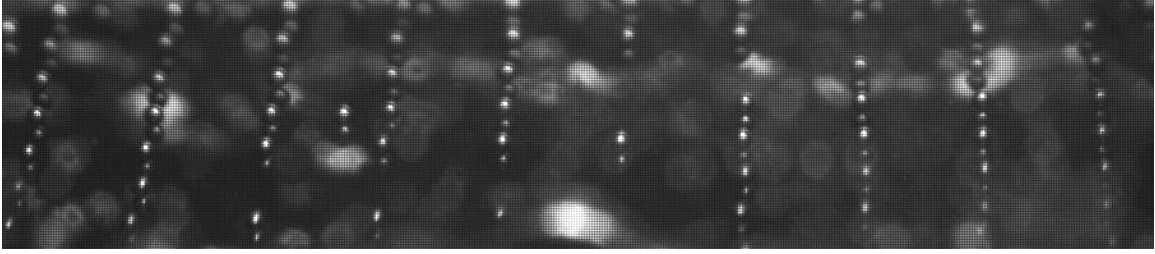
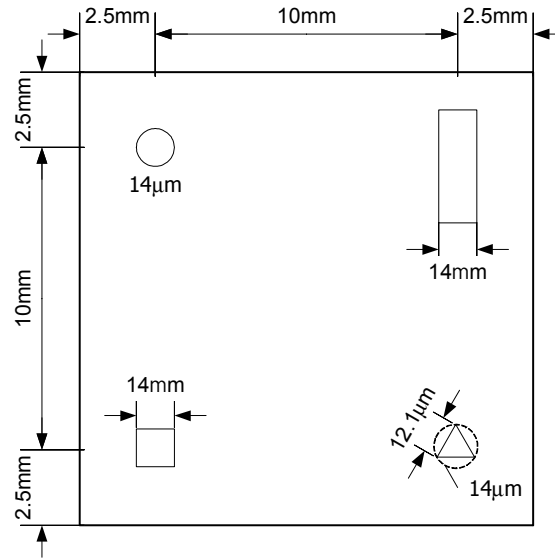


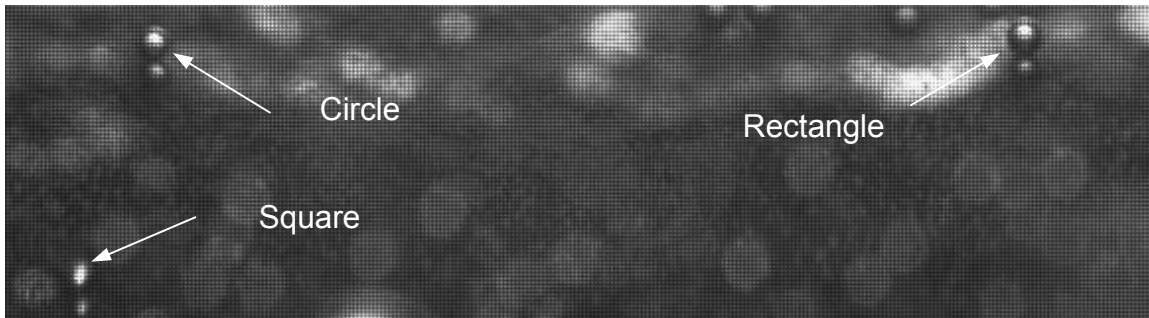
Figure 5.15. Gas bubble activation on a 10×10 matrix of $10 \mu\text{m}$ cylindrical cavities.

5.5.5 Activation of Different Shape Cavities Using Gas Nucleation

A silicon surface was prepared in which four different shaped cavities were placed adjacent to one another, separated by a distance $10 \mu\text{m}$ as shown in Fig. 5.16a. Also shown in Fig. 5.16a is the size of the cavities relative to the cylindrical cavity, which has a diameter of $14 \mu\text{m}$. As shown, the cavities were designed so that the diameter of the cylindrical cavity, the width of the square cavity, the width of the rectangular cavity and the diameter of the circumscribed circle around the triangular cavity have the same dimension. All cavities have the same depth, $45 \mu\text{m}$. A series of experiments were done using water in the gas nucleation facility with different magnitudes of depressurization. A typical image of bubble activation is shown in Fig. 5.16b, where the triangular cavity is not activated. The results are summarized in Fig. 5.17. As shown, the cylindrical, rectangular, and square cavity all activate at the same depressurization. The triangular cavity requires almost twice the depressurization to activate than the others since the meniscus curvature formed in the triangular cavity is smaller than the others. The fact that the rectangular cavity activates at the same depressurization as the cylindrical cavity suggests that the meniscus radius of curvature is governed by the width of the rectangular cavity. Thus when scratches on surfaces serve as potential nucleation sites, the appropriate length scale to consider for activation is the width.



(a)



(b)

Figure 5.16. Gas bubble activation on cavities with different shapes.

5.6 Discussion

Incipience experiments with precisely manufactured artificial cavities reveal that the wall superheat and depressurization typically required to activate vapor trapping

cavities respectively are $\Delta T_{sat} = \frac{4\sigma T_{sat}}{\rho_v h_{fg} r}$ and $\Delta P = \frac{4\sigma}{r}$, respectively. This result is

consistent with the hypothesis of Cornwell that a concave meniscus, as shown in Fig. 5.2a, is the most stable configuration within a vapor trapping cavity. As a matter of fact,

Kosky's (1968) study provides evidence that large pressure fluctuations are present during boiling, and are sufficient to push the meniscus into the cavity to form a concave shape. However, as vapor trapping cavities increase in size, there exists a threshold superheat or depressurization needed to activate a cavity, as observed in Fig. 5.13. In order to offer an explanation for this and other observed phenomena, it is necessary to consider the mechanics of vapor trapping.

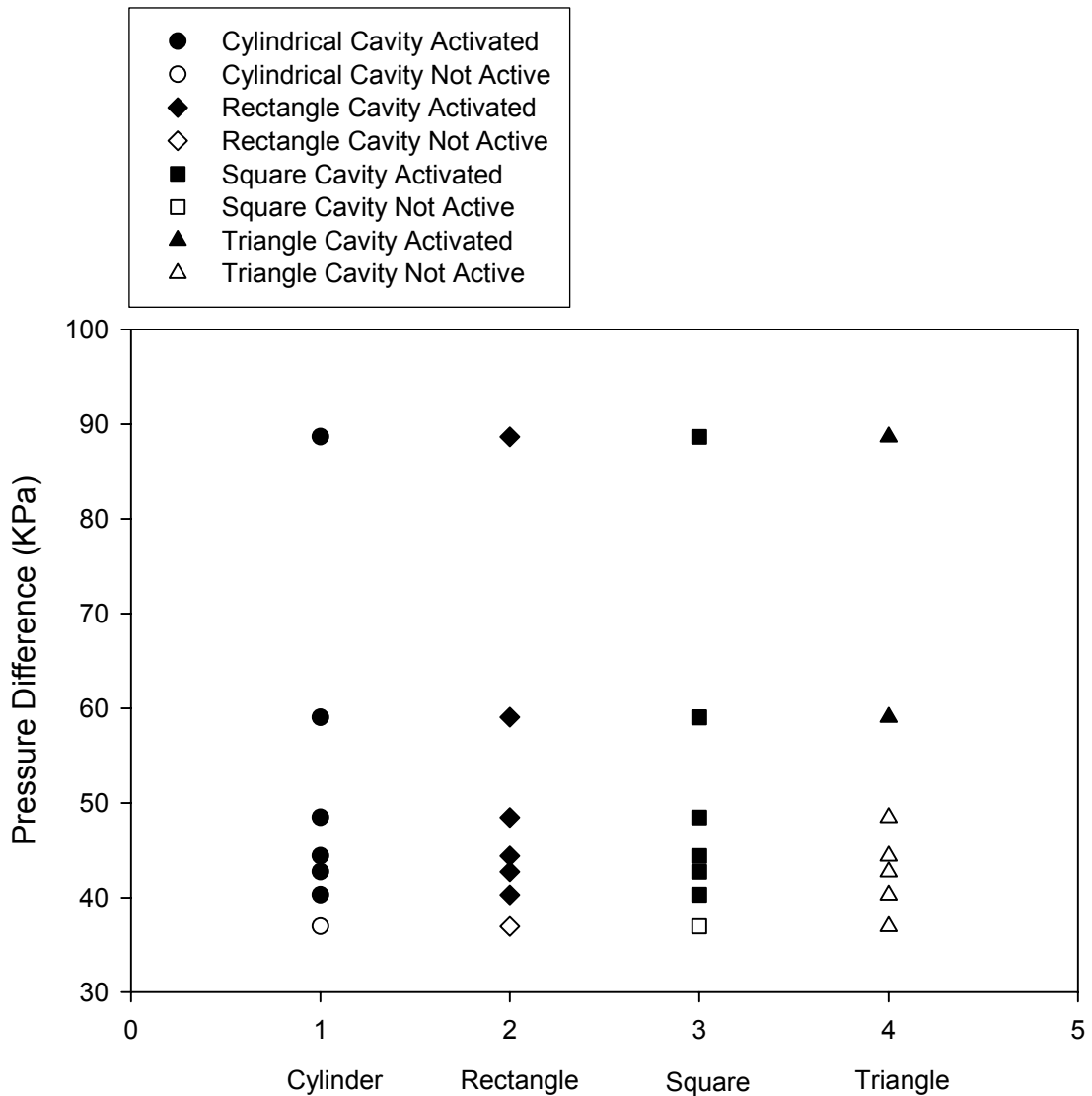


Figure 5.17. The influence of cavity shape on gas bubble activation.

There are currently two theories to describe the mechanism of vapor entrapment. Bankoff (1958) proposed a vapor trapping criterion based on the incomplete displacement of gas from the cavity by an advancing liquid front. Wang and Dhir (1993) developed a criterion based on equilibrium considerations and concluded that the liquid solid contact angle must be larger than the cavity mouth angle in order for a cavity to trap the vapor. For a cylindrical cavity, the cavity mouth angle is 90° . The water/silicon contact angle is only 21° , yet the cylindrical cavities considered in this study clearly trap vapor. In order to explain vapor trapping in cylindrical cavities, consideration is first given to Case I, where an advancing liquid front spreads over a cavity with a small diameter to depth ratio as shown in Fig. 5.18a. Using a quasi-static model, the liquid front creeps along with no inertia and follows the path shown in Fig. 5.18a. Based on geometrical considerations, such a cavity will always trap vapor when $\theta \geq \tan^{-1}\left(\frac{D}{H_{cav}}\right)$, where θ is the liquid/solid contact angle, D is the cavity mouth diameter and H_{cav} is the cavity height. For a cavity depth of $45 \mu\text{m}$ and water/silicon contact angle of 21° , according to the above criterion, any cylindrical cavity with a mouth diameter less than $17 \mu\text{m}$ will trap vapor. This threshold is consistent with the experimental observation in Fig. 5.13 where the predicted depressurization agrees with the measured data with cavity sizes below $20 \mu\text{m}$. Cylindrical cavities with a large diameter to depth ratio which do not satisfy the above vapor trapping criterion will flood, shown as case III in Fig. 5.18c. In reality, wetting and vapor trapping are dynamic processes, and the liquid inertia of the wetting front can be important. When consideration is given to an advancing liquid front with inertia over a cylindrical cavity with a moderate diameter to depth ratio, it is likely

that the liquid front will overshoot the back side of the cavity and trap vapor in a crevice, shown as case II in Fig. 5.18b. For such a case, the radius of curvature of the meniscus formed in the cavity depends on the amount of vapor trapped and is smaller than that of the mouth cavity radius. Also, the amount of vapor trapped will depend on the liquid inertia and not the cavity size. This is the reason the amount of depressurization required to activate cavities greater than 40 μm is the same and is more than that predicted when it is assumed the meniscus radius of curvature equals the cavity mouth radius. Clark et al. (1959) observed that scratches on heating surfaces make very efficient nucleation sites. The fact that cavities with a rectangular cross section are capable of trapping pockets of vapor as depicted in Fig. 5.18b offers a plausible explanation for their observation.

Nucleation site instability has been observed with pool boiling on the silicon surface with an array of cylindrical cavities as is evident in Fig. 5.14. Hsu (1962) identified both a minimum and maximum cavity radius that will permit the incipience of vapor bubbles, depending on the thickness of the liquid thermal boundary layer surrounding the vapor embryo. A thinning thermal boundary layer reduces the maximum cavity diameter that will permit an active nucleation site. As observed in Fig. 5.14, as the wall superheat increases, the size of active cavities decreases, which is consistent with thermal boundary layer thinning. At the interface between the brass heater and silicon test surface, significant ebullition was observed with increasing superheat. Strong convective currents, which sweep across the silicon surface were observed, which result in thermal boundary layer thinning. This leads to deactivation of the larger cylindrical cavities on the test surface, as was observed.

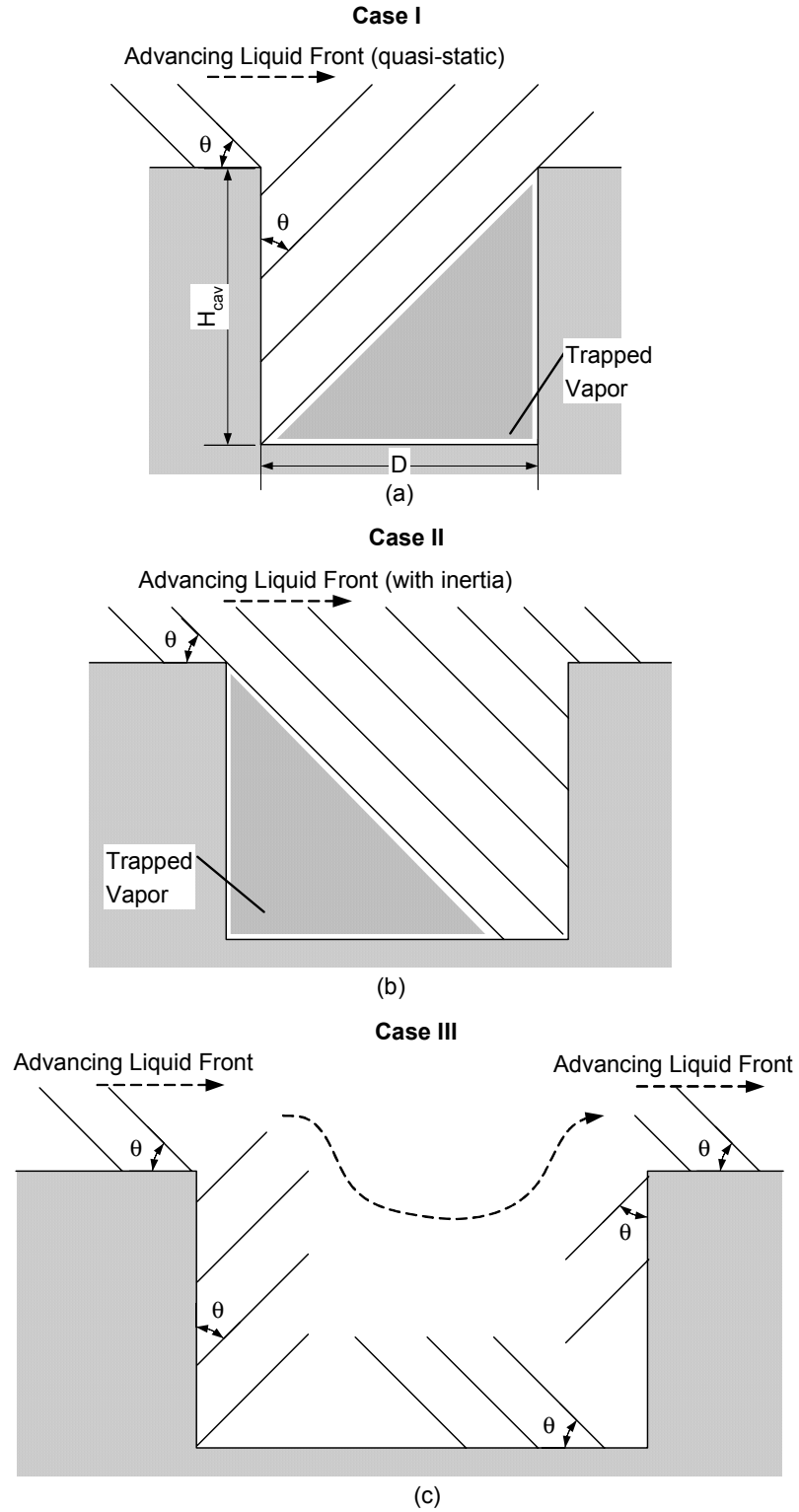


Figure 5.18. Vapor trapping mechanism in cylindrical cavities.

Lastly, the observations of Pesse et al. (2004) suggest that even though a cavity is efficient at trapping gas, it will eventually flood due to diffusion given enough time. The implication is that the wetting history of the heating surface may be important in incipience considerations.

5.7 Summary

A detailed experimental investigation of heterogeneous nucleation with artificial cavities has been presented. The results are summarized as follows:

(1) The incipient depressurization or wall superheat required for activating vapor trapping cavities is twice that predicted from the Griffith and Wallis model. The result is consistent with a concave meniscus residing within a vapor trapping cavity as was proposed by Cornwell.

(2) Vapor trapping cavities are stable, with no site interaction, when activated using gas nucleation depressurization. They are not stable during boiling, and the larger cavities are suppressed with boundary layer thinning, which occurs with increasing superheat.

(3) Vapor trapping mechanisms have been proposed for cylindrical cavities, and a vapor trapping criterion has been introduced based on a creeping wetting front.

(4) Square and rectangle cavities with a width equal to the diameter of a cylindrical cavity require the same incipient depressurization for activation as the cylindrical cavity.

(5) From experimental observation, the backpressure exerted during gas nucleation does not influence the incipience as long as the magnitude of the depressurization is fixed.

(6) All artificial cavities flooded with ethanol covering the surface. An incipient superheat of 60°C was required to activate nucleation sites on a smooth silicon surface.

CHAPTER 6 CONCLUSIONS AND RECOMMENDATIONS

An experimental investigation of nucleation site density has been presented using a gas nucleation technique and pool boiling over a large parameter space. The fluids used for this study, distilled water and ethanol, are moderately wetting and highly wetting, respectively. The surfaces used in this study include roughly polished brass and stainless steel surfaces, mirror-like brass surfaces, and a silicon chip with artificial cavities. The major accomplishments of this study and recommendations for future study are summarized

6.1 Accomplishments and Findings

The body of research presented has advanced the fundamental understanding of heterogeneous nucleation theory as follows.

1. The usefulness of the gas nucleation technique to assist in the prediction of pool nucleate boiling site density has been investigated. It has been observed that the nucleation site density is higher for gas nucleation than for pool boiling although the trends of nucleation site density versus the inverse of the critical radius are similar for gas nucleation and pool boiling using water as the working fluid. These differences may be due to the thermal interference and wettability. Underneath a growing bubble the energy is depleted from the heater substrate and thus suppresses the formation of neighboring nucleation sites. The difference in wettability will also intensify the difference of nucleation site density. In gas nucleation experiments the gas phase is air while vapor is presented in pool boiling experiments although the same liquid/solid combination is used.

In conclusion, it is not currently possible to predict nucleation site density in pool boiling from gas nucleation experiments.

2. The usefulness of statistical models to predict nucleation site density on commercial surfaces has been examined. First, an algorithm for identifying potential cavities from topography data on commercial surfaces has been presented. After every peak in the x-z profile of the surface, achieved by interferometric scanning, is identified, the characteristic diameter and cone angle associated with the cavity which exists on either side of a peak are found by extending a line from the peak until it intersects the sidewall of a higher peak. A unique method has been presented to resolve the uncertainty when cavities reside inside a cavity. Second, a robust methodology for constructing surface structure statistical distributions has been explored. It was found that the size distribution of the cavities on the surfaces follows the Weibull distribution and the distribution of cavity half-cone angle has a fractal nature. Finally, the statistical model has been examined and compared with the experimental data from gas nucleation and pool boiling. Very good agreement both in gas nucleation and pool boiling is achieved for the brass surface using water. However, there is considerable error between the measurement and prediction for the stainless steel surface. One possible reason is that there is very large statistical uncertainty associated with the probability of cavity half-cone angles. From the probability distribution of cavity half-cone angle, it has been found that the frequency of cavities that can meet the vapor trapping criterion is very low. And thus the uncertainty will be large under the current sample size.

3. A significant finding in this study is that heterogeneous nucleation in boiling systems is not exclusively seeded by vapor trapping cavities. During the ethanol gas

nucleation experiments, it was found that few sites were activated even under very high depressurization. In contrast, nucleation sites could be easily activated during pool boiling. These unexpected results cast doubt on the vapor trapping theory in heterogeneous boiling nucleation since ethanol will flood most cavities on surfaces due to its high wettability. However, the large quantities of nucleation sites during pool boiling suggest that there exists some other mechanism. Tyrrell and Attard (2001) have observed very closely packed nanobubbles that cover a smooth surface. It is possible that there exist some nanobubbles with appropriate radius of curvature for nucleation since those observed nanobubbles are pancake shaped and closely packed.

4. This work is the first to systematically study the bubble incipience using precisely manufactured cavities. The incipient depressurization or wall superheat required for activating vapor-trapping cavities is twice that predicted from the Griffith and Wallis model. The incipience conditions observed for water using both gas nucleation and pool boiling support Cornwell's contact angle hysteresis theory for vapor trapping cavities. Using ethanol, cavities appeared to be completely flooded and were not activated using either gas nucleation or pool boiling. Using water and gas nucleation cavities were almost always activated, provided the incipience criterion was satisfied; in contrast cavities in pool boiling with water activated with different superheats during different experiments. The difference in incipience behavior between gas nucleation and pool boiling with water is explained based on vapor trapping and thermal suppression considerations. Using the gas nucleation technique, it has been observed that the backpressure does not influence bubble incipience, provided the pressure difference is the same. The experimental results presented affirm the theory of heterogeneous nucleation

from vapor trapping cavities provided contact angle hysteresis and vapor trapping are fully accounted for. However, the results also suggest that the theoretical considerations required for a deterministic model for incipience from vapor trapping cavities during boiling is more complex than previously hypothesized.

6.2 Recommendations for Future Research

The strong motivation for the present study is to understand the mechanisms of bubble nucleation with detailed surface topography. Several key issues remain unsolved although significant progress has been achieved through this work. In order to further develop the knowledge base of heterogeneous nucleation and seek reliable mechanistic boiling models, the following are recommended for future research:

1. The traditional vapor trapping theory in heterogeneous nucleation cannot explain the experimental observations in this study. The existence of nanobubbles offers a plausible mechanism for seeding nucleation sites. Yet, it still requires extensive further examination. Other mechanisms that can explain anomalous experimental observations should also be sought after.

2. Some limited success has been achieved using statistical models to predict the nucleation site density. The significant difference in nucleation site density between the brass and stainless steel surfaces in the gas nucleation experiments has not been adequately studied. Whether the parameters such as contact angle and cavity size are of controlling significance or whether surface chemistry is playing a very important role needs to be explored.

3. The fractal nature of the cavity geometry may have some utility in predicting the occurrence of vapor trapping cavities.

APPENDIX A
BRASS/WATER STATIC CONTACT ANGLE MEASUREMENTS

Baseline Length	Protrusion Height	Contact Angle
201.0	78.0	75.6
210.0	78.0	73.2
182.0	65.0	71.1
191.0	69.0	71.7
209.0	71.0	68.4
241.0	93.0	75.3
223.0	87.0	75.9
268.0	94.0	70.1
328.0	111.0	68.2
360.0	123.0	68.7
210.0	85.0	78.0
213.0	81.0	74.5
170.0	70.0	78.9
Contact Angle Average (°C)		73.1
Standard Deviation		3.7

Note: The baseline length and protrusion height of water drop are measured in Sigmascan software environment. So the unit is pixel that cannot represent the actual dimension. However, it is not a problem in this case because these two variables appear at numerator and denominator positions.

APPENDIX B
STAINLESS STEEL/WATER STATIC CONTACT ANGLE MEASUREMENTS

Baseline Length	Protrusion Height	Contact Angle
147.0	57.0	75.6
125.0	51.0	78.4
129.0	57.0	82.9
163.0	58.0	70.9
254.0	94.0	73.0
136.0	56.0	78.9
114.0	49.0	81.4
141.0	57.0	77.9
98.0	43.0	82.5
103.0	43.0	79.7
102.0	44.0	81.6
109.0	43.0	76.5
130.0	49.0	74.0
Contact Angle Average (°C)		77.4
Standard Deviation		4.2

APPENDIX C CAVITY MEASUREMENTS

The cylindrical cavities, manufactured on a 500 μm thick silicon substrate, have been measured using a Wyko NT 1000 interferometer. The following are the features of artificial cavities with nominal diameters ranging from 20 μm to 50 μm .

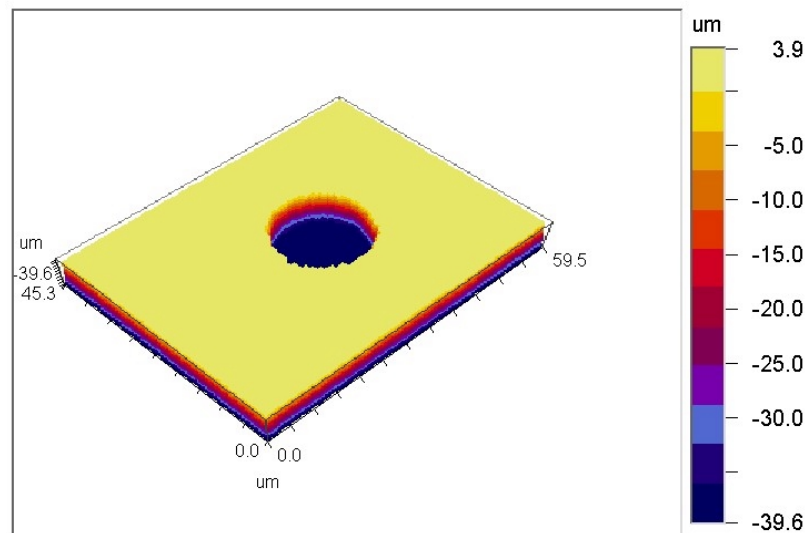


Fig. 1a. Three-dimensional profile of cylindrical cavity with 20 μm nominal mouth diameter.

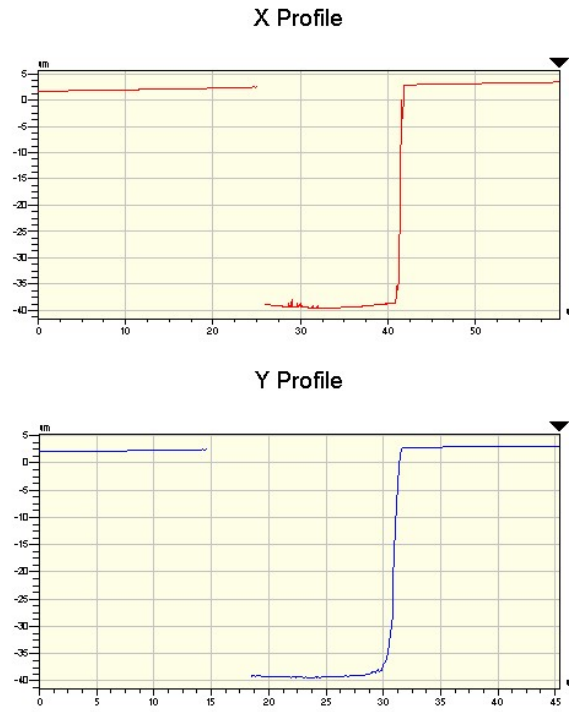


Fig. 1b. 2-D measurement of cylindrical cavity with 20 μm nominal mouth diameter.

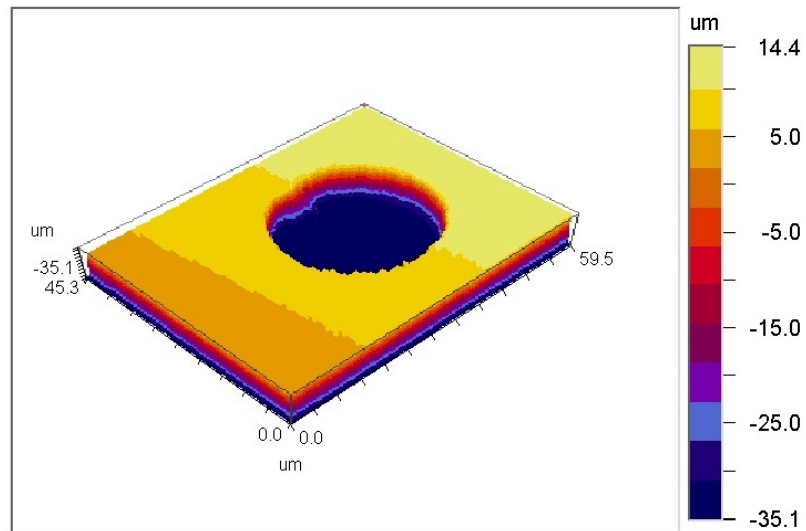


Fig. 2a. Three-dimensional profile of cylindrical cavity with 30 μm nominal mouth diameter.

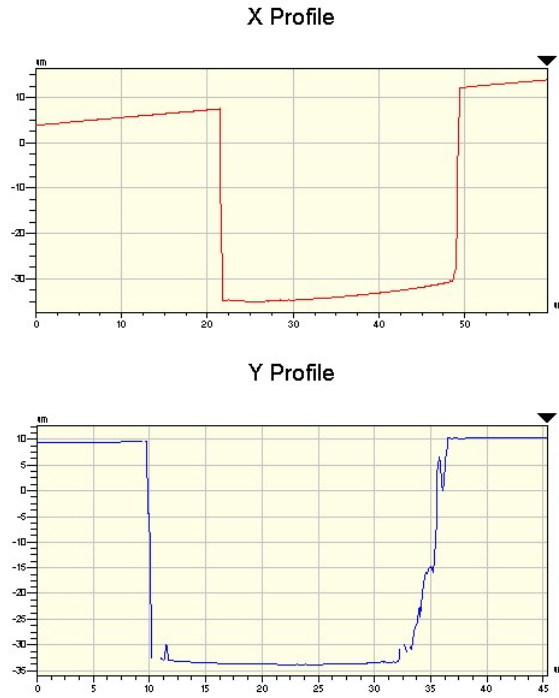


Fig. 1b. 2-D measurement of cylindrical cavity with 30 μm nominal mouth diameter.

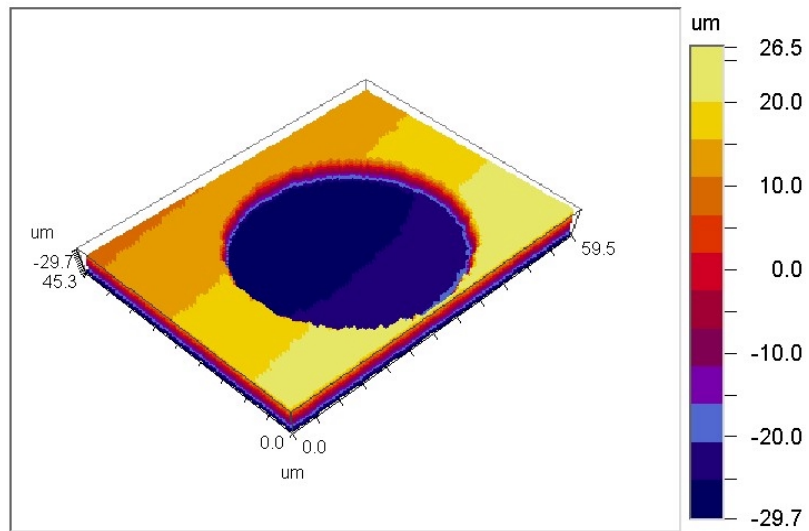


Fig. 3a. Three-dimensional profile of cylindrical cavity with 40 μm nominal mouth diameter.

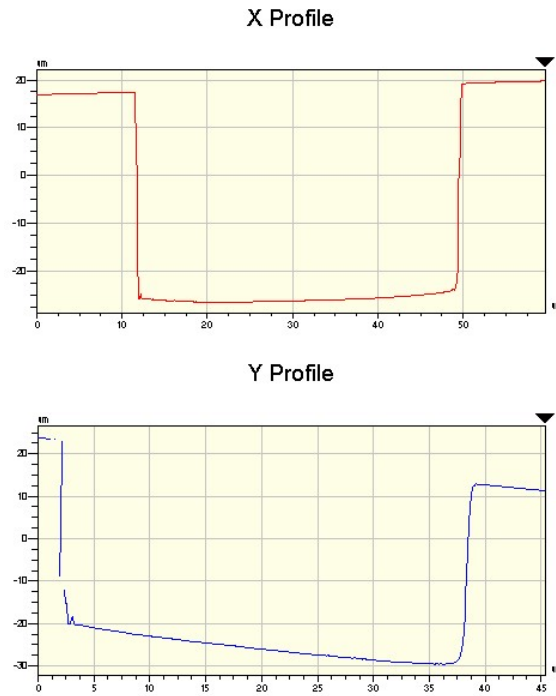


Fig. 1b. 2-D measurement of cylindrical cavity with 40 μm nominal mouth diameter.

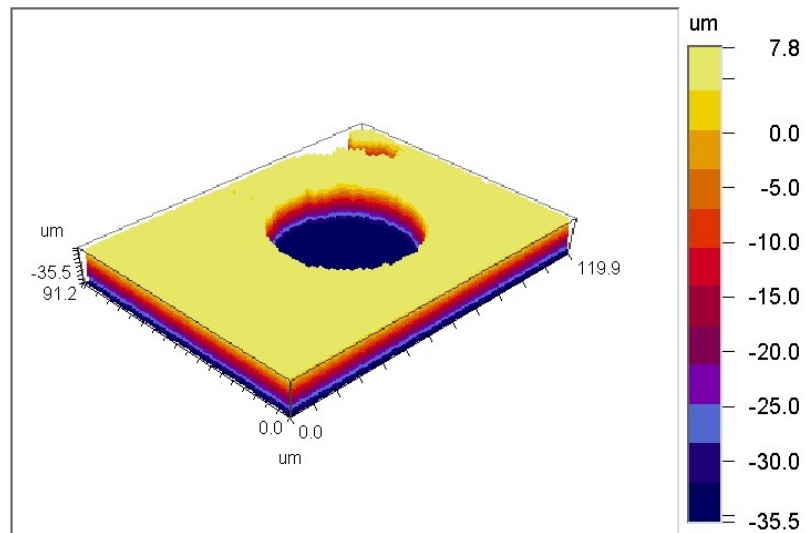


Fig. 4a. Three-dimensional profile of cylindrical cavity with 20 μm nominal mouth diameter.

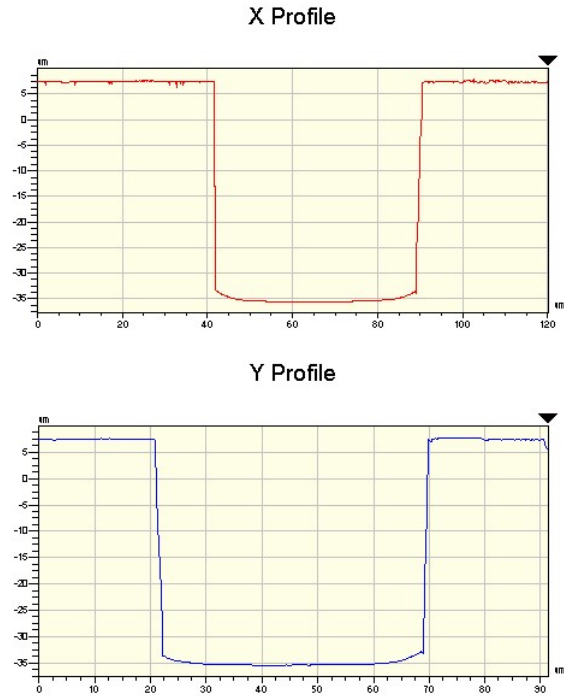


Fig. 1b. 2-D measurement of cylindrical cavity with 50 μm nominal mouth diameter.

APPENDIX D
LIQUID PROPERTIES AND POOL BOILING DATA

The pool boiling data discussed in Chapter 3 are included in this appendix. Bulk liquid temperature is the average of three measurements. Heating surface temperature is obtained from the measured temperature gradient.

Thermophysical Properties of Saturated Water and Ethanol							
		Temp. T (K)	Pressure, P (kPa)	Specific Volume (m ³ /kg) v _g (vapor)	v _f 10 ³ (liquid)	Latent Heat h _{fg} (kJ/kg)	Surf. Tension σ _f 10 ³ (N/m)
Water	T _{room}	298.15	5.083	43.87	1.003	2442	72.1
	T _{boiling}	373.15	101.33	1.679	1.044	2257	58.9
Ethanol	T _{room}	298.15	7.9	7.912	1.240	1025	21.9
	T _{boiling}	351	101.33	0.6944	1.321	846.0	17.1

Brass/Water Pool Boiling Data						
Liquid Temp. (°C)	Surface Temp. (°C)	Superheat (°C)	Heat flux (W/m ²)	Bubble number	n/A (cm ⁻²)	
Increasing heat flux						
100.46	105.05	4.59	21586.26			
101.58	110.43	8.85	39778.23			
101.61	110.82	9.21	51360.93	9	1.78	
101.63	111.75	10.12	58823.10	11	2.17	
101.60	111.83	10.23	69267.26	22	4.34	
101.33	111.38	10.05	67549.59	22	4.34	
101.72	112.01	10.29	84434.72	24	4.74	
101.79	112.50	10.71	96809.63	34	6.71	
101.77	113.10	11.32	118610.87	38	7.50	
101.78	113.43	11.65	140450.80			
Decreasing heat flux						
101.84	113.21	11.38	124361.03			
101.89	112.63	10.73	98532.62	33	6.51	
101.97	112.65	10.68	83851.59	25	4.93	
102.06	112.59	10.53	70440.03	21	4.14	
101.95	112.20	10.25	59594.70	15	2.96	
101.85	111.38	9.53	49162.17	12	2.37	
101.93	110.95	9.02	39372.47	11	2.17	
101.86	106.16	4.30	21663.27	1	0.20	

Brass/Ethanol Pool Boiling Data					
Liquid Temp. (°C)	Surface Temp. (°C)	Superheat (°C)	Heat flux (W/m ²)	Bubble number	n/A (cm ⁻²)
Increasing heat flux					
78.93	80.23	1.30	7616.27		
78.86	87.58	8.72	15669.09		
78.70	89.19	10.49	17546.02	1.00	0.20
78.71	90.89	12.18	19679.29	3.00	0.59
78.89	92.64	13.76	22458.01	13.00	2.57
78.60	92.46	13.86	25507.45	15.00	2.96
78.91	93.19	14.28	26153.79	20.00	3.95
78.44	92.67	14.23	28271.55	25.00	4.93
78.34	93.31	14.97	36887.03	46.00	9.08
78.83	93.42	14.59	35623.29		
78.90	93.71	14.81	44517.55		
78.75	93.83	15.08	54574.37		
78.16	93.56	15.39	67540.25		
Decreasing heat flux					
79.25	91.85	12.60	22867.92	5.00	0.99
78.67	91.98	13.30	25227.63	17.00	3.35
78.79	92.32	13.53	27027.98	20.00	3.95
78.18	92.38	14.20	32984.83		
78.70	93.14	14.44	35978.48	37.00	7.30
78.61	93.22	14.61	40822.76	48.00	9.47
78.72	93.86	15.15	43705.96		
79.22	94.41	15.19	55913.45		
78.73	93.75	15.02	46575.14		
78.34	93.70	15.36	67641.54		
78.38	93.78	15.40	77185.17		
78.17	93.73	15.56	108614.10		

Mirror-finish brass/Ethanol Pool Boiling Data					
Liquid Temp. (°C)	Surface Temp. (°C)	Superheat (°C)	Heat flux (W/m ²)	Bubble number	n/A (cm ⁻²)
Increasing heat flux					
77.59	78.51	0.92	10151.40	1.00	0.20
78.74	90.95	12.21	22299.07	8.00	1.58
78.44	91.77	13.33	28094.70	25.00	4.93
78.76	92.77	14.01	37135.34	38.00	7.50
79.16	93.38	14.22	44877.83		
Decreasing heat flux					
78.91	86.57	7.66	13235.92		
79.08	89.98	10.90	16989.46		
79.80	92.11	12.31	20244.97	1.00	0.20
78.88	91.96	13.09	24440.78	6.00	1.18
79.15	92.89	13.74	31987.07	24.00	4.74
79.27	93.28	14.01	38847.03	32.00	6.32
79.74	93.59	13.85	38192.42		

Stainless steel/Water Pool Boiling Data					
Liquid Temp. (°C)	Surface Temp. (°C)	Superheat (°C)	Heat flux (W/m ²)	Bubble number	n/A (cm ⁻²)
Increasing heat flux					
101.12	101.54	0.42	4061.90		
101.12	105.56	4.44	8880.00		
100.21	105.47	5.26	10520.00		
99.34	106.47	7.13	12121.00		
99.92	110.63	10.71	22491.00		
100.54	114.81	14.27	24259.00		
100.08	114.68	14.60	32120.00	4.00	0.79
99.94	114.85	14.91	40257.00	11.00	2.17
100.57	116.57	16.00	49600.00	20.00	3.95
101.01	118.11	17.10	56430.00	25.00	4.93
101.45	119.46	18.01	63935.50	31.00	6.12
101.76	119.23	17.47	69880.00	38.00	7.50
Decreasing heat flux					
101.66	115.63	13.97	50292.00		
101.16	117.11	15.95	59015.00		
101.73	119.00	17.27	69080.00		

Stainless Steel/Ethanol Pool Boiling Data					
Liquid Temp. (°C)	Surface Temp. (°C)	Superheat (°C)	Heat flux (W/m ²)	Bubble number	n/A (cm ⁻²)
Increasing heat flux					
78.99	83.67	5.37	7220.00		
78.12	89.20	10.90	14515.00		
78.89	95.90	17.60	22745.00		
79.40	99.20	20.90	35050.00	13.00	2.57
79.40	99.17	20.87	45105.00	34.00	6.71
79.32	99.56	21.26	49722.50	40.00	7.89
Decreasing heat flux					
78.69	97.60	19.30	27487.50	2.00	0.39
78.87	98.78	20.48	32092.50	7.00	1.38

LIST OF REFERENCES

- Bankoff, S. G., 1958, Entrainment of gas in the spreading of liquid over a rough surface, *AIChE J.*, vol. 4, no. 1, pp. 24-26.
- Barthau, G., 1992, Active nucleation site density and pool boiling heat transfer--an experimental study, *Int. J. Heat Mass Transfer*, vol. 35, no. 2, pp. 271-278.
- Benjamin, R. J., Balakrishnan, A. R., 1997, Nucleation site density in pool boiling of saturated pure liquids: effect of surface microroughness and surface and liquid physical properties, *Experimental Thermal and Fluid Science*, Vol.15, pp. 32-42.
- Bergez, W., 1995, Nucleate boiling on a thin heating plate: heat transfer and bubbling activity of nucleation sites, *Int. J. Heat Mass Transfer*, Vol. 38, No. 10, pp. 1799-1811.
- Bier, K., Gorenflo, D., Salem, M. I., Tanes, Y. M., 1978, Pool boiling heat transfer and size of active nucleation centers for horizontal plates with different roughness, *Proc. 6th Int. Heat Transfer Conf.*, Toronto, vol. 1, pp. 151-156.
- Brauer, H., Mayinger, F., 1992, Onset of nucleate boiling and hysteresis effects under forced convection and pool boiling, *Pool and External Flow Boiling*, ASME, pp. 15-35.
- Brown, W. T., 1967, Study of flow surface boiling, PhD Thesis, Department of Mechanical Engineering, Massachusetts Institute of Technology, Cambridge, MA.
- Bury, K., 1999, Statistical distributions in engineering, New York, Cambridge University Press, pp. 311-341.
- Calka, A., Judd, R. L., 1985, Some aspects of the interaction among nucleation sites during saturated nucleate boiling, *Int. J. Heat Mass Transfer*, vol. 28, no. 12, pp. 2331-2342.
- Chatpun, S., Watanabe, M., Shoji, M., 2004, Nucleation site interaction in pool nucleate boiling on a heated surface with triple artificial cavities, *Int. J. Heat Mass Transfer*, vol. 47, no. 14, pp.3583-3587.
- Clark, H. B., Strenge, P. S., Westwater, J. W., 1959, Active sites for nucleate boiling, *Chem. Eng. Prog. Symp. Series*, vol. 55, no. 29, pp. 103-110.

- Cornwell, K., 1977, Naturally formed boiling site cavities, Letters in Heat and Mass Transfer, vol. 4, pp. 63-72.
- Cornwell, K., 1982, On boiling incipience due to contact angle hysteresis, Int. J. Heat Mass Transfer, 25, pp. 205-211.
- Corty, C., Foust, A., 1955, Surface variables in nucleate boiling, Chem. Eng. Prog. Symp. Series, vol. 17, no. 51, pp. 1-12.
- Eddington, R. I., Kenning, D. B. R., 1978, The prediction of flow boiling bubble populations from gas bubble nucleation experiments, Proc. 6th Int. Heat Transfer Conf., vol. 1, pp. 275-280.
- Eddington, R. I., Kenning, D. B. R., Korneichev, A. I., 1978, Comparison of gas and vapor bubble nucleation on a brass surface in water, Int. J. Heat Mass Transfer, vol. 21, pp. 855-862.
- Eddington, R. I., Kenning, D. B. R., 1979, The effect of contact angle on bubble nucleation, Int. J. Heat Mass Transfer, vol. 22, pp. 1231-1236.
- Gaertner, R. F., 1963, Distribution of active sites in the nucleate boiling of liquid, Chemical Engineering Progress Symposium Series, Heat transfer – Houston, No. 41, Vol. 59, pp. 52-61.
- Gaertner, R. F., 1965, Photographic study of nucleate pool boiling on a horizontal surface, J. Heat Transfer, pp. 17-29.
- Gaertner, R. F., Westwater, J. W., 1960, Population of active sites in nucleate boiling heat transfer, Chem. Eng. Prog. Symp. Series, vol. 56, no. 30, pp. 39-48.
- Gjerkes, H., Golobic, I., 2002, Measurement of certain parameters influencing activity of nucleation sites in pool boiling, Experimental Thermal and Fluid Sciences 25, pp. 487-493.
- Golobic, I., Pavlovic, E., Strgar, S., Kenning, D. B. R., Yan, Y. Y., 1996, Wall temperature variations during bubble growth on a thin plate: computations and experimentations, Eurotherm Sem. no. 48, Paderborn, ETS, Pisa, pp. 25-32.
- Gorenflo, D., Luke, A., Danger, E., 1998, Interactions between heat transfer and bubble formation in nucleate boiling, Heat Transfer 1998, Proceedings of 11th IHTC, vol. 1, Korea, pp. 149-174.
- Griffith, P., Wallis, J.D., 1960, The role of surface conditions in nucleate boiling, Chemical Engineering Progress Symposium Series, no. 30, vol. 56, pp. 49-63.
- Heled, Y., Ricklis, J., Orell, A., 1970, Pool boiling from large arrays of artificial nucleation sites, Int. J. Heat Mass Transfer, vol. 13, pp. 503-516.

- Hsu, Y. Y., 1962, On the size range of active nucleation cavities on a heating surface, *J. Heat Transfer*, vol. 98c, pp. 207-216.
- Ishida, N., Inoue, T., Miyahara, M., Higashitani, K., 2000, Nano bubbles on a hydrophobic surface in water observed by tapping-mode atomic force microscopy, *Langmuir*, 16, pp. 6377-6380.
- Kenning, D. B. R. 2000, Experimental methods: looking closely at bubble nucleation, *Engineering Foundation Conference Boiling 2000*, Keynote Lecture.
- Kenning, D. B. R., Del Valle, V. H., 1981, Fully-developed nucleate boiling: overlap of areas of influence and interference between bubble sites, *Int. J. Heat Mass Transfer*, vol. 24, no. 6, pp. 1025-1032.
- Kenning, D. B. R., Yan, Y.Y., 1996, Pool boiling heat transfer on a thin plate: features revealed by liquid crystal thermography, *Int. J. Heat Mass Transfer*, vol. 39, pp. 3117-3137.
- Kosky, P. G., 1968, Nucleation site instability in nucleate boiling, *Int. J. Heat Mass Transfer*, vol. 11, pp. 929-932.
- Kurihara, H. M., Myers, J. E., 1960, The effects of superheat and surface roughness on boiling coefficients, *AIChE J.*, vol. 6, no. 1, pp. 83-91.
- Lorenz, J. J., Mikic, B. B., Rohsenow, W. M., 1974, Effect of surface conditions on boiling characteristics, *Proc. 5th Int. Heat Transfer Conf.*, Tokyo, pp.35-39.
- Luke, A., 1997, Pool boiling heat transfer from horizontal tubes with different surface roughness, *Int. J. Refrig.*, Vol. 20, No. 8, pp. 561-574.
- Luke, A., Baumhoger, E., Scheunemann, P., 2000, 3-dimensional description of the microstructure of heated surfaces in nucleate pool boiling, *Multiphase Science and Technology*, Vol. 12, Nos. 3 &4, pp. 17-29.
- Luke, A., Gorenflo, D., 1999, Nucleate boiling heat transfer of HFCs and HCs in heat pump application: state of the art and new developments, *6th IEA Heat Pump Conference*, Berlin.
- Luke, A., Gorenflo, D., 2000, Heat transfer and size distribution of active nucleation sites in boiling propane outside a tube, *Int. J. Therm. Sci.*, vol.39, pp. 919-930.
- Luke, A., Runowski, T., 1997, Heat transfer and size distribution of active nucleation sites in boiling of hydrocarbons, *Proc. Int. Conf. Convect. Flow & Pool Boil.*, Irsee, Engineering Foundation Publication, pp.89-96.
- Mark, H., Othmer, D., Overberger, C., Seaborg, G., 1978, *Encyclopedia of chemical technology*, Third Edition, Vol. 9, New York, John Wiley & Sons, pp. 338-373.

- Menz, W., Mohr, J., Paul, O., 2001, *Microsystem technology*, Weinheim, Wiley-VCH, pp. 171-208.
- Messina, A. D., Park, E. L., 1981, Effects of precise arrays of pits on nucleate boiling, *J. Heat Transfer*, vol. 24, pp. 141-145.
- Mikic, B. B., Rohsenow, W. M., 1969, A new correlation of pool-boiling data including the effect of heating surface characteristics, *Transactions of the ASME. Series C, J. Heat Transfer*, Volume 91, Issue 2, pp. 245-250.
- Miller, I., 1977, *Probability and statistics for engineers*, New Jersey, Prentice-Hall Inc., pp. 121-123.
- Mizukami, K., Furutani, H., Abe, F., Mukasa, S., 1998, Boiling inception on platinum surface in water and in ethanol, *Heat Transfer 1998, Proceedings of 11th IHTC*, Vol. 2, Kyongju, Korea, pp. 461-466.
- Pasamehmetoglu, K. O., Nelson, R. A., 1991, Cavity-to-cavity interaction in nucleate boiling: the effect of heat conduction within the heater, *AIChE Symp. Series*, vol. 87, no. 283, pp. 342-351.
- Pasamehmetoglu, K. O., Chappidi, P. R., Unal, C., Nelson, R. A., 1993, Saturated pool nucleate boiling mechanisms at high heat fluxes, *Int. J. Heat Mass Transfer*, vol. 36, pp. 3859-3868.
- Pesse, A. V., Warriar, G. R., Dhir, V. K., 2004, Experimental study of the gas entrapment process in close-end microchannels, 2004 ASME International Mechanical Engineering Congress, Anaheim, CA, USA.
- Preckshot, G. W., Denny, V. E., 1967, Explorations of surface and cavity properties on the nucleation boiling of carbon tetrachloride, *Can. J. Chem. Eng.*, Vol. 45, pp. 241-249.
- Qi, Y., Klausner, J. F., 2004, Comparison of gas nucleation and pool boiling site densities, 2004 ASME International Mechanical Engineering Congress, Anaheim, CA, USA.
- Rammig, R., Weiss, R., 1991, Growth of vapour bubbles from artificial nucleation sites, *Cryogenics*, Vol. 31, pp. 64-69.
- Sadasivan, P., Unal, C., Nelson, R. A., 1995, Nonlinear aspects of high heat flux nucleate boiling heat transfer, *J. Heat Transfer*, vol. 117, pp. 981-989.
- Sernas, V., Hooper, F. C., 1969, The initial vapor bubble growth on a heated wall during nucleation boiling, *Int. J. Heat Mass Transfer*, vol. 12, pp. 1627-1639.
- Sgheiza, J. E., Myers, J. E., 1985, Behavior of nucleation sites in pool boiling, *A. I. Ch. E. J* 31, pp. 1605-1613.

- Shoji, M., Takagi, Y., 2001, Bubbling features from a single artificial cavity, *Int. J. Heat Mass Transfer*, Vol. 44, 2763-2776.
- Shoji, M., Zhang, L., 2003, Boiling features on artificial surfaces, 5th International Conference on Boiling Heat Transfer, Montego Bay, Jamaica, keynote lecture.
- Theofanous, T. G., Tu, J. P., Dinh, A. T., Dinh, T. N., 2002, The boiling crisis phenomenon Part I: nucleation and nucleate boiling heat transfer, *Experimental Thermal and Fluid Science*, 26, pp. 775-792.
- Thorncroft, G. E., Klausner, J. F., Mei, R., 1997, Suppression of flow boiling nucleation, *J. Heat Transfer*, vol. 119, pp. 517-524.
- Tong, W., Cohen, A. B., Simon, T. W., You, S. M., 1990, Contact angle effects on boiling incipience of highly-wetting liquids, *Int. J. Heat Mass Transfer*, vol. 33, No. 1, pp. 91-103.
- Tretheway, D. C., Meinhart, C. D., 2002, Apparent fluid slip at hydrophobic microchannel walls, *Physics of Fluids*, 14(3), pp. 9-12.
- Tretheway, D. C., Meinhart, C. D., 2004, A generating mechanism for apparent fluid slip in hydrophobic microchannels, *Physics of Fluids*, 16(5), pp. 1509-1515.
- Tyrell, J. W. G., Attard, P., 2001, Images of nanobubbles on hydrophobic surfaces and their interactions, *Phys. Rev. Lett.* 87, no.17, 176104.
- Walpole, R. E., 1978, *Probability and statistics for engineers and scientists*, New York, Macmillan Publishing Co., Inc, pp. 133-135.
- Wang, C. H., Dhir, V. K., 1993, On the gas entrapment and nucleation site density during pool boiling of saturated water, *J. Heat Transfer*, vol. 115, pp. 670-679.
- Wang, C. H., Dhir, V. K., 1993, Effect of surface wettability on active nucleation site density during pool boiling of saturated water, *J. Heat Transfer*, vol. 115, pp. 659-669.
- Wienecke, M., Yan, Y. Y., Kenning, D. B. R., 1999, Bubble nucleation and growth during saturated pool boiling on thin vertical plate, *Applied Optical Measurements*, Eds. M. Lehner, D. Mewes, U. Dinglreiter, R. Tauscher, Springer-Verlag, Berlin, pp. 107-120.
- Yang, S. R., Kim, R. H., 1988, A mathematical model of the pool boiling nucleation site density in terms of the surface characteristics, *Int. J. Heat Mass Transfer*, Volume 31, Issue 6, pp. 1127-1135.
- Yang, S. R., Xu, Z. M., Wang, J. W., Zhao, X. T., 2001, On the fractal description of active nucleation site density for pool boiling, *Int. J. Heat Mass Transfer*, Vol. 44, pp. 2783-2786.

- Zeng, L. Z., Klausner, J. F., 1993, Nucleation site density in forced convection boiling, *J. Heat Transfer*, vol. 115, pp. 215-221.
- Zeng, L. Z., Klausner, J. F., 1993, Heat transfer, incipience, and hysteresis in saturated flow boiling, *AICHE Symp. Series, Heat Transfer, Atlanta*, pp.480-485.
- Zhang, L., Shoji, M., 2003, Nucleation site interaction in pool boiling on the artificial surface, *Int. J. Heat Mass Transfer*, 46, pp. 513-522.

BIOGRAPHICAL SKETCH

Yusen Qi was born in Zhejiang, China, on December 3, 1973. After receiving his Bachelor of Science in mechanical engineering from Xian Jiaotong University in 1994 and Master of Science in engineering from the same university, Yusen worked for Gree Electrical Appliance Co., China, as an engineer. In pursuit of a Ph.D. degree in mechanical engineering, Yusen began his studies at the University of Florida in 2001.